ABSTRACT

Title of Document: OCEAN VARIABILITY IN CMIP5 (COUPLED MODEL INTERCOMPARISON PROJECT PHASE 5) HISTORICAL SIMULATIONS

Yanni Ding, Doctor of Philosophy, 2014

Directed By: Professor James A. Carton
Department of Atmospheric and Oceanic Science

The oceans play a key role in the global climate variability. This dissertation examines climate variability in historical simulations from fourteen CMIP5 (Coupled Model Intercomparison Project Phase 5) coupled models on different time scales. Responses of oceans to the external volcanic eruption, green house gas forcing, and internally generated variability are investigated with emphasis on higher latitudes.

Chapter 2 addresses the oceanic response to tropical volcanic eruptions. Previous modeling studies have provided conflicting high latitude climate responses to volcanic eruptions, including the ocean's role. This controversy happens mainly because the response varies widely from model to model, and even varies among ensemble members of a single model. The increase in Atlantic Meridional

Overturning Circulation (AMOC) after the volcanic eruption is closely linked with its internal variability.

Chapter 3 addresses the seasonal and centennial trends in the Arctic Ocean. The Arctic warming is apparent in all models, although there is considerable variability especially its seasonal cycle. Both the surface heat flux and the oceanic heat convergence contribute to the Arctic warming on centennial time scale. Meanwhile, the seasonal variation of oceanic warming is largely determined by the atmospheric heating. In models presenting a clear seasonal cycle of surface net flux increases, there is a notable retreat of sea ice extent in winter, which allows more heat loss from the ocean through turbulent fluxes.

Chapter 4 discusses the internally generated variability of high latitude water masses. Both the magnitude and the time scale of subarctic decadal variability are strikingly similar to observations. The analysis of the more realistic models provides constraints on relative roles of the oceanic heat transport and the atmospheric heat flux. One possible factor that could give rise to the different origins of ocean variability is the blocking of mid-latitude jet stream. The oceanic heat transport is more important to the decadal variability of the high latitude ocean in models where winter-time atmospheric blocking events over the Euro-Atlantic sector are more frequent.

OCEAN VARIABILITY IN CMIP5 (COUPLED MODEL INTERCOMPARISON PROJECT PHASE 5) HISTORICAL SIMULATIONS

By

Yanni Ding

Dissertation submitted to the Faculty of the Graduate School of the
University of Maryland, College Park, in partial fulfillment
of the requirements for the degree of
Doctor of Philosophy
2014

Advisory Committee:
Professor James Carton, Chair
Doctor Gennady Chepurin
Doctor Sirpa Häkkinen
Professor Sumant Nigam
Professor William Boicourt

Acknowledgements

First and foremost, I would like to thank my advisor, Professor James Carton, for offering me a great opportunity to study on lots of interesting topics. I am deeply thankful his guidance, patience, and support through my Ph.D. study. I also would like to thank the rest of my committee members: Doctor Gennady Chepurin, Doctor Sirpa Häkkinen, Professor Sumant Nigam and Professor William Boicourt. They have been very helpful and very supportive during my graduation process. My thank goes to Doctor Gennady Chepurin for his generous help from basic software usage to broad scientific advices. I also would like to thank Doctor Semyon Grodsky, Professors Sumant Nigam and Rachel Pinker for a lot of helpful advice and suggestions.

I would like to thank Professor Georgiy Stenchikov of KAUST, and Professor Alan Robock of Rutgers University for their help with my study of oceanic response to volcanic eruptions. I also would like to thank Doctor Sirpa Häkkinen of NASA/GSFC for her kindly help towards my understanding of the atmospheric blocking, and Professor Michael Steele of University of Washington for sharing his knowledge in the Arctic. I would like to thank Lori Sentman and John Krasting of NOAA/GFDL for their help with providing huge amount of model outputs for two GFDL-ESM models.

My thanks also go to all the faculty and staff of AOSC for their help. I enjoyed the delightful five years with my fellow students and friends. Last but not least, I would like to give my deepest thanks to my husband, Yi Wang, and my parents, Limei An and Rixian Ding, for their endless love and support during my Ph.D. study.

Table of Contents

Acknowledgements ii
Table of Contents iii
List of Tables v
List of Figures vi
Chapter 1: Introduction 1
1.1 Background 1
1.2 External forcing on the North Atlantic and the Arctic 5
1.2.1 Impacts of volcanic eruptions on the North Atlantic and the Arctic 5
1.2.2 Response of the North Atlantic and the Arctic to the green house gas forcing 7
1.3 Climate variability on inter-annual to decadal time scale in the sub-Arctic seas 7
1.3.1 Atmospheric blockings and Atlantic storm tracks 7
1.3. 2 Atlantic Meridional Overturning Circulation 9
1.4 Thesis organization 10
Chapter 2: Ocean response to volcanic eruptions in CMIP5 simulations 11
2.1 Introduction 11
2.2 Data and methods 15
2.2.1 CMIP5 model description 15
2.2.2 Methods and observational data 18
2.2.3 REEOF analysis 19
2.3 Global response to volcanic eruptions 20
2.3.1 Atmospheric response to volcanic eruptions 20
2.3.2 Oceanic response to volcanic eruptions 25
2.4 Impact of volcanic eruptions on the Atlantic and tge Arctic 33
2.4.1 Impacts of volcanic eruptions on the Arctic sea ice 33
2.4.2 Impacts of volcanic eruptions on AMOC 34
2.5 Summary 39
Chapter 3: Seasonal and centennial trends in Arctic climate: information from CMIP5 simulations 42
3.1 Introduction 42
3.2 Data and methods 47
3.2.1 CMIP5 model description 47
3.2.2 Methods 47
3.2.3 Observational data decription 50
3.3 Mean state and seasonal cycle of the Arctic 51
3.3.1 Basic character of the atmosphere 51
3.3.2 Sea ice property and its impact on the albedo 53
3.3.3 Mean state of the Arctic Ocean 55
3.4 Centennial trend of the Arctic Ocean 65
3.4.1 Seasonal variations of atmospheric flux trend 65
3.4.2 Warming of the Arctic Ocean 67
3.4.3 Salinity changes in the Arctic Ocean 71
3.5 Summary 73

Chapter 4: Subarctic/Arctic decadal climate: insights from CMIP5 75
4.1 Introduction 75
4.2 Data and methods 81
4.2.1 Data description 81
4.2.2 Definition of blocking events 82
4.2.3 Definition of Atlantic water 83
4.3 Atmospheric blocking in CMIP5 historical simulations 84
4.3.1 Decadal variabilities of Atlantic water 84
4.3.2 Origins of the decadal variability of Atlantic water 87
4.3.3 Impacts of blocking events on the decadal variability 88
4.4 Decadal variability of Atlantic water in the sub-Arctic seas 89
4.4.1 Decadal variabilities of Atlantic water 89
4.4.2 Origins of the decadal variability of Atlantic water 92
4.4.3 Impacts of blocking events on the decadal variability 94
4.5 Decadal variability of the Arctic sea ice Summary 97
4.6 Conclusion and discussion 99
Chapter 5: Conclusions 102
5.1 Summary of results 102
5.2 Implications and future plans 107
Bibliography 109

List of Tables

Table 2.1. The name, eruption date, location and the Ice-core Volcanic Index 2 (IVI2) stratospheric sulfate injections [*Gao et al.* 2008] of volcanoes considered in this study. ……..... 13
Table 2.2. Some basic information about historical simulations examined in this study: name, source of aerosol loading, ocean model resolution(longitude × latitude × vertical), and the number of ensemble members using all forcing, and the number that do not include volcanic aerosols. ……..... 15

Table 3.1: Some basic information about historical simulations examined in this study: name, institution, ocean model resolution (longitude × latitude × vertical), and the number of all ensemble members and those with available daily geopotential height data ……..... 48
Table 3.2: Volume transport through the Bering Strait, the Davis Strait, the Fram Strait and the Barents Sea Opening. Units are Sv ……..... 62
Table 3.3: Heat transport through the Bering Strait, the Davis Strait, the Fram Strait and the Barents Sea Opening. Units are TW (10^{12} W) . ……..... 63
Table 3.4: Salt transport through the Bering Strait, the Davis Strait, the Fram Strait and the Barents Sea Opening. Units are 10^{6} Kg s^{-1} ……..... 64
Table 3.5: Correlation between changing rate of heat anomalies ($\partial HC/\partial t$) and surface net flux, and correlation between heat transports respectively for 14 CMIP5 models with seasonal cycle removed (from 1861 to 2005). ……... 71

Table 4.1: The minimum salinity of defined Atlantic water in different models …..84

List of Figures

Figure 1.1. Arctic Ocean currents and sea ice extent (source: [*Map Courtesy of Philippe Rekacewicz, UNEP/GRID-Arendal*]). Red and blue arrows show warm currents from Atlantic and Pacific and cold currents respectively. Dark and light blue shadings show the minimum and minimum sea ice extent …… 4
Figure 1.2. Summary of impacts of tropical volcanic eruptions on North Atlantic and Arctic Ocean…… 6

Figure 2.1. Global average all-sky and clear-sky downwelling surface shortwave flux anomalies (red and green) from the ensemble means of each of the eight models (Units: W m^{-2}). Black curves show aerosol optical depth of *Ammann et al.* [2003] (top panel, scale on right) and *Sato et al.* [1993] (second panel, scale on right). Dashed lines show the starting time of the five eruptions (in chronological order: Krakatau, St. Maria, Agung, El Chichón, and Pinatubo)…… 21
Figure 2.2. Ensemble means of the REEOF first (red, decay ENSO phase) and second (green, buildup ENSO phase) principle components after removal of the climatological seasonal cycle. Dashed lines show the starting time of the five eruptions (in chronological order: Krakatau, St. Maria, Agung, El Chichón, and Pinatubo). Lowest panel shows the average of the time series for all the model ensembles. No trend has been removed. ……23
Figure 2.3. Ensemble mean global net surface heat flux anomalies from the six-year average prior to each eruption. The seasonal cycle and the ENSO signal have been removed separately from each, and the time series are then smoothed with a running four-season average. Bars show the stand error from the ensemble mean. Lower right-hand panel shows the average of all the ensembles for each eruption. ……. 24
Figure 2.4. Ensemble mean global average SST anomaly from the six-year average prior to each eruption (similar to **Figure 2.3**). The seasonal cycle and the ENSO signal have been removed separately from each, and the time series have then been smoothed with a running four-season average. Lower right-hand panel shows observed SST processed in the same way (y-axis same as other panels) and the average SST of all ensembles with y-axis on the right. Bars show the stand error from the ensemble mean. ……... 26
Figure 2.5: Similar to **Figure 2.4** except that the ENSO signals are not filtered out ……. 27
Figure 2.6. Ensemble mean net surface heat flux difference between Northern and Southern Hemispheres (Northern minus Southern Hemisphere) from the six-year average difference prior to each eruption (similar to **Figure 2.3**). Units are W m^{-2}. The seasonal cycle and the ENSO signal have been removed separately from each, and the time series have then been smoothed with a running four-season average. Lower right-hand panel shows the average of all model ensembles for each eruption. Bars show the stand error from the ensemble mean. …….. 28
Figure 2.7. Ensemble mean sea surface salinity (units: psu) in the northern Atlantic sector for the two years following the Krakatau eruption minus the six year

average prior to eruption. Two models are shown: CCSM4 (left panel) which has a weak AMOC response to volcanic eruptions, and GFDL-CM3 (right panel) which has a strong AMOC response to volcanic eruptions……. 29
Figure 2.8. Ensemble mean two-year running averaged global ocean heat content anomalies (0/1000m) from both models and SODA (Simple Ocean Data Assimilation) data (units: K). The seasonal cycle of SODA data from 1970 to 2005 is removed from all model outputs and the average of 1970 are subtracted from all data. No linear trend has been removed. Vertical dashed lines indicate the starting time of the five eruptions…….. 30
Figure 2.9: Time series of sea surface temperature from CCSM4 and GFDL-CM3 historical runs with and without volcanic forcing……31
Figure 2.10. Global mean temperature anomaly scaled by the RMS annual temperature variability at each level. A quadratic trend computed separately for each model, at each level, is removed prior to computing anomalies in order to highlight the response to volcanic eruptions. Vertical axis is depth, (units: m). 32
Figure 2.11. Ensemble mean Northern Hemisphere sea ice mass anomaly (0-90ºN) from the six-year average prior to the eruption (similar to **Figure 2.3**) (units: $1x10^{15}$ kg). The seasonal cycle and the ENSO signal have been removed separately from each, and the time series have then been smoothed with a running four-season average. Lower right-hand panel shows the average of all model ensembles for each eruption. Bars show the stand error from the ensemble mean……..34
Figure 2.12. Ensemble mean Atlantic meridional overturning streamfunction anomaly from the six-year average prior to each eruption (units: Sv). The time series have been smoothed with a running eight-season average after removal of the climatological seasonal cycle. Lower right-hand panel shows the average of all the ensembles for each eruption. The El Chichón time series are truncated so they do not continue past the 1991 Pinatubo eruption. Bars show the stand error from the ensemble mean…….. 35
Figure 2.13. AMOC volume transport response to eruptions versus intrinsic AMOC variability. AMOC transport response is the increase during years 7-8 following eruptions versus the natural AMOC RMS annually averaged variability computed during the 41-year gap in huge tropical eruptions 1920 through 1960. Comparisons are shown for the strong Krakatau eruptions, the weak El Chichón eruption, and the average response to the five eruptions…… 36
Figure 2.14: Similar to **Figure 2.9** but for AMOC ……37
Figure 2.15. Ensemble mean zonal integrated Atlantic meridional overturning transport streamfunction (color, units: Sv) and zonal mean density (contours, CI: 25 g m^{-3}) response to the Krakatau eruption estimated from the difference between the two year average (years 7-8) following the eruption minus the average during the prior six years……38
Figure 2.16. Same as **Figure 2.15** except showing anomalous temperature (colors, units: K) and salinity (contour, CI: 0.05 psu)…….. 39

Figure 3.1: Time mean of ensemble mean of winter-time (DJFM) sea level pressure from 1861 to 2004 at high latitudes for 14 CMIP5 models and HadSLP2 observational data. Units are mb……..52
Figure 3.2: Seasonal cycle of ensemble mean surface downward net flux (black), net shortwave flux (red), net longwave flux (green), latent heat flux (blue) and sensible heat flux (yellow) from 1957 to 2002 over the high latitude ocean (north to 65°N) for 14 CMIP5 models and ERA-40 reanalysis data……..53
Figure 3.3: Time mean sea ice concentration (%) (color shading), winter-time (DJFM) sea ice extent (black contour), and summer-time (JJAS) sea ice extent (red contour) from 1861 to 2005 for 14 CMIP5 models……..54
Figure 3.4: Seasonal cycle of ensemble mean surface net flux, cloud fraction, and sea ice extent at the high latitude ocean (north to 65°N) for GFDL-ESM2G, GISS-E2-R and NSIDC observational data……55
Figure 3.5: Time mean of ensemble mean upper ocean temperature (0-100m) from 1900 to 1994 for 14 CMIP5 models and PHC3.0 observational data. Units are °C. 56
Figure 3.6: Time mean of ensemble mean upper ocean salinity (0-100m average) for 14 CMIP5 models and SODA reanalysis data. Time mean is calculated from 1861 to 2005 for models and from 1871 to 2005 for SODA. Units are psu…...57
Figure 3.7: Ensemble mean temperature and salinity profiles for one across-Arctic sector (30E and 150W) for CCSM4, HadCM3 and PHC3.0 from 1900 to 1994. Units for temperature are °C, and units for salinity are psu. ……..… 58
Figure 3.8: Ensemble mean temperature and salinity profiles in the defined four regions for CCSM4 (open circle), HadCM3 (triangle) and PHC3.0 (closed square) for time period 1900-1994. Locations of selected regions are marked in the two spatial maps on the left panel. AWZ means the Atlantic water zone in the Nordic Seas, and BaS stands for the Barents Sea. LS is short for the Laptev Sea, and BeS is for the Beaufort Sea. Units for temperature are °C, and units for salinity are psu……59
Figure 3.9: Time mean of ensemble mean surface velocity from 1861 to 2005 at Arctic Basin in CCSM4 and HadCM3…….61
Figure 3.10: Correlation between the ensemble mean sea level pressure and upper ocean salinity (0-100m) at Beaufort Gyre (75-80°N, 150-180°W) from 1861 to 2005…… 61
Figure 3.11: The long-term trend of ensemble mean surface downward net flux (black), net shortwave flux (red), net longwave flux (green), latent heat flux (blue) and sensible heat flux (yellow) at high latitudes for 14 CMIP5 models. The long-term trend here is defined as the difference between the mean value from 1861 to 1880 minus the mean from 1986 to 2005…… 66
Figure 3.12: Seasonal feedbacks: rate of change of heat flux versus rate of change of sea ice extent for various flux components. Open marks are calculated from 1861 to 2005; closed marks are calculated from 1950 to 2005……67
Figure 3.13: Temperature and salinity profile changes in recent 145 years in the defined four regions for CCSM4 and HadCM3. Open circles and squares show the average temperature and salinity from 1861 to 1880, and closed circles and squares show the average temperature and salinity from 1986 to 2005…….. 68

Figure 3.14: Seasonal cycle of ensemble mean mix-layer heat content increase (0-70m, light grey) and heat content increase due to sea ice melting (dark grey) in the Arctic Ocean. Increase of heat content is calculated as the 1986-2005 mean minus 1861-1880 mean……69
Figure 3.15: Seasonal cycle of heat flux changes through the Denmark Strait (red line, left Y axis), the Iceland-Norway Strait (green line, right Y axis) and total heat flux through these two straits (black line, left Y axis) for 1861-1880 (solid line) and 1986-2005 (dash line). Heat flux is calculated relative to 0°C…….70
Figure 3.16: Upper ocean salinity (0-100m average) difference over high latitude ocean for 14 CMIP5 models and SODA reanalysis data. Difference is defined as the 1986-2005 mean minus 1861-1880 mean for models, and 1986-2005 mean minus 1871-1880 mean for SODA…….. 72

Figure 4.1: Example of geopotential height (contours, units: mb), surface ocean velocity (arrows, units: m/s), and SST (°C) from GFDL-CM3 for a month with persistent Greenland atmospheric blocking (>19 days). …….76
Figure 4.2: Mean winter-time (DJFM) blocking days in North Hemisphere for CCSM4, GFDL-CM3 and HadCM3, which present three types of blocking distributions over Greenland and western Europe seen among the CMIP5 models considered here. CCSM4 have only one ensemble with daily blocking data, while GFDL-CM3 and HadCM3 have five and 10 ensembles separately…… 85
Figure 4.3: The first EOF pattern of winter-time (DJFM, 1861-2004) sea level pressure for the North Atlantic sector as represented in CCSM4, GFDL-CM3, HadCM3 and observations (units: mb). ……..86
Figure 4.4: (a) Time series of the frequency of winter-time (DJFM) blocking days plotted against the NAO index for GFDL-CM3 ensemble member #5. (b) Relationship between mean blocking days and the latitude of the low-pressure center of the NAO (see **Figure 4.3**). (c) Similar to (b) except for longitude….. 88
Figure 4.5: Correlation between surface net flux and the NAO index for models with frequent (contours, left panel) and infrequent (contours, right panel) Greenland blocking events. Color shows the time-mean winter-time (DJFM) surface net flux from 1861 to 2005……89
Figure 4.6: Root mean square heat content from observations (upper left), ensemble mean of all 14 models (upper right), and CCSM4 and GFDL-CM3 (lower panels). Heat content is calculated from surface to bottom. Both seasonal cycle and the long-term trend have been removed. Data are running two-year average……..90
Figure 4.7: a) Temperature profiles and (b) salinity profiles of the Nordic Seas Atlantic Water region for CCSM4, GFDL-CM3 and HadCM3. The seasonal cycle and linear trend have been removed and data have been low-pass filtered with a running two-year average……..91
Figure 4.8: Lead/lag correlation between the North Hemisphere SST and the SST in the Nordic Seas for HadCM3. The apparent northward progression of the correlation suggests the importance of heat advection in this model…….. 93
Figure 4.9: Time series of downward net surface flux and anomalous heat content tendency ($\partial HC/\partial t$) in the Nordic Seas Atlantic water region as it appears in

CCSM4, GFDL-CM3 and HadCM3. Heat content is calculated from surface to 600m deep……94
Figure 4.10: Relationship between mean winter-time (DJFM) blocking days over Greenland and the correlation coefficient between the heat storage changing rate ($\partial HC/\partial t$) and surface net flux of Atlantic water…… 95
Figure 4.11: Mean state of winter-time ocean surface currents (arrows) and sea level pressure (color) for models with frequent (left panel) and infrequent (right panel) Greenland blocking events……...96
Figure 4.12: Difference of ocean currents (arrows) and sea level pressure (color) between years with more blocking days (larger than the mean value) and years with fewer blocking days. Models with frequent (left panel) and infrequent (right panel) Greenland blocking events are considered respectively here..…..... 97
Figure 4.13: Area mean sea ice concentration over Barents Sea (red) and volume transport through Barents Sea Opening (black) for CCSM4, MPI-ESM-LR, and MRI-CGCM3……...98

Chapter 1: Introduction

Interactions between atmosphere and ocean play an important role in the global climate on seasonal and longer time scales. Interactions at high latitude are particularly intense because of feedback processes unique to the cold and dry conditions found there. In some cases these interactions are driven by externally controlled fluctuations in the net downwelling radiation. The seasonal cycle is an example of this. In others the interactions seem to be the result of internal variability. In this study I examine interactions between atmosphere and ocean on several timescales from seasonal to centennial. I begin by examining the global oceanic response to volcanic eruptions (Chapter 2). In Chapters 3 and 4 I shift attention a bit and examine the forced and internal variability of high Northern Hemisphere climate. The two most prominent external forcings are the reduction due to volcanic eruptions and the enhancement of net longwave radiation due to the increase in greenhouse gas. A common theme is that in each case I use results from the wonderful suite of historical coupled model simulations produced as part of the latest release of the Coupled Model Intercomparison Project (CMIP5).

1.1 Background

The Arctic Ocean connects with Pacific Ocean through the Bering Strait, and with the Atlantic Ocean through the Nordic Seas region, which is the region north of the Greenland-Scotland Ridge and south of the Arctic Ocean, including the Greenland Sea, the Iceland Sea, the Norwegian Sea and the Barents Sea (**Figure 1.1**). The Bering Strait flow brings ~1 Sv of cold and fresh Pacific water into the Arctic Ocean.

The fresh water goes across the Arctic Basin and exports to the North Atlantic Ocean mainly through the Davis Strait and the Fram Strait. Approximate 8 Sv of warm and salty Atlantic water reaches the Nordic Seas, where most of the heat and mass exchanges happen. The Nordic Seas together with the Labrador Sea are two locations where deep water formation takes place, which is an important part of the Atlantic Meridional Overturning Circulation (AMOC).

The major circulation patterns in the Arctic Basin are the Beaufort Gyre and the transpolar drift. The surface anti-cyclonic wind pattern corresponding to the Polar high pressure system drives sea water anti-cyclonically and forms the Beaufort Gyre, which is most prominent in winter. In addition to the Polar high, another important winter-time atmospheric pattern over the high latitude ocean is in the blocking of the mid-latitude jet stream over the North Atlantic, which is closely linked with the Atlantic storm tracks and the North Atlantic Oscillation (NAO). The interannual variability of blocking frequency over the North Atlantic is able to influence the subpolar ocean and the Nordic Seas through regulating the wind pattern.

There are three different atmosphric forcings considered in this dissertation: 1) volcanic aerosols and their impact on solar radiation, 2) the seasonal cycle of sunlight at high latitudes and its impact on solar radiation, and 3) greenhouse forcing and its impact on net infrared radiation. Some huge tropical eruptions, like the Pinatubo, reduce the solar flux by about -5 W m^{-2}. Seasonal differences of the surface flux at the Arctic Ocean are as large as several hundred W m^{-2}, for which both the cloud and sea ice extent are important because of their regulation of surface reflectivity. The radiative forcing because of carbon dioxide, on of the most important green house

gases, is ~3.7 W m^{-2} on global scale. The green house gas forcing is most remarkable in the Arctic Ocean partly due to its positive feedback with the sea ice.

Recent observational studies have shown surprising variability in the properties of the Atlantic Water in the Nordic Seas. Because of limitations of the historical records, I turn to analysis of coupled climate models to understand the complex interactions in the entire climate system. Historical simulations of 14 Coupled Model Intercomparison Project (CMIP5) coupled climate models are analyzed in this study together with other observational data sets. The CMIP5 provides multi-model and multi-ensemble context for studying the mechanism responsible for atmosphere-ocean-sea ice feedback process and the climate variability at multiple time scales. Previous studies suggest that there is a big improvement in simulating column-integrated cloud amount and the seasonal cycle of sea ice extent in the CMIP5 compared to the CMIP3 [*Jiang et al*., 2012; *Stroeve et al.,* 2012]. The equilibrium climate sensitivity of CMIP5 coupled climate models ranges 2.1 to 4.7 °C, which is largely due to the differences in cloud feedbacks [*Andrews et al*., 2012].

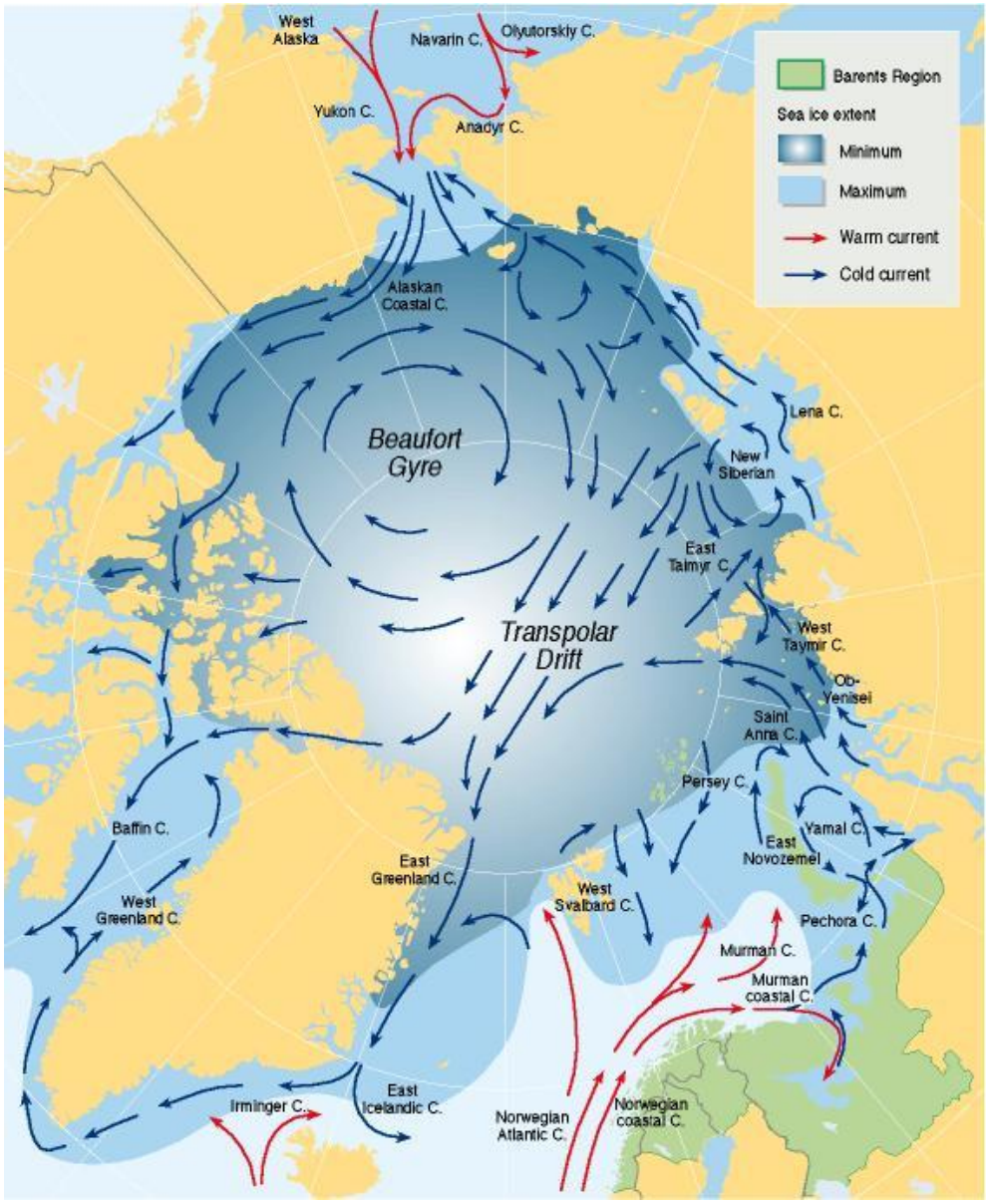

Figure 1.1. Arctic Ocean currents and sea ice extent (source: [*Map Courtesy of Philippe Rekacewicz, UNEP/GRID-Arendal*]). Red and blue arrows show warm currents from Atlantic and Pacific and cold currents respectively. Dark and light blue shadings show the minimum and minimum sea ice extent.

1.2 External forcing on the North Atlantic and the Arctic

1.2.1 Impacts of volcanic eruptions on the North Atlantic and the Arctic

Volcanic eruptions are one of the most important natural causes of climate change. Volcanoes eject sulfuric gases into the lower stratosphere where they oxidize to form sulfate aerosols, which spread globally over the course of weeks. The lifetime of stratospheric sulfate aerosols is about 1 year, but the brought impacts can be found on many time scales, from annual to decadal. The mechanisms that tropical volcanic eruptions affect the North Atlantic and Arctic Ocean through the stratospheric sulfate aerosols are summarized in **Figure 1.2**. On one hand, stratospheric sulfate aerosols cool the surface by reflecting the solar radiation back to the space. Due to this cooling effect, earth surface temperature decreases and the sea ice coverage extends. The cooling effect can also reduce the precipitation, and increase the salinity at Nordic Seas, which would make the surface water denser, accelerate the deep water formation and enhance the Atlantic overturning circulation [*Stenchikov et al*., 2009; *Iwi et al*., 2012; *Ding et al*., accepted by JGR.].

On the other hand, the volcanic eruption can heat the lower stratosphere by absorbing both solar and terrestrial radiation. For tropical eruptions, the tropical stratosphere would be warmer in Northern Hemisphere winter, which enhance the pole-to-equator temperature gradient. This larger temperature gradient produces a stronger polar vortex, pushing the system into a positive NAO phase [*Robock et al*., 2000; *Stenchikov et al*., 2002; *Stenchikov et al*., 2006]. According to some studies, the NAO phase may also be correlated with AMOC by affecting the heat flux over

Labrador seas [*Stenchikov et al*., 2009; *Ottera et al., 2010*]. In this study, we will mainly discuss the cooling effect.

Some recent studies suggest that eruptions can increase the likelihood of El Niño, while other studies conclude there is no causative link between these two [*Adams et al.,* 2003; *Mann et al.,* 2005; *Emile-Geay et al.,* 2008; *McGregor et al.,* 2010; *Christiansen,* 2008; *McGregor & Timmermann*, 2011]. To make volcanic signal clear, we removed the ENSO signal from all the surface variables.

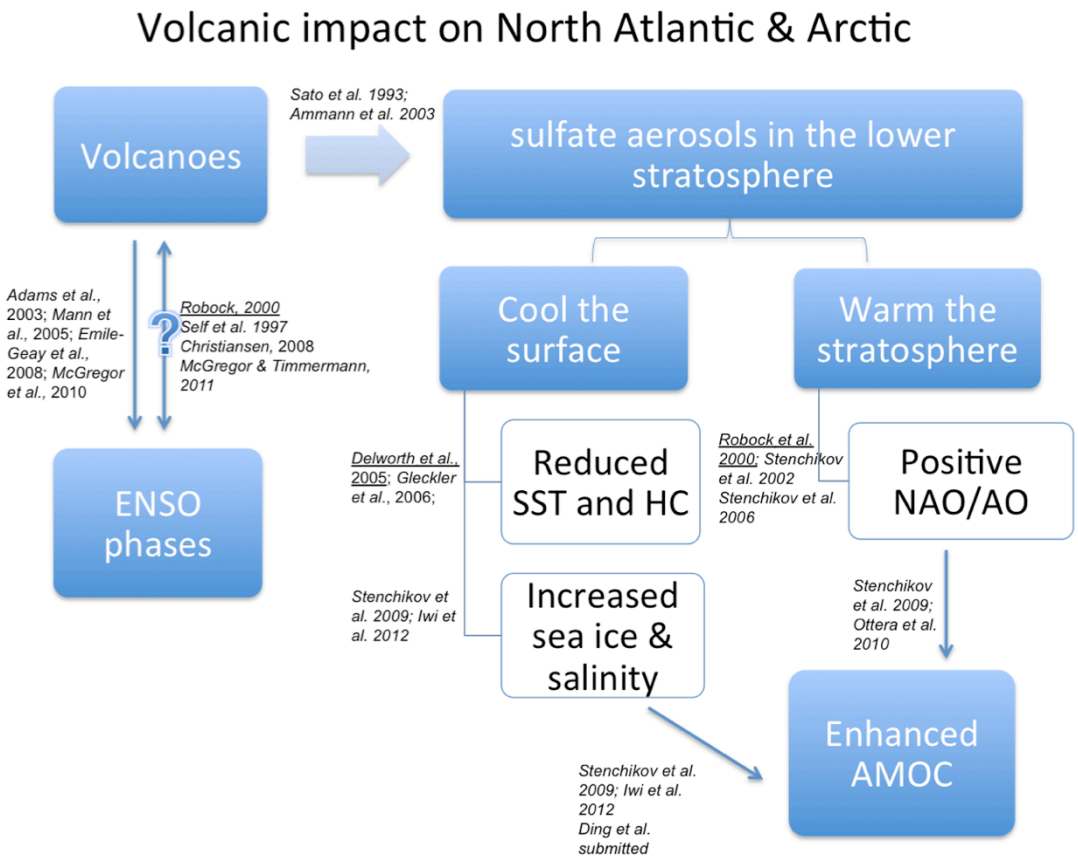

Figure 1.2. Summary of impacts of tropical volcanic eruptions on North Atlantic and Arctic Ocean.

1.2.2 Response of the North Atlantic and the Arctic to the green house gas forcing

Over the whole globe, the Arctic is the most sensitive region to the green house gases forcing with remarkable changes in atmosphere, ocean and sea ice during the last decades. There are mainly two reasons for the high sensitivity of the Arctic to global warming: one is the "ice-albedo" feedback, and another is the ocean heat convergence into the Arctic. Increasing net downward heat flux increases the surface temperature and melts the sea ice, which decreases the area of sea ice with high reflectivity and reduces the surface albedo. Smaller surface albedo increases the surface net flux and further enhances the warming process. This positive feedback loop is referred as "ice-albedo" feedback [*Graversen and Wang*, 2009; *Steele et al.*, 2010].

In general, the Arctic Ocean loses heat through surface radiative process and gains heat mainly from the warm and salty Atlantic water inflow through the Nordic Seas. During the past decades, the deep water of the Nordic Seas underwent warming by about 0.01°C yr^{-1}, and sea ice extent in this region also decreases by ~33% **[***Østerhus and Gammelsrød*, 1999*Vinje*, 2001]. Heat gained at the Nordic Seas would warm the Arctic Basin further through the advective heat flux.

1.3 Internal variability on inter-annual to decadal time scale over Nordic Seas and Arctic

1.3.1 Atmospheric blockings and Atlantic storm tracks

Tropospheric blocking happens when there is a large region of air isolated from the eastward jet stream, which usually lasts for more than 5 days, and modifies the movement of Atlantic storm tracks [*Rex*, 1950a, b]. The blocking event could be

found through the year at mid-latitude regions, but it is more frequent in winter.

Blocking events over North Atlantic are able to influence the underlying meteorology on synoptic time scale. The breaking of jet stream due to the blocking event develops an anti-cyclonic high-pressure center, and the subsidence air makes the underlying region drier and less cloudy, which will allow more upward longwave flux heat loss and causes a colder winter [*Green*, 1977; *Buehler et al*., 2011; *Trigo et al*., 2004; *Sillmann et al*., 2011].

The frequency of winter-time blocking events over the North Atlantic could also explain some low-frequency climate variabilities. *Häkkinen et al.* [2011] pointed out that the anticyclone caused by blocking changes the wind pattern and surface wind curl, which alters the ocean circulation and changes the upper ocean properties in the North Atlantic Ocean.

In winters with frequent blocking events, the Atlantic storms become weaker and move southward, which leads to less heat transport from the northwestern North Atlantic Ocean to Europe continent. Recent studies showed that low-frequency of the North Atlantic Oscillation (NAO) is strongly linked with the presence /absence of Greenland blocking events [*Croci-Maspoli et al*., 2007a; *Woollings et al.*, 2008]. *Woollings et al.* [2008] found a correlation between the Greenland Blocking and NAO of -0.47.

Causative link between blocking events and NAO on synoptic time scale have been studied, and several mechanisms have been proposed. One suggests that the breaking of jet stream develops an anti-cyclonic circulation pattern, which leads to the negative phase of the NAO. Other studies argued that high pressure at the

subpolar ocean when NAO phase is negative is preferable for occurrence of blocking events because of the modification of planetary waves. In addition, it's also been suggested that NAO and the blocking over the North Atlantic are two different descriptions of one phenomenon. The low frequency of winter-time blocking events and the positive phase of NAO are both characterized by an intensified and southward shifted Atlantic storm tracks [*Luo* 2005; *Huang et al.*, 2006; *Luo et al.*, 2007; *Wollings et al.*, 2008; *Woollings et al.*, 2010; *Häkkinen et al.*, 2011].

1.3.2 Atlantic Meridional Overturning Circulation

AMOC is a large-scale thermohaline circulation in the Atlantic Ocean, which carries upper-layer warm and salty water from south to north, and brings cold deep water from north to south. There are mainly two physical mechanisms to explain AMOC: one is the vertical mixing process which forms the Atlantic deep water, and another is the wind-driven Ekman upwelling process at the Southern Ocean. The deep water formation process mainly happens at the Labrador Sea and the Greenland Sea, and this process is more frequent in the Labrador Sea [*Kuhlbrodt et al*., 2007].

AMOC variability is considered as an internal variability, which is also influenced by external forcing such as volcanic eruptions and green-house-gas forcing. Salt rejection during sea ice growth and decreased ocean upper-layer temperature are both responsible for the denser surface salinity and an enhanced AMOC after volcanic eruptions [*Stenchikov et al*., 2009; *Iwi et al*., 2012; *Ding et al.,* accepted by JGR]. It has been observed that AMOC has slowed down in rent decades. Some studies argue that this might be driven by variations of the NAO through changing the heat flux and

convection process in the Labrador Sea [*Bryden et al*., 2005; *Dickson et al*., 1996; *Latif et al*., 2006].

1.4 Thesis organization

I started with analyzing the oceanic response to tropical volcanic eruptions, presented in Chapter 2. I evaluated impacts of volcanic eruptions on the global oceans and on the North Atlantic and the Arctic in different models. Discrepancies in oceanic response among models are also discussed in this section.

Chapter 3 shows the mean state and seasonal cycle of the high latitude region in the CMIP5 models. After that, the centennial trend of the atmosphere, ocean and sea ice in the Arctic Ocean as well as the interactions within the entire climate system is studied.

In chapter 4, I first compared the simulated low-frequency atmospheric variability, i.e. the atmospheric blocking events over the North Atlantic and NAO, to the observations. Then I analyzed the climate variability of the Nordic Seas on interannual to decadal time scale in CMIP5 models. After that, how the blocking events influence the decadal variability of the Nordic Seas and the Arctic is presented.

Finally, conclusions along with discussion on further work are offered in Chapter 5.

Chapter 2: Ocean response to volcanic eruptions in CMIP5 Simulations

2.1 Introduction

This study examines the impact of volcanic eruptions on the ocean using recent coupled model simulations from the Coupled Model Intercomparison Project Phase 5 (CMIP5). The past decade has seen considerable progress in understanding the ocean response to volcanic aerosols in coupled models. For major volcanic eruptions, reductions in net short wave heating lead to a drop in global annual sea surface temperature (SST) by a few tenths of a degree K for a few years and a decrease in the temperature of the upper 3000 m by -0.01 to -0.02 K spanning decades, although the experiment design might change this number [*Robock and Mao*, 1992; *Delworth et al*., 2005; *Stenchikov et al*., 2009; *Gergory,* 2010; *Booth et al*., 2012; *Driscoll et al*., 2012; *Iwi et al.,* 2012].

In one key example of the potential impact of eruptions on the background state *Stenchikov et al.* [2009] and *Otterå et al.* [2010] present model results showing major eruptions strengthening the North Atlantic Ocean meridional overturning circulation (AMOC) by a Sverdrup (10^6 m^3 s^{-1}) or more on 5-15 year time scales. These studies suggest two mechanisms for the increase: 1) changes in wintertime surface wind stress, and/or 2) increasing the density of polar surface water and thus its ability to convect. Such changes correspond to a significant 5% increase in the Atlantic's contribution to the Earth's meridional heat transport. In contrast, *Mignot et al.* [2011], and *Iwi et al.* [2012] find an increase for some eruptions but not for others, while *Zhong et al.* [2011] find a decrease in AMOC due to the stabilizing impact on surface

salinity of increases in sea ice export into the North Atlantic Ocean. *Zanchettin et al.* [2013] conduct a series of experiments with a single model examining the climate response to the combined Tambora and Cosiguina eruptions and suggest that some of the differences in the AMOC and gyre circulation responses to eruptions is due to the differing background states of the model climates when the eruptions occurred. One alternative explanation is that the differences are due to differences in the models themselves. To explore this model dependence we present a composite examination of the impact of volcanic aerosols on the ocean based on analysis of five major tropical volcanoes represented in 36 historical simulations using eight recent climate models.

Tropical volcanic eruptions inject sulfuric gases into the lower stratosphere where they oxidize to form sulfate aerosols. The two largest of these during our 136 year period of interest are the 1883 eruption of Krakatau and the 1991 eruption of Pinatubo (**Table 2.1**), both of which resulted in an increase of aerosol optical depth (AOD) at 0.55 μm of ~0.15 (~20 Tg SO_2 injection) [*Gao et al.,* 2008; *Schmidt et al.,* 2011; *Crowley and Unterman,* 2012]. The 1902 eruption of Santa Maria, the 1963 eruption of Agung, and the 1982 eruption of El Chichón are of the similar size according to *Sato et al.* [1993] with El Chichón slightly larger. But *Ammann et al*. [2003] ranks Santa Maria the strongest of the three. These stratospheric sulfate aerosols spread globally over the course of months increasing planetary albedo and reducing downwelling shortwave radiation.

Table 2.1. The name, eruption date, location and the Ice-core Volcanic Index 2 (IVI2) stratospheric sulfate injections [*Gao et al.* 2008] of volcanoes considered in this study.

Name	Date	Latitude	Longitude	IVI2 (Tg)
Krakatau	26-27 August 1883	6.1°S	105.4°E	22
Santa María	24-25 October 1902	14.8°N	91.6°W	4
Agung	17 March, 16 May 1963	8.3°S	115.5°E	17
El Chichón	3-4 April 1982	17.4°N	93.2°W	14
Pinatubo	15 June 1991	15.1°N	120.4°E	30

The characteristic lifetime of stratospheric aerosols is on the order of a year or two. But the climate response to volcanic eruptions persists far longer due to their impact on the more slowly evolving components of the Earth system, notably the ocean. Historical observations confirm model results suggesting that large eruptions can reduce global mean SST by -0.3 to -0.5 K for several years relative to the centennial temperature trend [*Rampino and Self,* 1982; *Mass and Portman*, 1989; *Angell and Korshover*, 1985; *Angell,* 1988; *Minnis et al*., 1993]. Models have shown this anomalously cool water is subducted primarily into the upper 1000 m where it persists for many decades [*Delworth et al.,* 2005; *Gleckler et al*., 2006; *Stenchikov et al*., 2009; *Driscoll et al.,* 2012; *Iwi et al*., 2012]. Water found at this depth has various surface source regions: the Southern Ocean, marginal seas such as the Mediterranean, and subtropical and subpolar frontal regions [*Schmitz,* 1995]. The rates of formation vary from year to year in each location and are modulated by surface climate. At higher latitudes temperature anomalies increasingly act like passive tracers for a circulation driven by haline processes and are thus strongly linked to the atmospheric hydrologic cycle [*Talley et al.,* 2011].

Other impacts of volcanic aerosols on natural interannual to decadal climate variability (e.g., El Niño/Southern Oscillation, ENSO) have been discussed before [*Robock and Mao*, 1995; *Stenchikov et al*., 2006; *Evan et al*., 2009; *Otterå et al*., 2010; *Zanchettin et al.* 2012; *Booth et al*., 2012; *Zanchettin et al.* 2013; *Haywood et al.* 2013]. Some recent studies of proxy data and model simulations suggest that eruptions increase the likelihood of El Niño because reduced surface radiation reduces the zonal SST gradient along the equatorial Pacific [*Adams et al.,* 2003; *Mann et al.,* 2005; *Emile-Geay et al.,* 2008; *McGregor et al.,* 2010]. In contrast, *McGregor and Timmermann* [2011] find an initially La Niña–like response. Still other studies conclude there is no causative link between volcanic eruptions and ENSO [*Self et al.,* 1997; *Robock,* 2000; *Christiansen,* 2008]. Among the five volcanic eruptions we examine in this study, four are known to have occurred with concurrent strong El Niño events: Krakatau (1883), Agung (1963~1964), El Chichón (1982), and Pinatubo (1991), while Santa Maria is somewhat uncertain (see, e.g., the delta-^{18}O records of *Cobb et al.,* 2003). However El Niño had already initiated prior to the eruptions of El Chichón and Pinatubo [e.g., *Robock et al.* 1995; *Self et al.*, 1997].

Volcanic aerosol-induced heating of the tropical stratosphere may also enhance the pole-to-equator temperature gradient. In Northern Hemisphere winter this larger temperature gradient produces a stronger polar vortex, and a corresponding stationary wave pattern of tropospheric circulation, pushing the system into a positive North Atlantic Oscillation/ Arctic Oscillation (NAO/AO) circulation pattern [*Robock,* 2000]. NAO/AO may also be changed by the heating reduction due to depletion of

stratospheric ozone by volcanic aerosols [*Stenchikov,* 2002]. To add further complexity, NAO/AO is correlated with AMOC [*Otterå et al*., 2010; *Zanchettin et al.*, 2012], which is separately related to volcanic aerosol loading through the hydrologic cycle link mentioned above.

One recent study also suggest that the index of Atlantic Multidecadal Variability (AMV) may also influence the quantification of volcanic cooling [*Canty et al*., 2013]. After detrending the AMV index, the volcanic cooling becomes approximately one half of the original value. AMV is one of the dominant SST patterns over the Atlantic Ocean on multidecadal time scale. On multidecadal to centennial time scales, AMOC and AMV is closely correlated with each other with a correlation coefficient; however, there has been continuous discussion of the causative link between these two [*Knight et al*., 2005; *Msadek and Frankignoul*, 2009; *Wouters et al*., 2012; *Drijfhout et al*., 2012]. These connections suggest further links between volcanic aerosols and the background climate which we examine.

2.2 Data and methods

2.2.1 Description of CMIP5 models

Here we briefly describe the ensembles of simulations from eight models used in this study (listed in **Table 2.2**). All models are driven by both natural and anthropogenic forcings. In addition, for two models we have ensemble members that lack volcanic forcing. Each ensemble member begins with different initial conditions, and in our study, we are interested in the period 1871-2005.

Table 2.2. Some basic information about historical simulations examined in this study: name, source of aerosol loading, ocean model resolution(longitude × latitude

× vertical), and the number of ensemble members using all forcing, and the number that do not include volcanic aerosols.

Name	Aerosol source	Ocean resolution	Ensembles
CCSM4	*Ammann et al*. [2003]	$1^\circ \times (0.27^\circ \sim 0.54^\circ) \times 60 lev$	6/4
GFDL-CM3	*Sato et al.* [1993]	$1^\circ \times (1/3^\circ \sim 1^\circ) \times 50 lev$	5/3
GFDL-ESM2G	*Sato et al.* [1993]	$1^\circ \times (1/3^\circ \sim 1^\circ) \times 63 layers$ *	3/0
GFDL-ESM2M	*Sato et al.* [1993]	$1^\circ \times (1/3^\circ \sim 1^\circ) \times 50 lev$	2/0
HadCM3	*Sato et al.* [1993]	$1.25^\circ \times 1.25^\circ \times 20 lev$	10/0
HadGEM2-ES	*Sato et al.* [1993]	$1^\circ \times (1/3^\circ \sim 1^\circ) \times 40 lev$	4/0
MPI-ESM-LR	*Sato et al.* [1993]	$1.5^\circ \times 1.5^\circ \times 40 lev$	3/0
MRI-CGCM3	*interactive***	$1.0^\circ \times 0.5^\circ \times 51 lev$	3/0

* the 63 layers are remapped onto 50 fixed depth levels for analysis.
** *Driscoll et. al.* [2012]

1) The National Center for Atmospheric Research Community Climate System Model, version 4 (CCSM4) atmospheric component model has a resolution of 0.9° × 1.25° lat-lon and 26 vertical levels (L26), with a top of 2.9 mb [*Gent et al*., 2011]. The ocean model uses Parallel Ocean Program (version 2) with 0.9° × 0.27-0.54° L60 resolution, a displaced North Pole, and a coupled sea ice model (true of all models considered here). CCSM4 uses volcanic aerosols provided by *Ammann et al.* [2003], which are roughly 20 to 30% larger in AOD than the estimates of *Sato et al*. [1993] [*Solomon et al.,* 2007]. Here we examine an ensemble of six historical simulations with full natural and anthropogenic forcing and four that exclude volcanic aerosols.

2) We consider three models from the Geophysical Fluid Dynamics Laboratory (GFDL). The first is the Climate Model Climate Model version 3 (CM3). The atmospheric component model has a resolution of 2.0° × 2.5° L48, with

a model top of 0.01 mb. We shall see that aerosol effects are particularly strong in this model. The ocean component model is built on Modular Ocean Model version 4.1 (MOM4.1) numerics with approximately $1^\circ \times (1/3^\circ \sim 1^\circ) \times 50 lev$ longitude× latitude and vertical resolution and a tripolar grid [*Griffies et al.,* 2011]. We examine five ensemble members of the historical simulations and an additional three that exclude volcanic aerosols.

3) The second is the GFDL Earth System Model GFDL-ESM2M (*Dunne et al.,* 2012) which incorporates the coarser atmospheric vertical resolution $2.0^\circ \times 2.5^\circ \times 24 lev$. The ocean component is MOM4.1 ocean, as used in the previous Climate Model version 2.1 [*Stenchikov et al.,* 2006, 2009]. We examine two ensemble members driven by historical forcing.

4) The third in this series, GFDL-ESM2G, differs from GFDL-ESM2M mainly in that is uses the Generalized Ocean Layered Dynamics (GOLD) isopycnal coordinate ocean model with a somewhat higher resolution $1^\circ \times (1/3^\circ \sim 1^\circ)$ horizontal grid and 63 layers [*Dunne et al.,* 2012]. We should expect such an ocean to have much reduced unphysical vertical diffusion compared to GFDL-ESM2M. We have three ensemble members of the historical simulations of GFDL-ESM2G.

5) We consider two models produced by the Hadley Centre. The first, the Hadley Centre Coupled Model, version 3 (HadCM3), has an atmosphere with $2.5^\circ \times 3.75^\circ \times 19 lev$ resolution with top pressure 5 mb resolution [*Jones et al.,* 2003]. The HadOM3 ocean model has $1.25^\circ \times 1.25^\circ \times 20 lev$ resolution. We examine 10 ensemble members driven by historical forcing.

6) The second Hadley Center model we consider is the Hadley Centre Global Environmental Model version 2 - Earth System (HadGEM2-ES) with a somewhat higher resolution atmosphere ($1.25^\circ \times 1.875^\circ \times 38 lev$, with top pressure 3 mb) and ocean $1^\circ \times (1/3^\circ \sim 1^\circ) \times 40 lev$ [*Collins et al*., 2011]. We examine four ensemble members driven by historical forcing.

7) The Max Planck Institute - Earth System Model - Low Resolution (MPI-ESM-LR) atmosphere model, known as ECHAM6, has $1.875^\circ \times 1.875^\circ \times 47 lev$ resolution with top pressure 10 mb. The MPIOM ocean model uses a bipolar orthogonal spherical coordinate system with approximately $1.5^\circ \times 1.5^\circ \times 40 lev$ resolution [*Mauritsen et al*., 2012]. We examine three ensemble members driven by historical forcing.

8) The final model we consider is the Meteorological Research Institute Coupled General Circulation Model version 3 (MRI-CGCM3). The MRI-AGCM3 atmosphere has $1.125^\circ \times 1.125^\circ \times 48 lev$ resolution, and is notable for having a high top at 0.01 mb. The ocean-ice model is the MRI Community Ocean Model Version 3 with a tripolar grid and approximately $1.0^\circ \times 0.5^\circ \times 51 lev$ resolution [*Yukimoto et al*., 2012]. For MRI-CGCM3, like MPI-ESM-LR, we have a more limited ensemble member set of three historical ensemble members.

Most of the ocean component grids are irregular. For this comparison all ocean variables have been remapped onto a regular 1° × 1° horizontal grid using the same conservative mapping routine. All data are monthly averaged, and a seasonal cycle has been removed from each ensemble member as well as from the observation sets used for comparison. In some situations when examining the impact of volcanic

eruptions on subsurface temperature a centennial trend has also been removed in order to reduce the impact of centennial warming associated with greenhouse gasses on the multidecadal response to volcanoes.

2.2.2 Methods and observational data

While the emphasis in this study is on examining the model's behavior, we do include brief comparison to historical temperature observations. Simulated SST and subsurface heat content for the top 1 km of the ocean ($\rho C_p \int_{-1000m}^{0} T dz$) is represented here by the temperature anomaly from its climatological annual average, since r and C_p are essentially constant. The layer from 1 to 2 km depth is represented in the same way. The heat contents are compared to the Simple Ocean Data Assimilation version 2.2.4 reanalysis estimates of *Carton and Giese* [2008]. SST is provided by HadISST1 (Hadley Centre Sea Ice and Sea Surface Temperature) (*Rayner et al.,* 2003). The algorithms used to estimate SST from satellite infrared radiances are themselves quite sensitive to aerosol loading, with corrections in excess of 0.4 K. This connection between the phenomena and observing system means that satellite infrared SST observations of the ocean's response to El Chichón and Pinatubo must be viewed cautiously [*Zhang et al.,* 2004].

2.2.3 Rotated Extended Empirical Orthogonal Functions analysis

The response of SST to an eruption is approximately a factor of ten less than the SST variations associated with ENSO in the tropical Pacific and so it would require averaging 100 ensemble members to suppress an uncorrelated ENSO signal simply

by ensemble averaging in this region. Lacking so many ensemble members we carry out this separation by adopting the method of *Guan and Nigam* [2008] to identify the buildup and decay phases of ENSO and then ensemble average those time series, looking for a temporal relationship between the evolution of ENSO in the ensemble average and the timing of the eruptions. The method of *Guan and Nigam* involves computing the rotated extended empirical orthogonal functions (REEOFs) of SST in the Pan-Pacific domain (20°S-60°N, 120°E-60°W) for each ensemble member (seasonal cycle removed). We then associate the first two REEOFs with the canonical ENSO decay and buildup phases, so that by averaging the REEOFs associated with individual ensemble members we can isolate the ENSO signal in the ensemble averages. This method is also applied to filter the impact of the ENSO buildup phase and the decay phases from surface ocean variables such as SST and sea surface salinity (SSS).

2.3 Global response to volcanic eruptions

2.3.1 Atmospheric response to volcanic eruptions

We begin by examining global averaged atmospheric variables, identifying the response to volcanic aerosols by comparing average conditions during the six years prior with average conditions in the years following each eruption. Of the five eruptions, Krakatau causes the strongest reduction of ocean surface net surface shortwave flux (**Figure 2.1**).

For this eruption on average the all-sky shortwave flux is reduced by 4.5 W m^{-2}, a reduction followed in size by Pinatubo with a reduction of 3.4 W m^{-2}. In contrast the

weakest, Agung and El Chichón, reduced all-sky shortwave radiation on average by 2.0 W m^{-2}. Among the eight models CCSM4 has the greatest reduction, especially for Santa Maria, whose annual average all-sky shortwave radiative forcing in CCSM4 was reduced by average of 5.5 W m^{-2}. The large reduction in this case is likely due to the use in CCSM4 of *Ammann et al* [2003] aerosol loading estimates. The reductions of all-sky radiation (which include cloudy regions) are about 70% of the clear-sky

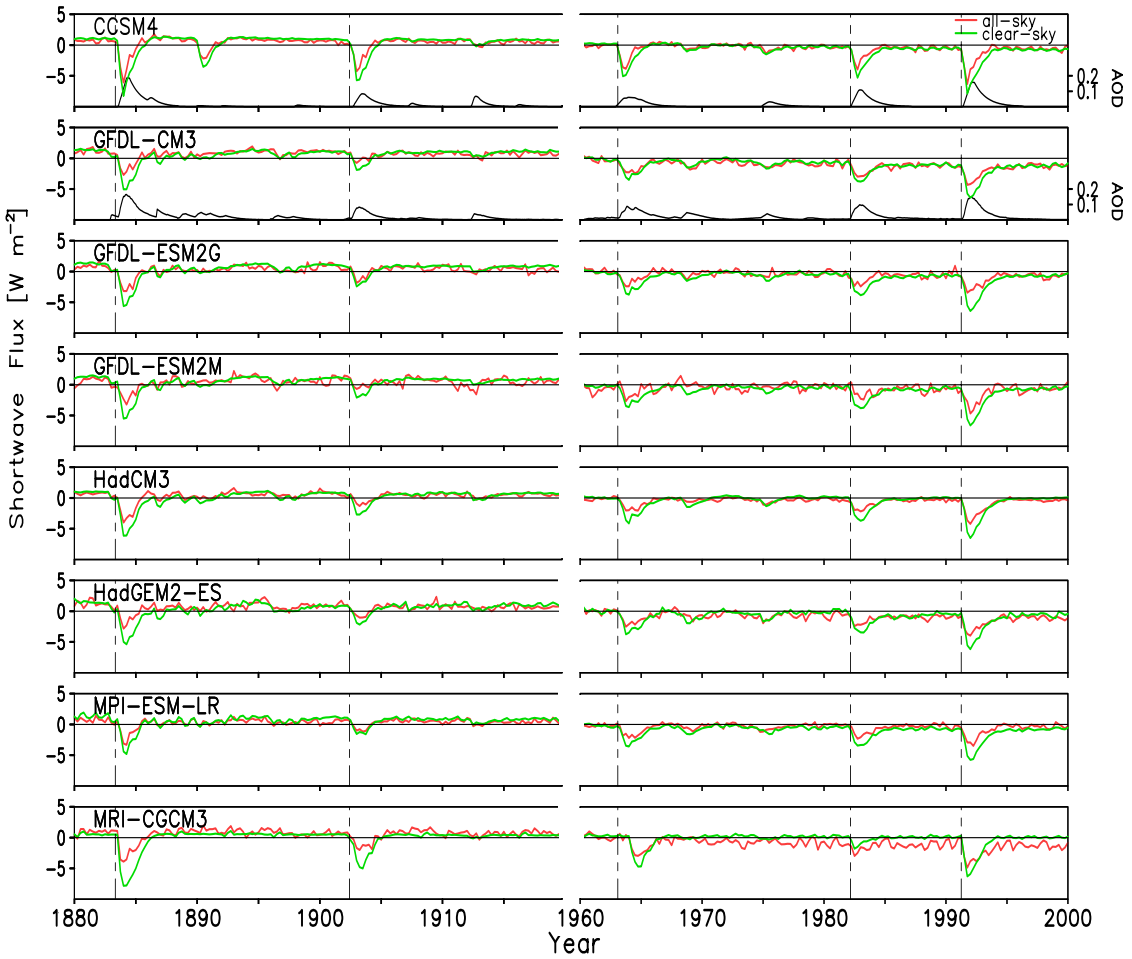

Figure 2.1. Global average all-sky and clear-sky downwelling surface shortwave flux anomalies (red and green) from the ensemble means of each of the eight models (Units: W m^{-2}). Black curves show aerosol optical depth of *Ammann et al.* [2003] (top panel, scale on right) and *Sato et al.* [1993] (second panel, scale on right). Dashed lines show the starting time of the five eruptions (in chronological order: Krakatau, St. Maria, Agung, El Chichón, and Pinatubo).

reductions in all models, which is comparable to the results in *Stenchikov et al.* [1998]. This fairly constant ratio is surprising since global mean cloud fraction varies widely among models, ranging from 50% in CCSM4 and HadCM3 to over 70% in GFDL-CM3. Surprisingly also, the global mean cloud fraction does not show a pronounced volcanic signal, except in CCSM4.

All ensemble members show significant variability associated with ENSO. The buildup and decay phases of ENSO in the ensemble averages are shown in **Figure 2.2**. GFDL-ESM2M (which only has two ensemble members) and MRI-CGCM3 show buildup and decay phases of El Niño associated with the Pinatubo eruption although in both cases the buildup began prior to the eruption. Several other models; CCSM4, HadCM3, MPI-ESM-LR; show an El Niño even further in progress when the eruption occurred. A different set of models: CCSM4, HadGEM2-ES, and MRI-CGCM3, show development of a small to medium sized El Niño in the year following Krakatau, while GFDL-ESM2G shifts into the La Niña phase. The evidence of a connection to the other eruptions is even weaker. If we accept the average of the eight model ensembles as our most stable estimate of how the climate responds to volcanic aerosols (treating each model as equally valid) then the lack of a coherent ENSO signal suggests there is no compelling evidence of a link between the timing of an eruption and a shift in phase of ENSO. We have made a similar effort to examine the relationship between the volcanic eruptions and the phase of NAO in boreal winter sea level pressure (not shown) and found similarly tenuous connections.

We next examine the changes in surface variables in response to the eruptions by comparing the global average values for the years following the eruption with the six-

year average prior to the eruptions. Surface net outgoing longwave flux and latent heat loss both show a negative anomaly with a lag of a year or so (resulting from their connection to SST). As a result of this lag and their lower amplitudes, the surface heat flux anomaly following the eruptions is dominated by the impact of the

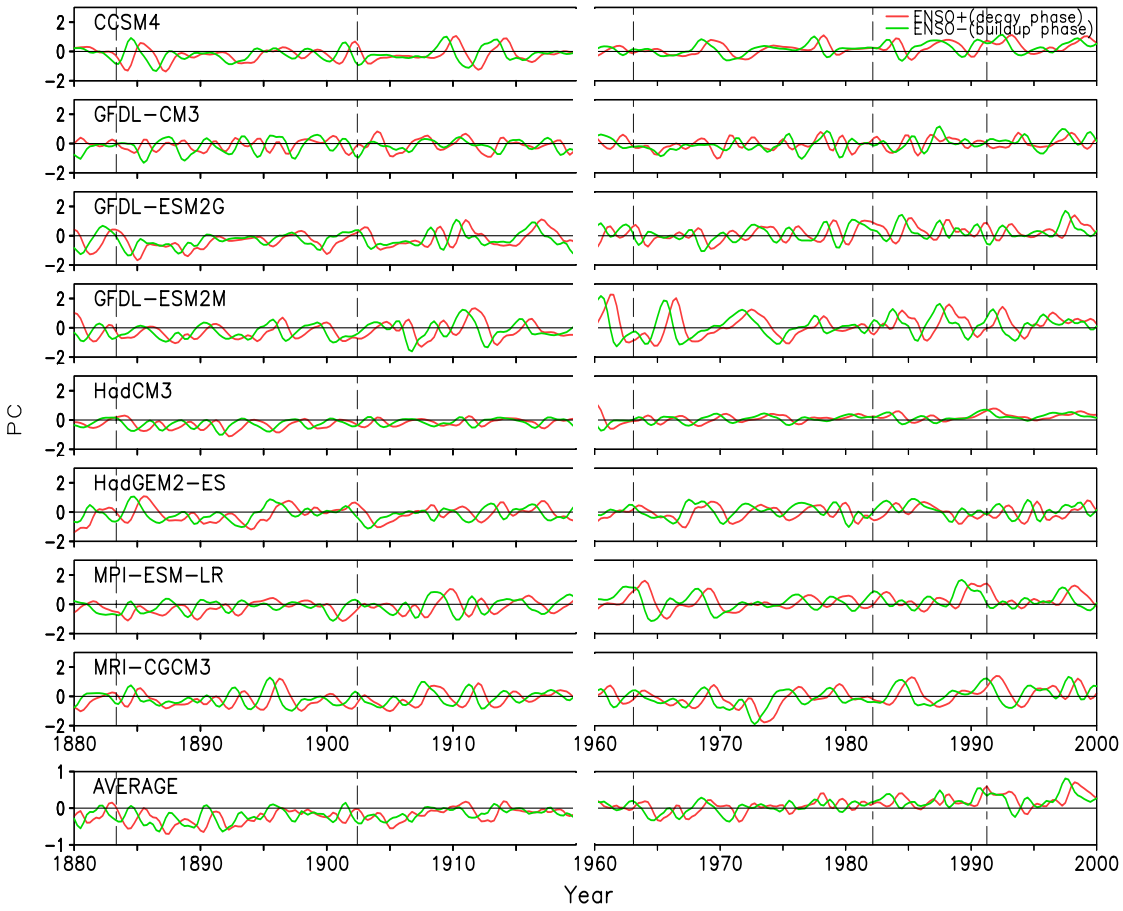

Figure 2.2. Ensemble means of the REEOF first (red, decay ENSO phase) and second (green, buildup ENSO phase) principle components after removal of the climatological seasonal cycle. Dashed lines show the starting time of the five eruptions (in chronological order: Krakatau, St. Maria, Agung, El Chichón, and Pinatubo). Lowest panel shows the average of the time series for all the model ensembles. No trend has been removed.

immediate reduction in net shortwave radiation, with the strongest response associated with Krakatau followed by Pinatubo of statistical significance (**Figure 2.3**

lower right). Of the different models we consider CCSM4 has the largest net flux reduction, particularly for Krakatau and Santa Maria. MRI-CGCM3 seems to be almost missing El Chichón, and its response to Agung is delayed by a year because the volcanic aerosol forcing data are different from Ammann's and Sato's analysis. The recovery time for all models is three years or so, reflecting the atmospheric lifetime of stratospheric sulfate aerosols.

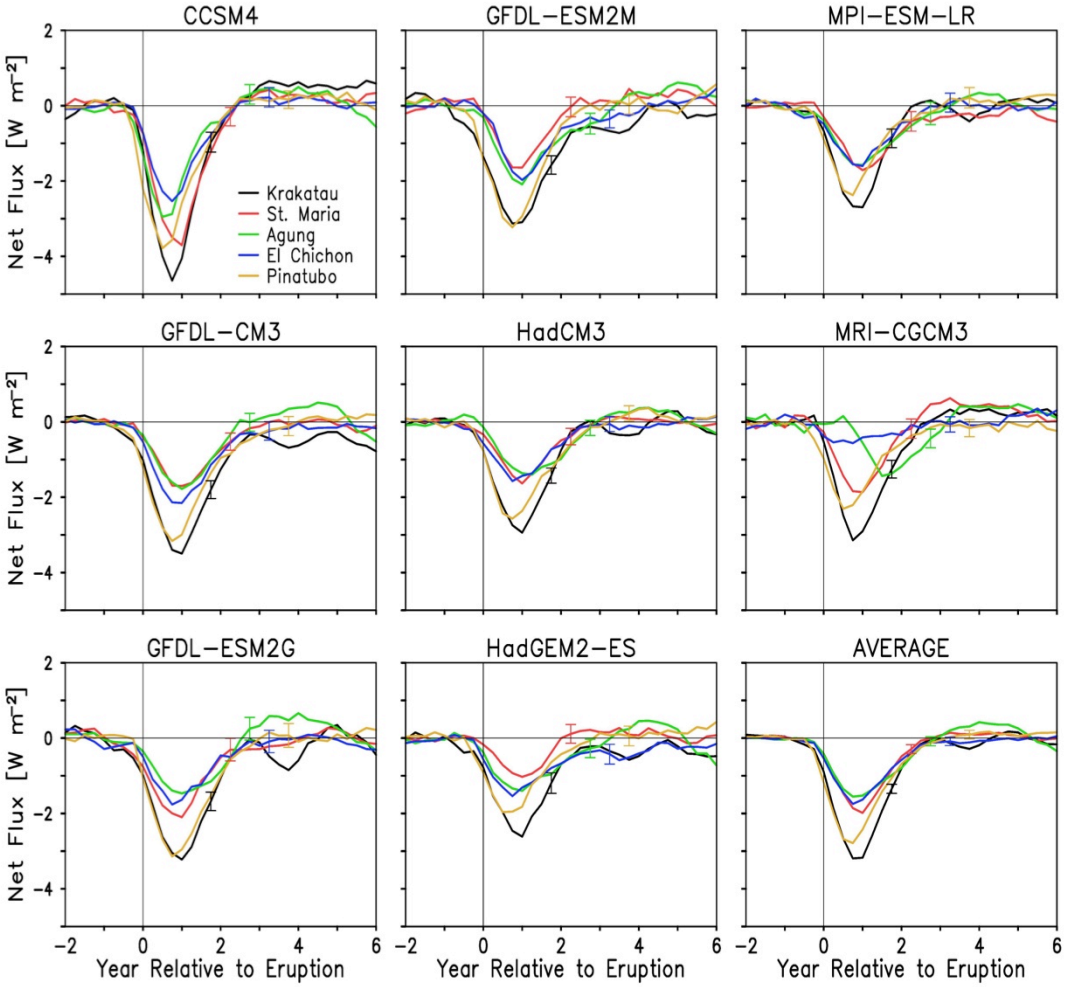

Figure 2.3. Ensemble mean global net surface heat flux anomalies from the six-year average prior to each eruption. The seasonal cycle and the ENSO signal have been removed separately from each, and the time series are then smoothed with a running four-season average. Bars show the stand error from the ensemble mean. Lower right-hand panel shows the average of all the ensembles for each eruption.

2.3.2 Oceanic response to volcanic eruptions

We next turn our attention to the oceanic response. The lowest SSTs occur 1-2 years following each eruption (**Figure 2.4**). Among the eruptions we consider the maximum seasonal cooling of -0.2 to -0.4 K is associated with Krakatau, values reasonably consistent with the (poorly constrained) observed estimates shown in the lower right-hand panel. Combining this cooling estimate with the net surface flux anomalies shown in **Figure 2.3** allows us to estimate an effective mixing depth over which the cooling from Krakatau is distributed, of about 85 m. For some models the Santa Maria and El Chichón eruptions elicit fairly weak responses in SST, the latter likely because its aerosol loading is significantly lower than the others.

The relaxation time of SST back to its pre-eruption value is ~5-7 years, a little longer than the recovery time of surface net fluxes (**Figure 2.3**). Among the volcanoes we consider, Krakatau is again unusual in that SSTs remain depressed (although the response to Krakatau may be affected by additional aerosol loading from the 1886 Tarawera eruption that followed Krakatau, **Figure 2.1** upper panel). Although correcting for ENSO generally makes the Pinatubo signal stronger (comparing **Figure 2.4** and **Figure 2.5**), Pinatubo still has a weaker SST response than Krakatau in several of the models. Models high equilibrium climate sensitivity, like HadGEM2-ES, GFDL-CM3, and MPI-ESM-LR [*Andrews et al.* 2012], are sensitive to volcanic forcing as well. For example, with ~ 2.5 W m^{-2} net flux decrease after Krakatau, SST is reduced by ~ 0.27 K in HadGEM2-ES.

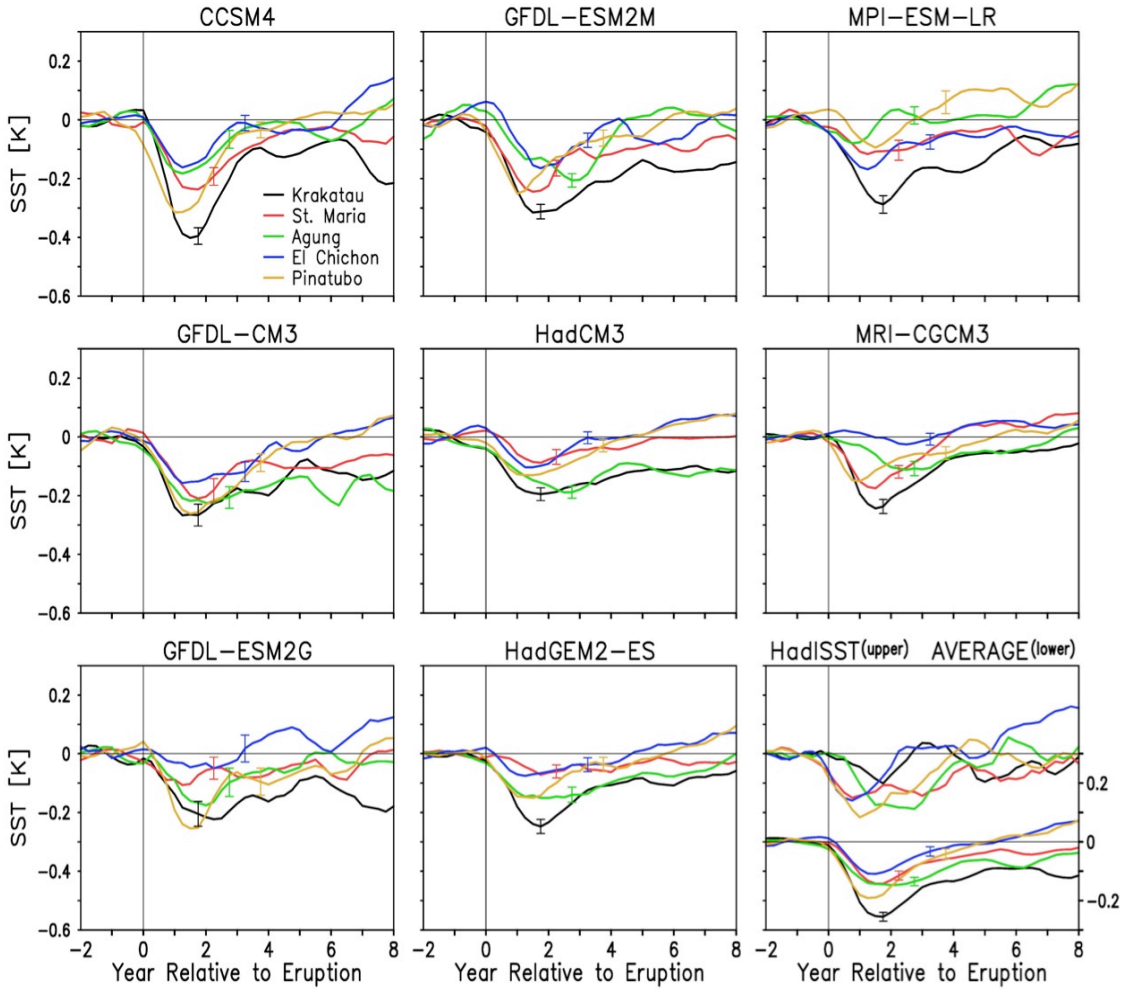

Figure 2.4. Ensemble mean global average SST anomaly from the six-year average prior to each eruption (similar to **Figure 2.3**). The seasonal cycle and the ENSO signal have been removed separately from each, and the time series have then been smoothed with a running four-season average. Lower right-hand panel shows observed SST processed in the same way (y-axis same as other panels) and the average SST of all ensembles with y-axis on the right. Bars show the stand error from the ensemble mean.

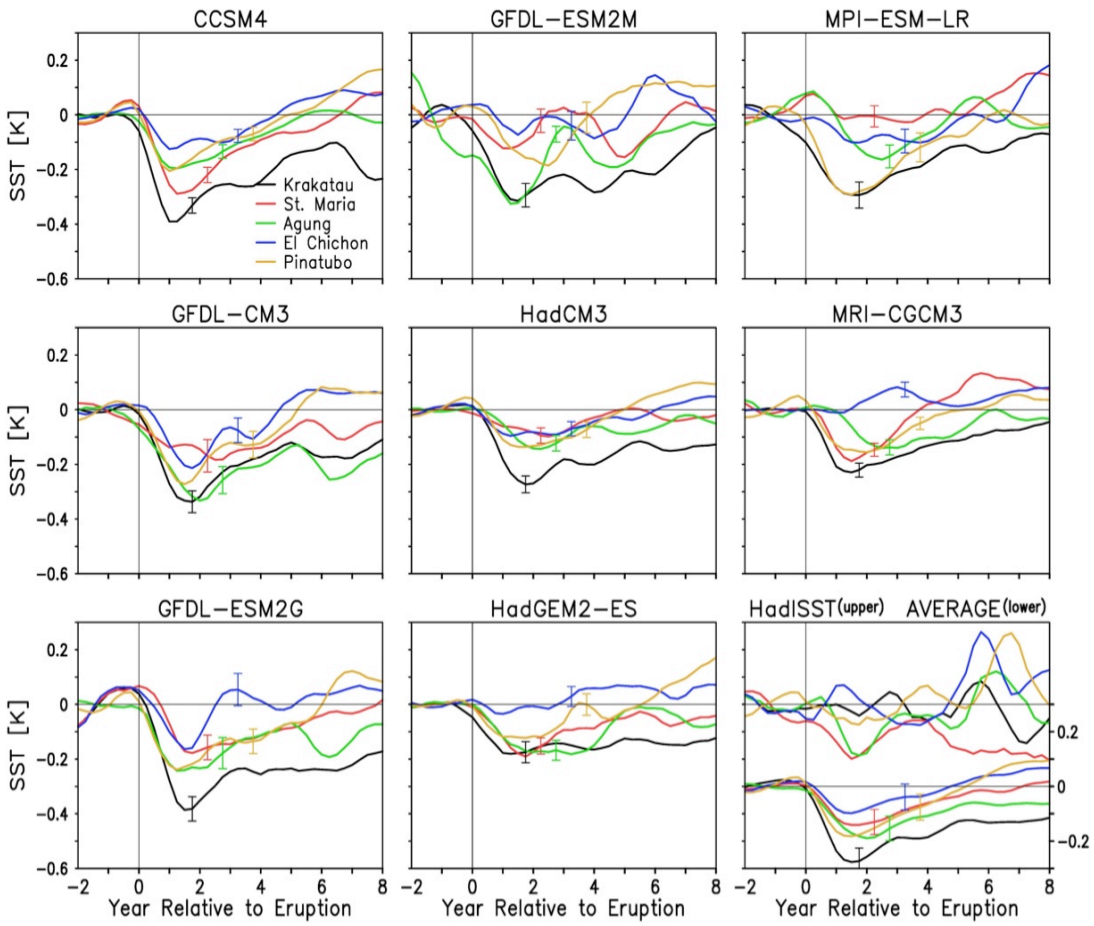

Figure 2.5: Similar to **Figure 2.4** except that the ENSO signals are not filtered out.

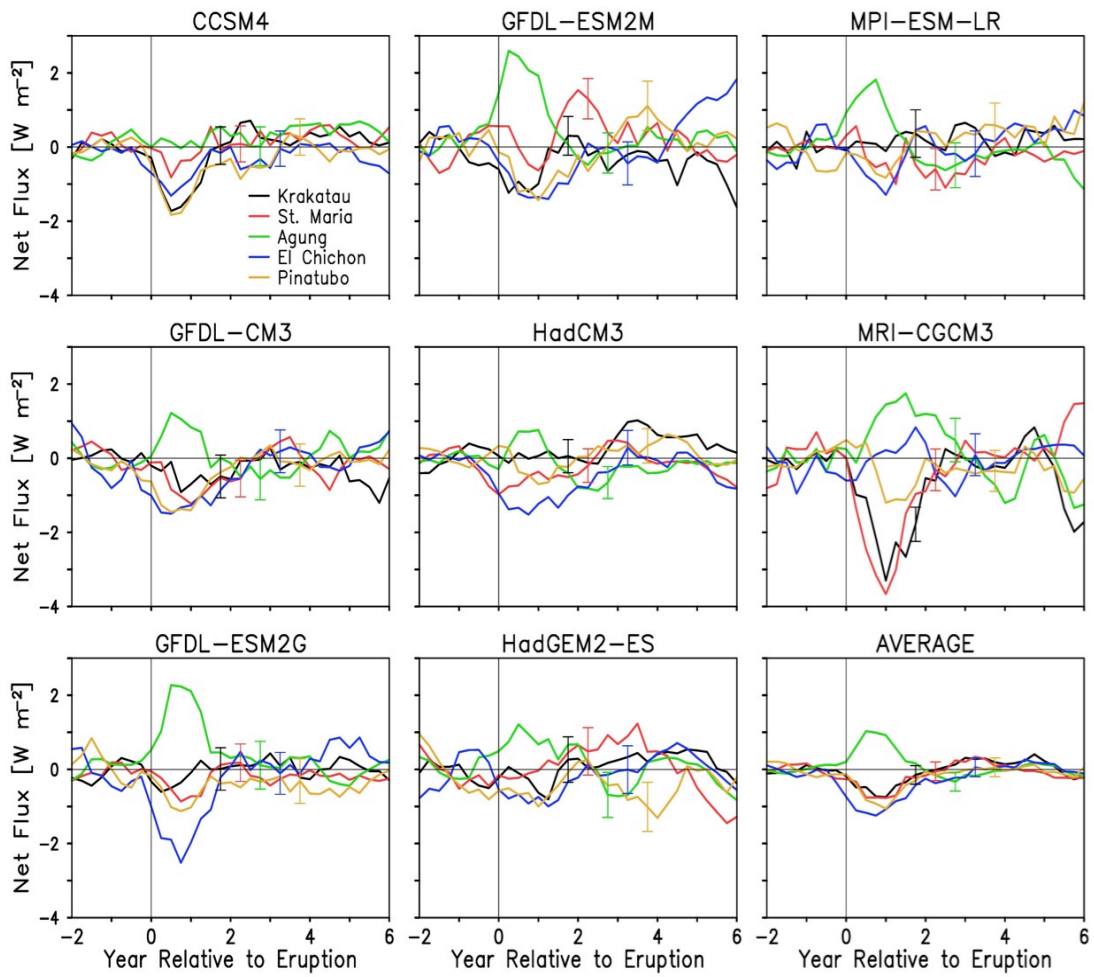

Figure 2.6. Ensemble mean net surface heat flux difference between Northern and Southern Hemispheres (Northern minus Southern Hemisphere) from the six-year average difference prior to each eruption (similar to **Figure 2.3**). Units are W m^{-2}. The seasonal cycle and the ENSO signal have been removed separately from each, and the time series have then been smoothed with a running four-season average. Lower right-hand panel shows the average of all model ensembles for each eruption. Bars show the stand error from the ensemble mean.

The hemisphere in which eruptions occur alters the strength of the ocean response because of the weakness of cross-equatorial stratospheric aerosol exchange and the greater land mass in the Northern Hemisphere. For example, the sulfate aerosols from Agung were four times larger in the Southern Hemisphere than in the Northern Hemisphere, while El Chichón put twice as much aerosol loading into the Northern

Hemisphere as into the Southern Hemisphere [*Sato et al.,* 1993]. This positive interhemispheric difference (Northern minus Southern Hemisphere) in net surface heat flux due to Agung is evident to some extent for all the eight models (**Figure 2.6**). The asymmetry is most evident in the two GFDL-ESM models.

We note one additional impact of aerosols on the surface ocean: an increase in SSS following the eruptions, which we believe is associated with multi-year aerosol-induced changes in the atmospheric hydrologic cycle. This effect is most evident in the North Atlantic subpolar gyre, two examples of which are shown for Krakatau (**Figure 2.7**).

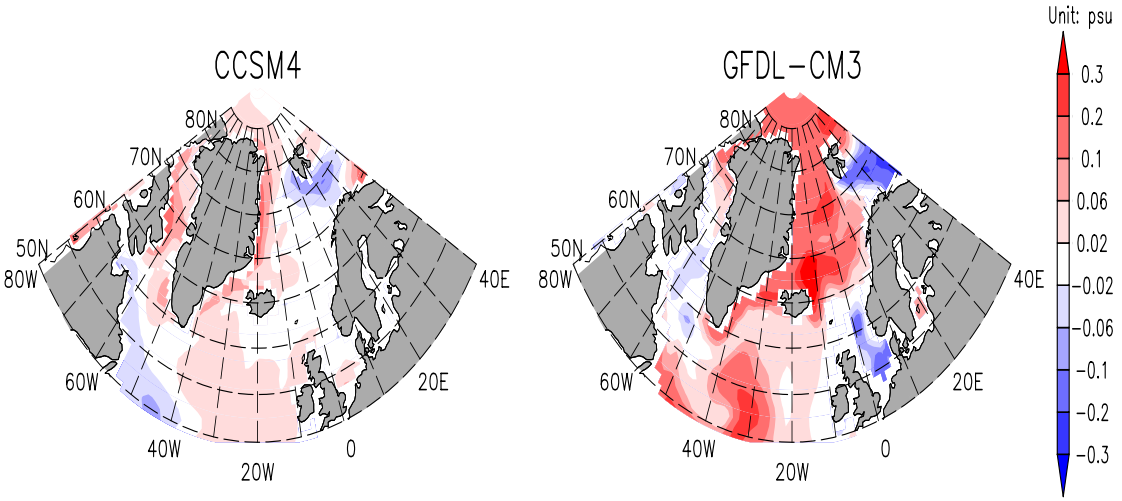

Figure 2.7. Ensemble mean sea surface salinity (units: psu) in the northern Atlantic sector for the two years following the Krakatau eruption minus the six year average prior to eruption. Two models are shown: CCSM4 (left panel) which has a weak AMOC response to volcanic eruptions, and GFDL-CM3 (right panel) which has a strong AMOC response to volcanic eruptions.

We next consider the response of the subsurface ocean, beginning by examining the global average ocean heat content (**Figure 2.8**). By focusing on the global average we eliminate the impact of horizontal heat transport convergence. The

climate drift in pre-industrial controls runs are less than 0.025 K/100yr in the upper 1000m, much smaller than the increase in historical runs. The response in heat content to the eruptions is quite evident in the upper 1000m, but not at deeper levels. In the upper 1000m average temperature is depressed for multiple decades by as much as 0.03K, comparable to observations. For HadCM3 the accumulated effect of Krakatau and Santa Maria may have obscured the anthropogenic warming trend for a century! On such long time-scales the anomalies due to volcanic aerosols cannot easily be separated from the centennial 0-1000 m warming trend, which in this model is 0.3-0.4 K per century (equivalent to ~4 x10^{23} J per century).

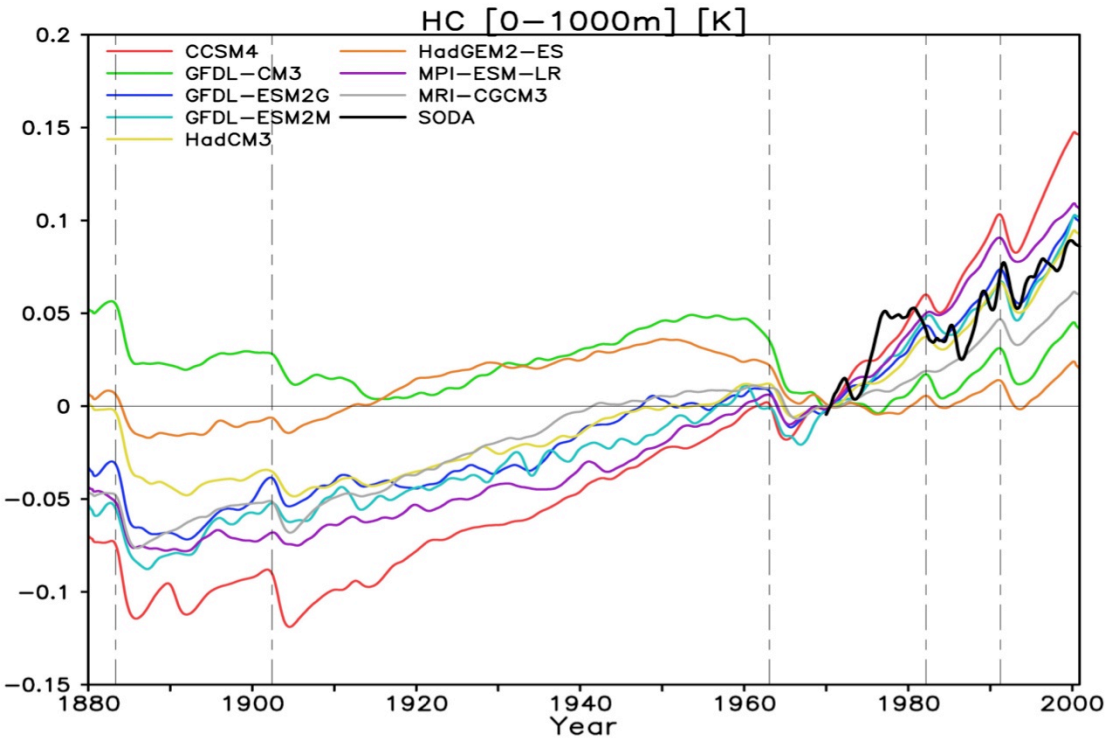

Figure 2.8. Ensemble mean two-year running averaged global ocean heat content anomalies (0/1000m) from both models and SODA (Simple Ocean Data Assimilation) data (units: K). The seasonal cycle of SODA data from 1970 to 2005 is removed from all model outputs and the average of 1970 are subtracted from all data. No linear trend has been removed. Vertical dashed lines indicate the starting time of the five eruptions.

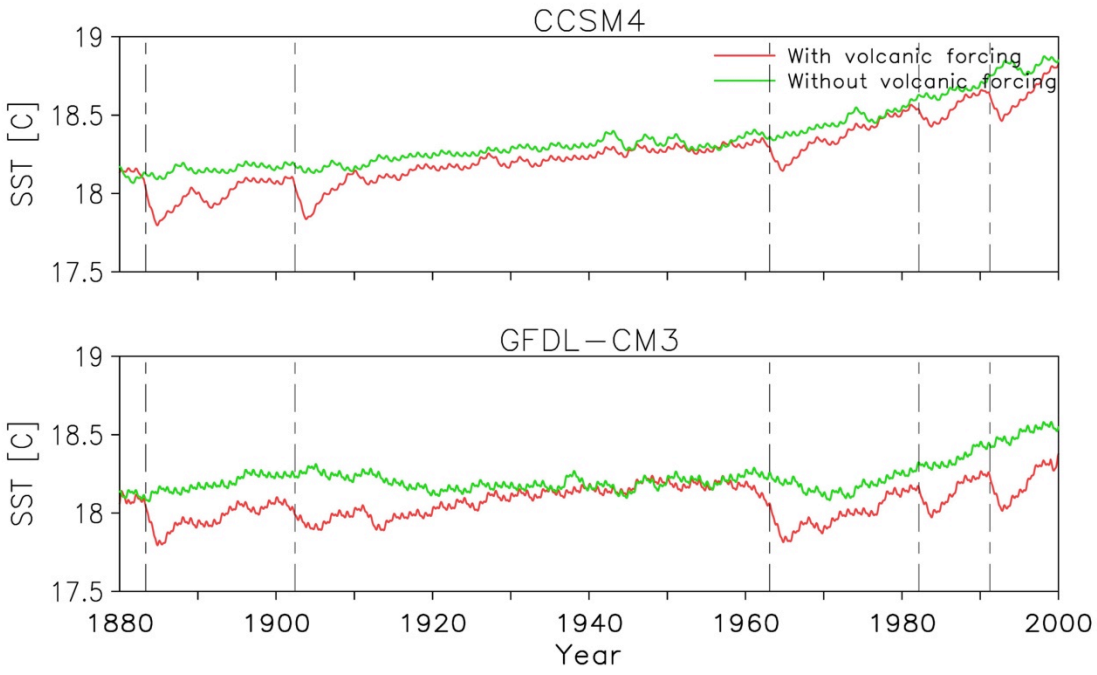

Figure 2.9: Time series of sea surface temperature from CCSM4 and GFDL-CM3 historical runs with and without volcanic forcing.

For two of our models (CCSM4 and GFDL-CM3) we also have historical run ensemble members lacking volcanic aerosols (**Figure 2.9**). Comparison of global SST for the ensemble averages with and without volcanic aerosols confirms that the impact of the eruptions on SST can persist for seven years or more and their concentration at the beginning and end of the 20th century reduces the curvature a quadratic trend of SST (in other words, the *acceleration* of warming) computed over the 20th century.

We next consider the vertical structure of the global average temperature anomalies over the upper 2 km in which it is apparent that the signals associated with the volcanic eruptions are still evident at this depth (**Figure 2.10**). It is also interesting to note that the Krakatau/ Santa Maria and Agung cool anomaly is

particularly prominent and lasts longer in the deep ocean (below 1000m) in GFDL-CM3 and HadGEM2-ES. The presence of the strong volcanically induced cooling is

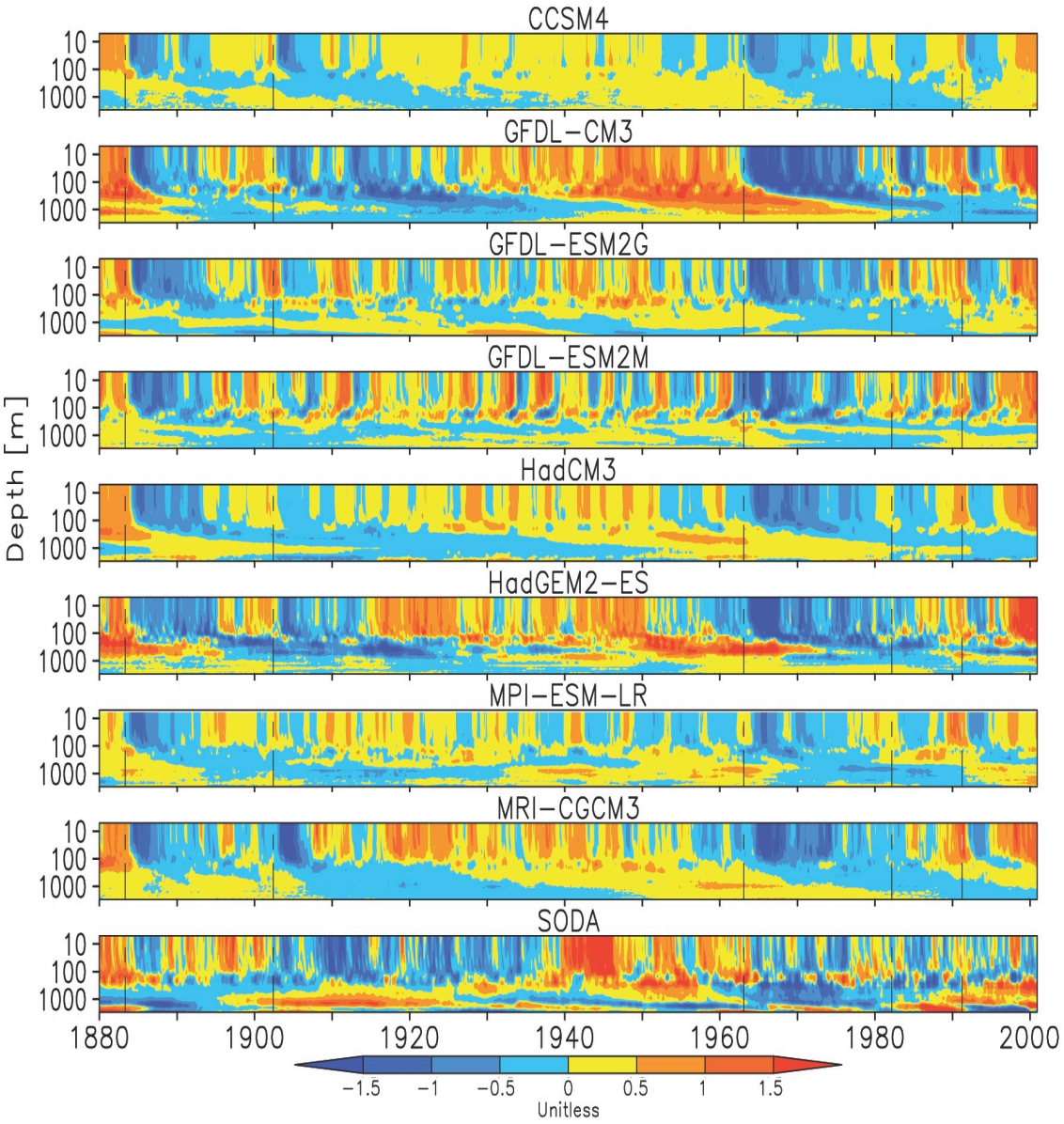

Figure 2.10. Global mean temperature anomaly scaled by the RMS annual temperature variability at each level. A quadratic trend computed separately for each model, at each level, is removed prior to computing anomalies in order to highlight the response to volcanic eruptions. Vertical axis is depth, (units: m).

probably the reason that the centennial warming trends in these two models are the weakest among the models we consider (**Figure 2.8**). Thus for these models the eruptions are masking some of the effects of increasing greenhouse gasses.

2.4 Impact of volcanic eruptions over Arctic and North Atlantic

2.4.1 Impact of volcanic eruptions on Arctic sea ice

Tropical volcanic eruptions also reduce the SST over North Atlantic, although this cooling impact is smaller than the global cooling impact. One of the huge impacts of aerosols on the high latitude ocean is an increase in both Arctic sea ice extent and total mass ranging from a few percent up to 10% within two to three years following an eruption (the sea ice mass change is shown in **Figure 2.11**). This sea ice mass increase persists for years longer than the SST decrease. Among the models we consider MRI-CGCM3 shows the largest changes in sea ice areal extent and GFDL-CM3 shows the greatest change in mass, but these models also have the greatest variability from year to year. Interestingly, the sea ice mass recovery is more rapid after El Chichón and Pinatubo than the previous volcanoes.

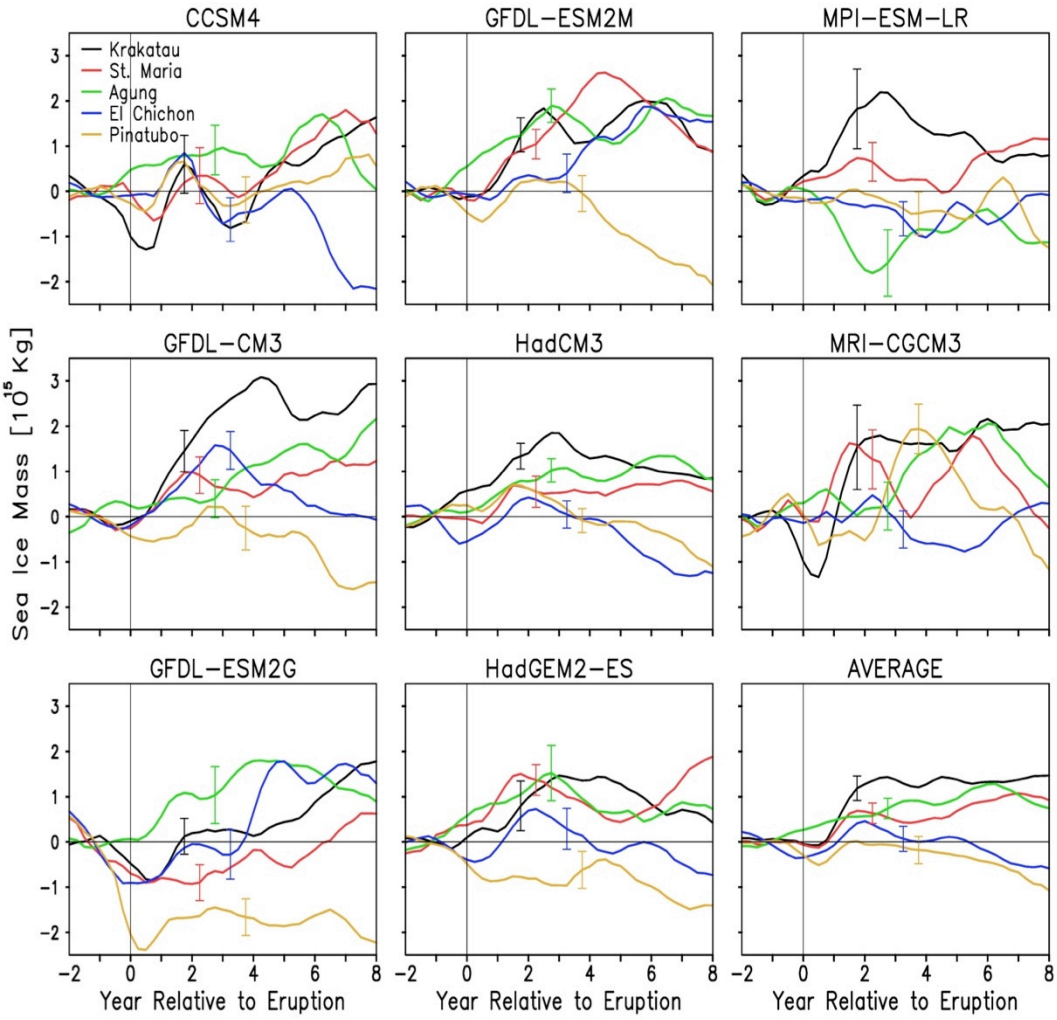

Figure 2.11. Ensemble mean Northern Hemisphere sea ice mass anomaly (0-90ºN) from the six-year average prior to the eruption (similar to **Figure 2.3**) (units: $1x10^{15}$ kg). The seasonal cycle and the ENSO signal have been removed separately from each, and the time series have then been smoothed with a running four-season average. Lower right-hand panel shows the average of all model ensembles for each eruption. Bars show the stand error from the ensemble mean.

2.4.2 Impact of volcanic eruptions on AMOC

The reduction in SST and increase in SSS in response to eruptions has the potential to reduce the stability of the oceanic water column and enhance overturning. Indeed changes in the Atlantic overturning circulation and thus its contribution to

meridional heat transport as suggested by *Stenchikov et al.* [2009] and *Otterå et al.* [2010]. To revisit this issue we define an AMOC index time series as the time series of the maximum value of the zonally integrated volume transport streamfunction

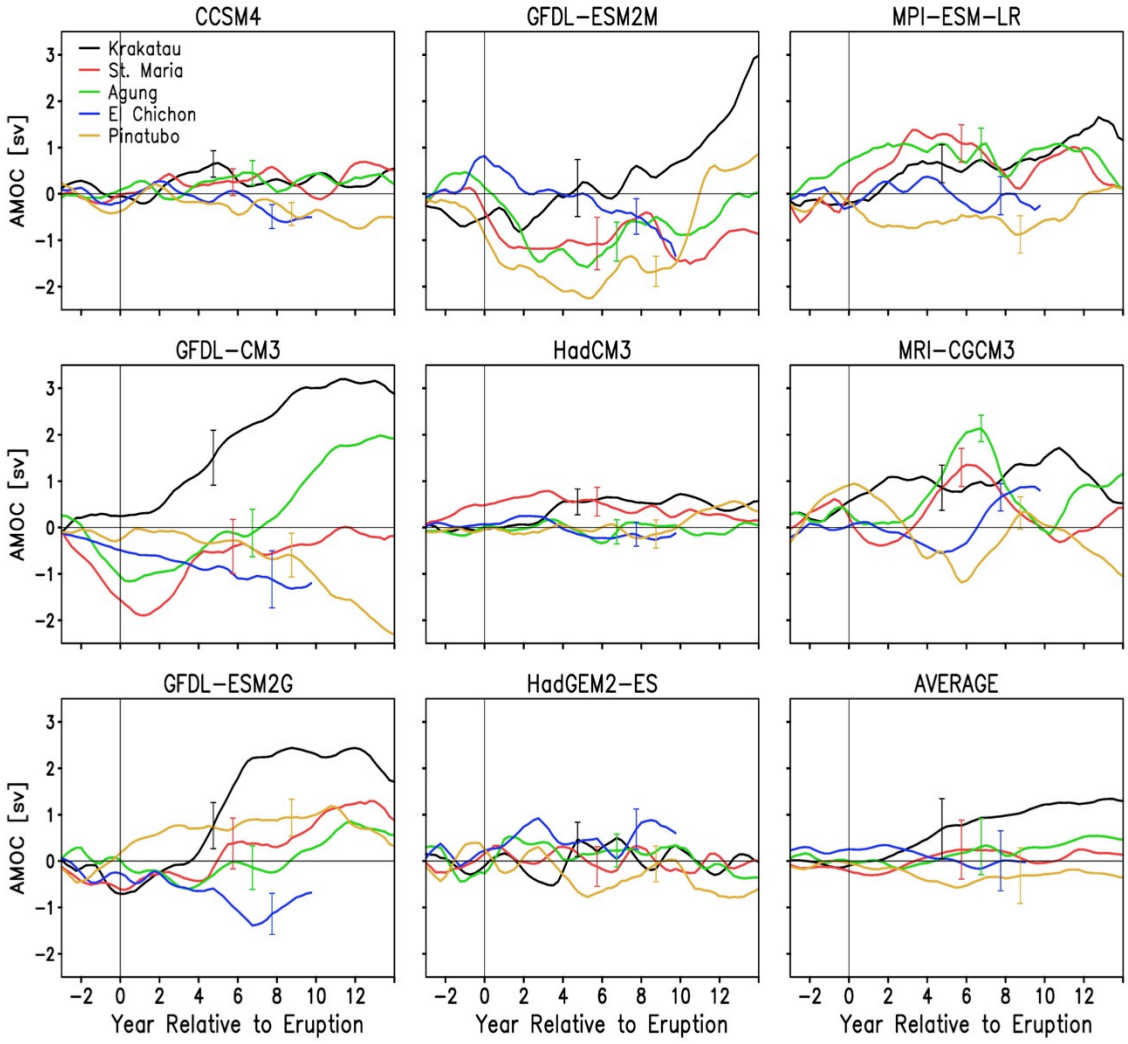

Figure 2.12. Ensemble mean Atlantic meridional overturning streamfunction anomaly from the six-year average prior to each eruption (units: Sv). The time series have been smoothed with a running eight-season average after removal of the climatological seasonal cycle. Lower right-hand panel shows the average of all the ensembles for each eruption. The El Chichón time series are truncated so they do not continue past the 1991 Pinatubo eruption. Bars show the stand error from the ensemble mean.

from 30°N to 60°N (*Otterå et al.* uses a similar definition, except with latitudinal limits of 20°N to 50°N). The time series show AMOC is generally enhanced by volcanic eruptions, but the magnitudes vary, with GFDL-CM3 and GFDL-ESM2G showing transport enhancements of up to 2 Sv (**Figure 2.12**). In contrast, AMOC increases in CCSM4 and HadCM3 are only one quarter to one third as large, perhaps because of its low ocean mixing rates, shows reductions in AMOC transport. The average response is only a small fraction of a Sverdrup.

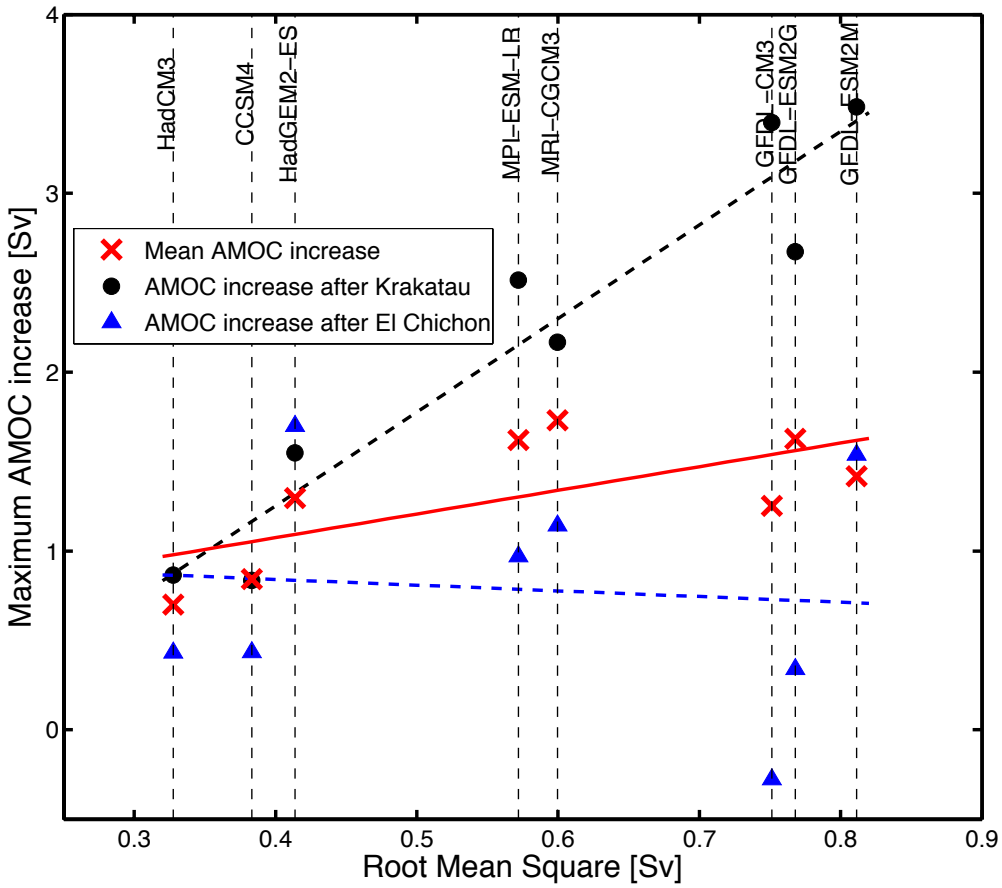

Figure 2.13. AMOC volume transport response to eruptions versus intrinsic AMOC variability. AMOC transport response is the increase during years 7-8 following eruptions versus the natural AMOC RMS annually averaged variability computed during the 41-year gap in huge tropical eruptions 1920 through 1960. Comparisons are shown for the strong Krakatau eruptions, the weak El Chichón eruption, and the average response to the five eruptions.

These differences in AMOC sensitivity to volcanic aerosols seem to reflect the overall variability of AMOC in various models. Those models with low AMOC variability in general show a weak response to volcanoes as well, while those with high variability show strong AMOC transport responses to eruptions (the relationship is most evident for the stronger volcanoes, **Figure 2.13**). The dependence of the sensitivity of AMOC to the model likely explains some of the conflicting conclusions of previous studies noted in Section 1. Comparison of the GFDL-CM3 and CCSM4 ensemble mean results with the simulations excluding volcanic forcing (**Figure 2.14**) are consistent with this model dependence.

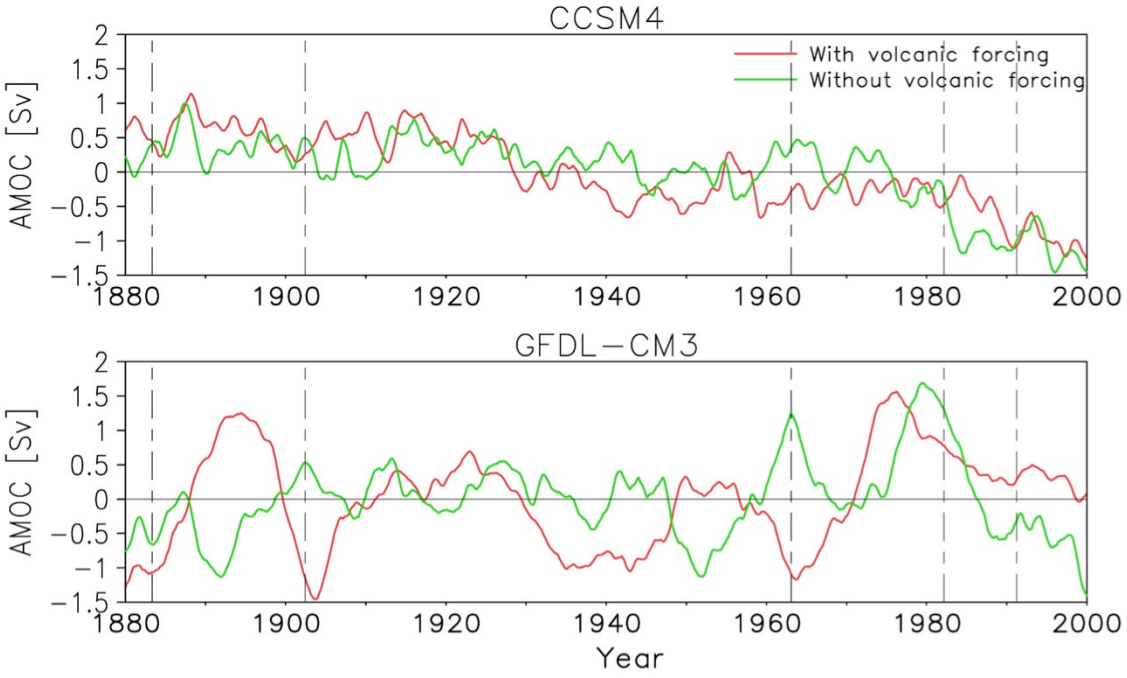

Figure 2.14: Similar to **Figure 2.9** but for AMOC .

The variations in the AMOC time series among different models are reflected in variations in the latitudinal and vertical structure of their stratification and overturning circulation (**Figures 2.15** and **2.16** show the changes in circulation and

stratification in response to Krakatau). The streamfunction change is closely correlated with surface water density change, for which both salinity and temperature variations are important. Models with reduced surface temperature and increased salinity after volcanic eruptions present the most significant AMOC increase. For example, in GFDL-CM3 the sea water density increases extending from surface to several hundred meter deep and from equator to 60°N. As a comparison, in other models, temperature and salinity changes are generally in-phase, which causes a

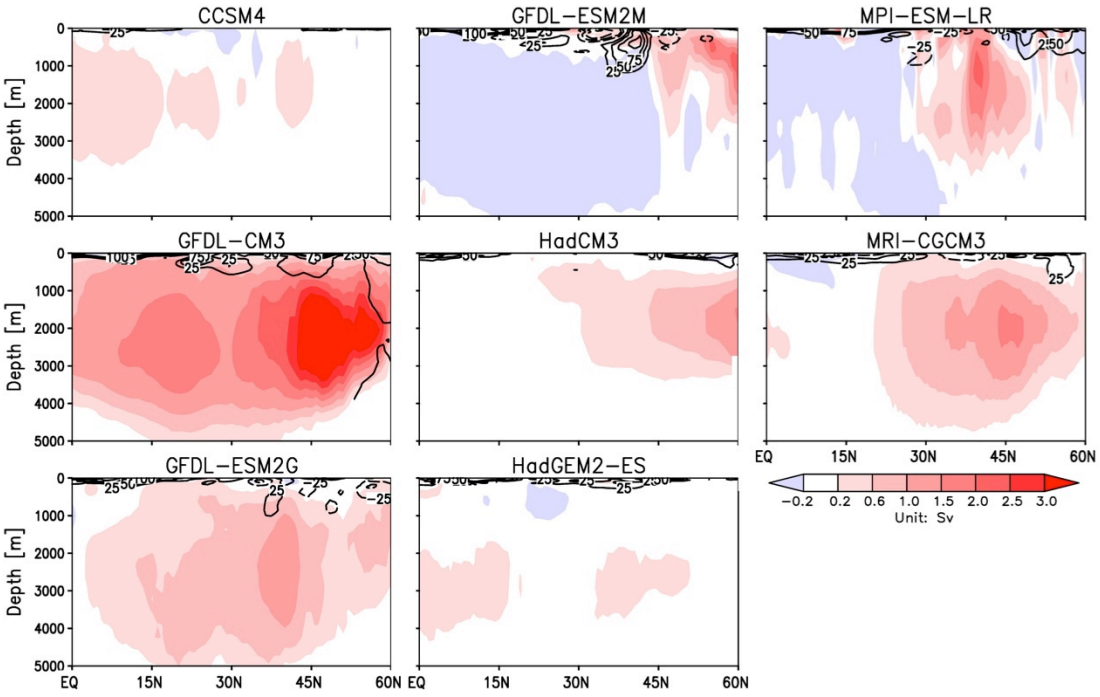

Figure 2.15. Ensemble mean zonal integrated Atlantic meridional overturning transport streamfunction (color, units: Sv) and zonal mean density (contours, CI: 25 g m^{-3}) response to the Krakatau eruption estimated from the difference between the two year average (years 7-8) following the eruption minus the average during the prior six years.

smaller density and streamfuction increase. When temperature and salinity changes are generally in-phase, the relative magnitudes become important. For example, in two GFDL ESM models, the temperature and salinity changes are of larger amplitudes than in other models. The in-phase change between temperature and salinity after volcanic eruptions as well as the relative smaller magnitudes might be the reasons of the low AMOC sensitivity to volcanic eruptions in CCSM4, HadCM3 and HadGEM2-ES.

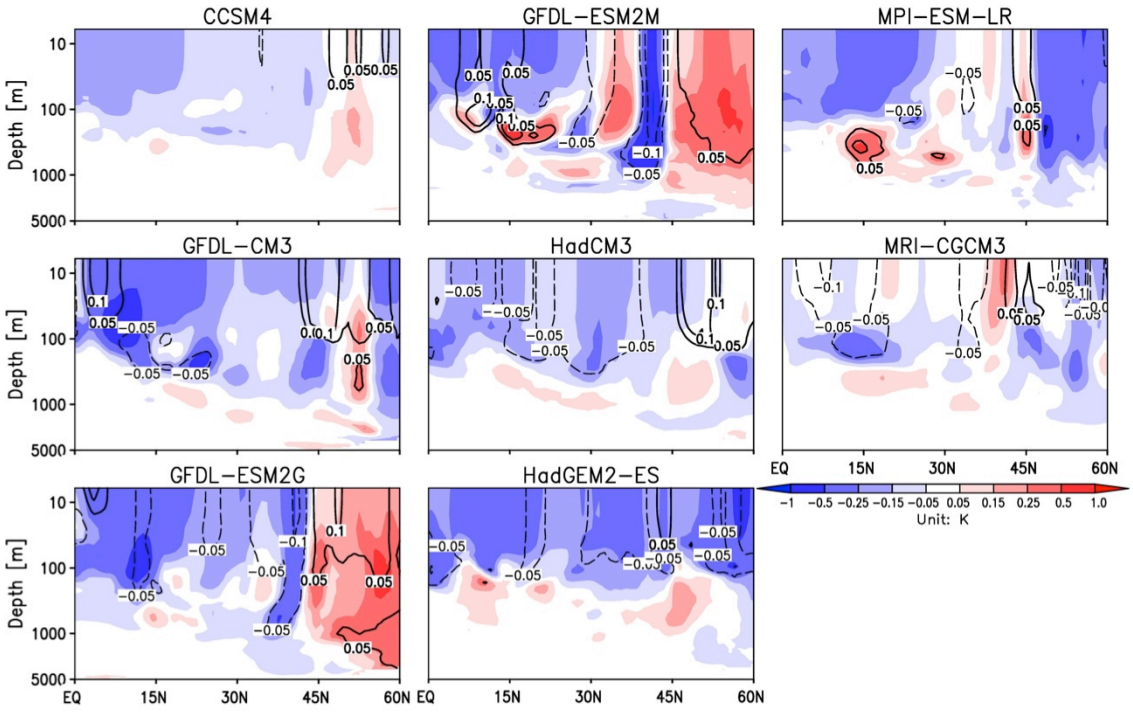

Figure 2.16. Same as **Figure 2.15** except showing anomalous temperature (colors, units: K) and salinity (contour, CI: 0.05 psu).

2.5 Summary

Questions regarding the ocean response to changes in atmospheric aerosol loading in general have arisen recent years (e.g. *Evan et al*., 2009; *Ottera, et al.,* 2010; *Booth et al.,* 2012; *Zhang et al.,* 2013). Here we exploit the availability of new simulations

produced as part of CMIP5 to revisit the ocean response to the five largest tropical volcanoes of the last 135 years (Krakatau, Santa Maria, Agung, El Chichón, and Pinatubo) in a set of 36 historical climate simulations produced using eight widely used climate models. Our goals are to clarify the common features of the oceanic response and those properties that vary among models and simulations.

The first part of this study examines the response of global average and hemispheric properties to volcanic aerosols. All models show an annual average reduction in net surface solar radiation of 1-5 W m^{-2}, a drop in net surface heat flux of 1-3 W m^{-2}, and a resulting decline in SST of 0.1-0.3 K. Sea ice extent and mass also increase by about 5%. For smaller eruptions SST may recover in a few years, but our results confirm the suggestion of previous studies [e.g., *Delworth et al*., 2005; *Gleckler et al*., 2006; *and Stenchikov et al*., 2009] that the impacts on ocean heat content of major eruptions may persist for decades. The increase in sea ice area and mass also persists well beyond the lifetime of stratospheric aerosols due to the reinforcing impact of solar albedo feedback and reductions in thermodynamic surface heat loss. The cool SST signal also penetrates into the subsurface ocean, lowering 0-1000m temperature by an average of roughly 0.03 K, and persisting for many decades, masking some of the anthropogenic warming signal. Indeed, comparisons of simulations with and without volcanic aerosols (available for CCSM4 and GFDL-CM3) show that the concentration of eruptions in the early years of the 20th century and again in the near the end of the century may mask some of the acceleration of ocean heating that might otherwise have been observed.

A number of previous studies have explored the connection between volcanic eruptions and interannual to decadal climate variability. However all have suffered from insufficient samples to make this discrimination (we estimate that approximately 100 ensemble members would be required to simply average out an incoherent ENSO signal). Using a Rotated Extended Empirical Orthogonal Function analysis to further discriminate the natural and forced response, we find there is no compelling evidence of a link between the timing of an eruption and a shift in phase of ENSO. We have made a similar effort to examine the relationship between the volcanic eruptions and the phase of NAO in boreal winter sea level pressure and found similarly tenuous connections.

Finally we examine the impact of eruptions on the overturning circulation, most particularly the overturning in the North Atlantic and confirm previous results suggesting that volcanic eruptions may enhance the overturning circulation (and consequently increase northward heat transport) due to increases in ocean surface density in the northern Atlantic sector. A comparison shows that the models vary by at least a factor of four in their sensitivity, the most sensitive models being those which have the most Atlantic meridional overturning variability in general.

The relationship between AMV and volcanic eruption is not discussed in the study. Whether there is a causative link between AMV and AMOC in CMIP5 models and the importance of AMV index on better understanding the volcanic cooling are interesting topics and require further studies.

Chapter 3: Seasonal and centennial trends in Arctic climate: information from CMIP5 simulations

3.1 Introduction

This study examines seasonal variability and centennial trends in the surface atmosphere, ocean, and sea ice, and their interactions in the Arctic as they appear in 14 CMIP5 (Coupled Model Intercomparison Project Phase 5) coupled models. Our interest in these models arises because historical observational data are limited, especially at the high latitudes. The coupled models are also interesting because they span a wide space of key parameters such as mean sea ice cover and mean SST. A number of previous studies have already explored trends in the sea ice cover in these models mainly in connection to the impact of rising greenhouse gasses [e.g. *Wang and Overland,* 2012; *Stroeve et al.,* 2012]. In contrast, much less attention has been paid to the response of high latitude surface fluxes and in the underlying ocean to the two main prescribed forcings: the seasonal cycle of sunlight and the radiative imbalance due to greenhouse gasses. This is surprising because of the potential relationship between the processes regulating the seasonal cycle and those controlling centennial trends [*Cavalieri et al*., 2003; *Moritz et al*., 2003].

The Arctic Basin consists of the Eurasian Basin and the American Basin. The marginal seas of the Arctic Basin incorporate the East Siberian Sea, the Laptev Sea and the Kara Sea at the Eurasian Basin, and the Beaufort Sea at the Canadian Basin. The Arctic Basin exchanges heat and mass with the Pacific and Atlantic Oceans through the Bering Strait and the Nordic Seas respectively. The Nordic Seas region

includes the Greenland Sea, the Iceland Sea, the Norwegian Sea and the Barents Sea. Warm and saline Atlantic water at the Nordic Seas region enters the Arctic through the Fram Strait and the Barents Sea Opening, while cold and fresh water exports from the Arctic through the Fram Strait. Another branch of the Arctic water goes into the North Atlantic Ocean through the Davis Strait.

Because the seasonal cycle in the Arctic is dominated by annual variations it will be convenient to define a winter season, December-March (DJFM), and a summer season, June-September (JJAS). The winter-time atmosphere overlying the high latitude ocean is characterized by a strong polar high pressure system (Polar high) and associated anti-cyclonic wind pattern. The Bering Sea and the Nordic Seas are characterized by low sea level pressure and intensified mid-latitude jet stream.

The seasonal variation of the Arctic surface net flux reaches 140 W m^{-2} [*Curry et al*., 1996]. Both the cloud fraction and sea ice are important to the Arctic radiation budget through their regulation of surface reflectivity. Generally, there are more clouds over the Arctic Ocean in summer; but there are still lots of uncertainties of the seasonal cycle of cloud [*Curry et al*., 1996]. The impact of clouds on the surface flux is hard to estimate because of the impact of underlying sea ice [*Curry et al*., 1992]. The surface reflectivity of sea ice is about 0.5 to 0.7, the second highest reflectivity on the Earth [*Markvart and CastaŁżer*; 2003]. In addition to its reflection of radiative flux, the melting and growth processes of sea ice in different seasons affect the turbulent fluxes over the Arctic Ocean on the order of ~ 40 W m^{-2} [*Serreze et al*., 2007b].

The high latitude ocean surface circulation consists of an anti-cyclonic Beaufort Gyre driven by the winds associated with the Polar high pressure system [*Proshutinsky and Johnson*, 1997]. The typical magnitude of the Beaufort Gyre current is on the order of 10^{-1} m/s [*Proshutinsky and Johnson*, 1997]. Another major current in the Arctic is the transpolar drift stream, which transports the Arctic water from the East Siberian Sea and the Laptev Sea toward the Fram Strait.

The main fresh water source for the Arctic includes river discharge, Pacific inflow through Bering Strait, and net precipitation [*Serreze et al*., 2006]. Freshwater accumulates in the upper layer (within 20m) of the Beaufort Gyre due to Ekman convergence and subsequent downwelling [*Proshutinsky and Johnson*, 1997; *Proshutinsky et al*., 2002; *Serreze et al*., 2006]. The Atlantic water could be found at the mid-depth or deeper, which is most significant at the Eurasian Basin [*Steele and Boyd*, 1998].

The Arctic Ocean gains heat mainly two ways: heat flux from atmosphere, and heat convergence from the Pacific and Atlantic Oceans. The Atlantic Ocean contributes most of the heat advection into the Arctic through the Nordic Seas. Warm and saline Atlantic water moves northward along the eastern coast of Norwegian Sea and enters the Arctic Ocean through the Fram Strait and across the Barents Sea Opening. The salt fluxes at these two straits are comparable; however, the heat transport through Fram Strait is significantly larger than the Barents Sea Opening [*Aksenov et al*., 2010]. In summer, there is more Pacific water entering the Arctic Ocean from the Bering Strait and less Arctic water outflow from Fram Strait [*Serreze*

et al., 2006]. On seasonal time scales, surface atmospheric flux is the primary driver of the heat storage variations in the Arctic Ocean [*Serreze et al*., 2007b].

In addition to a prominent seasonal cycle the Arctic is remarkable in having a pronounced centennial warming trend in the atmosphere, ocean, and ice cover which seems inescapably linked to greenhouse forcing [*Moritz et al*., 2003; *Overland et al*., 2004]. For instance the warming trend in surface air temperature in the eastern Arctic Ocean is as much as 2°C per decade [*Chapman and Walsh*, 1993; *Rigor et al*., 2000]. The warming trend in atmosphere is related to both increasing heat fluxes and the atmospheric circulation in Arctic [*Rigor et al*., 2000; *Overland et al*., 2004]. Corresponding to the increasing surface air temperature, the strength of Polar high pressure has decreased in recent decades [*Walsh et al*., 1996].

Both the Arctic ice extent and thickness show remarkable decreases in recent decades [*Holloway and Sou*, 2002; *Cavalieri et al*., 2003]. The decreasing trend of sea ice extent is found in all seasons and it is greater in summer than in winter [*Cavalieri et al*., 2003]. The reduction of sea ice extent is most significant on the Russian side of the Arctic Basin [*Serreze et al.*, 2007a]. The melting of Arctic sea ice affects the heat and freshwater budgets. The sea ice decline affects the Arctic heat budget through the impact of ice on the radiative properties of the surface (the ice-albedo feedback). The decrease of sea ice reduces the surface albedo by exposing more sea water, which enhances ocean warming and causes more severe sea ice melting as a result [*Curry and Schramm*, 1995; *Graversen and Wang*, 2009; *Steele et al.*, 2010]. Melting sea ice also freshens the Arctic surface [*Aagaard and Carmack*, 1989; *Serreze et al.*, 2007].

The changes of ocean water in the Arctic can be found in both temperature and salinity. Temperature increases are as large as 1°C for Atlantic water in the Arctic Basin [*Carmack et al*., 1995; *Grotefendt et al*., 1998]. Changes of the annual mean temperature of the Nordic Seas is more remarkable with increase as much as 10°C from 1948 to 2005 [*Drange et al.*, 2005].

Salinity changes are different in different regions. The surface salinity at the Eurasian basin, which is near the Russian side of the Arctic, increases in recent decades, which is closely related with the associated surface pressure and wind pattern changes [*Steele and Boyd*, 1998; *Johnson and Polyakov*, 2001]. For the Beaufort Gyre, sea ice cover becomes thinner, and the upper ocean becomes less saline, which is due to the combined impacts of sea ice melting, atmospheric circulation and momentum transfer to ocean [*McPhee et al*., 1998; *Giles et al*., 2012]. The increasing rate of fresh water accumulation rate in the Beaufort Gyre is a result of the spin-up of the gyre, which could be explained by the increasing efficiency of momentum transfer into the upper ocean because of the decline of sea ice [*Giles et al*., 2012; *Davis et al.*, 2014].

In this study, I explore 14 CMIP5 coupled climate models, each with multiple ensembles. By averaging these we are able to minimize the impact of internal variability. Section 2 briefly describes the fourteen CMIP5 models, several observational data sets and the methods I used in this study. Section 3 presents the mean state and seasonal cycle of the Arctic atmosphere, ocean and sea ice, and discusses the interactions between these three and the centennial trends in CMIP5 historical simulations. Conclusions are presented in Section 4.

3.2 Data and method

3.2.1 CMIP5 model description

The historical simulations of fourteen multi-ensemble CMIP5 models are analyzed in this study (**Table 3.1**). All the data are of monthly resolution, and most data were obtained from the online archive (http://pcmdi3.llnl.gov/esgcet/home.htm), while for some ensembles of two GFDL-ESM models, data was obtained directly from Geophysical Fluid Dynamics Laboratory model working group. Ocean and sea ice model outputs in ten models are on original irregular grids. Horizontal and vertical resolutions are shown in **Table 3.1**. Most models have approximately 1°×1° spatial ocean resolution except for IPSL-CM5A-MR, whose horizontal resolution is about 2°×2°. NorESM1-M has the finest vertical resolution (70 layers), and HadCM3 have the coarsest resolution, which is about 20 layers. In order to carry out spatial comparison among models, sea water temperature and salinity data are remapped to 1°×1° resolution using climate data operators (CDO).

3.2.2 Methods

The calculation of volume transports into Arctic is applied on the original ocean grid to avoid possible biases from remapping. I calculate volume flux at six straits: the Bering Strait (~65°N), the Davis Strait (~67°N), the Fram Strait (~79°N), the Barents Sea Opening (~20°E), the Denmark Strait (~65°N), and the strait between Iceland and Norway (~65°N). The exact latitude and longitude vary among models due to the different grid types. For HadCM3, in which ocean model there is a "rigid-lid" parameterization, the volume flux through certain strait is calculated as

Table 3.1: Some basic information about historical simulations examined in this study: name, institution, ocean model resolution (longitude × latitude ×vertical), and the number of all ensemble members and those with available daily geopotential height data.

Model Name	**Model Center**	**Ocean resolution**	**Grid**	**Ensembles**
CanESM2	Canadian Centre for Climate Modelling and Analysis	1.4ºx0.9ºx40*lev*	regular	5/5
CCSM4	National Center for Atmospheric Research	1.1ºx(0.27º-0.54º)x60*lev*	displaced	6/1
CNRM-CM5	CNRM, France	1ºx(1/3º-1º)x42*lev*	tripolar	10/1
GFDL-CM3	Geophysical Fluid Dynamics Laboratory	1ºx(1/3º-1º)x50*lev*	tripolar	5/5
GFDL-ESM2G	Geophysical Fluid Dynamics Laboratory	1ºx(1/3º-1º)x50*lev*	tripolar	2/1
GFDL-ESM2M	Geophysical Fluid Dynamics Laboratory	1ºx(1/3º-1º)x50*lev*	tripolar	3/1
GISS-E2-R	NASA Goddard Institute for Space Studies	1ºx~1ºx32*lev*	regular	6/0
HadCM3	Met Office Hadley Centre, U.K.	1.25ºx1.25ºx20*lev*	regular	10/10
HadGEM2-ES	Met Office Hadley Centre, U.K.	1ºx(1/3º-1º)x40*lev*	regular	4/1
IPSL-CM5A-MR	Institut Pierre-Simon Laplace, France	2ºx2ºx39*lev*	tripolar	3/3
MIROC5	Model for Interdisciplinary Research On Climate, Japan	1ºx1ºx50*lev*	tripolar	5/5
MPI-ESM-LR	Max Planck Institute for Meteorology, Germany	1.5ºx1.5ºx40*lev*	displaced	3/3
MRI-CGCM3	Meteorological Research Institute, Japan	1ºx0.5ºx50*lev*	tripolar	3/1
NorESM1-M	Norwegian Climate Centre	1ºx1ºx70*lev*	displaced	3/3

$\iint v(x,z)dxdz$, where $v(x,z)$ is the monthly mean ocean velocity normal to sides of the volume, x is the along-side distance coordinate, and z is the vertical coordinate. For the rest "free surface" models, the volume transport is calculated from mass

transport data. There is no available mass transport data for MIROC5, and thus the calculation of volume and heat transports is not applied in this model.

Heat transport in HadCM3 is calculated as $\iint \rho C_p v'(x,z)\theta' dxdz$, where ρ is the density of sea water, C_p is the heat capacity of sea water, and θ' is the monthly mean potential temperature (θ) anomaly $\theta' = \theta - \theta_{ref}$. θ_{ref} is the reference potential temperature, and 273.15 K is selected as θ_{ref} in our study. ρ and C_p are assumed to be constant. For models with mass transport data available, heat transport is calculated as $\iint C_p m'(x,z)\theta' dxdz$, where $m(x,z)$ is the mass transport.

In this study, the heat content of mix-layer sea water is calculated as $\rho C_p \int_{70m}^{0} T dz$, where ρ and C_p are assumed to be constant. In addition, we examine the heat content changes corresponding to sea ice melting in recent 145 years. The definition of total heat content change ΔHC follows *Boé et al*. [2009], which is expressed as a change of temperature within the mixed layer: $\Delta HC = \frac{\rho_w C_p \Delta T_o V + \rho_i L_i \Delta V_i}{\rho_w C_p \mathrm{V}}$, where ρ_w and ρ_i are the density of sea water and sea ice respectively, ΔT_o is the mean temperature change of sea water, V is the volume of mixed layer, L_i is the latent heat of melting sea ice, and ΔV_i is the volume change because of sea ice melting. ΔT_o and ΔV_i are calculated as the mean number from 1986 to 2005 minus the mean number from 1861 to 1880.

I selected four regions to analyze the temperature and salinity profiles: Atlantic Water Zone (AWZ) in the Nordic Seas, the northern Barents Sea, the Laptev Sea and the Beaufort Sea. Definition of AWZ in the Nordic Seas follows the salinity definition in *carton et al.* [2011]. The approximate latitude and longitude for AWZ

are 65-80°N, 15°W-30°E. Temperature and salinity at AWZ in the Nordic Seas help to identify the Atlantic water layer at other three regions. Coordinates for the northern Barents Sea are 75°N to 80°N, 30°E to 60°E. The Laptev Sea and the Beaufort Sea are two regions near the Pacific Ocean with latitude ranging from 75-80°N, and longitudes are 120-150°E and 120-150°W respectively.

3.2.3 Observational data description

Several observational data sets are used in this study to examine the performance of CMIP5 historical simulations on the mean state and seasonal cycle of the Arctic. Simulations of sea level pressure are compared to the monthly mean HadSLP2 (Hadley Centre Sea Level Pressure data, version 2) observational data with time coverage from 1860 to 2004 [*Allan and Ansell*, 2006]. The spatial resolution for HadSLP2 is 5°x5°. Surface radiative and turbulent fluxes from ERA-40 reanalysis product at European Centre for Medium-Range Weather Forecasts (ECMWF) are analyzed in this study as well. The ERA-40 provides surface flux data from September 1957 to August 2002, and the spatial resolution is 2.5°x2.5° [*Uppala et al.,* 2005]. The temperature and salinity field in model simulations are compared to the Polar science center Hydrographic Climatology third version data (PHC3.0) [*Steele et al*., 2001] and the Simple Ocean Data Assimilation (SODA) version 2.2.4 reanalysis estimates of *Carton and Giese* [2008]. PHC3.0 only provides the climatology data from 1900 to 1994, while the time coverage for SODA is longer, from 1871 to 2010. Observational sea ice extent data are obtained from the National Snow and Ice Data Center (NSIDC), which is a merged data version of multiple observational sources with time coverage from 1972 to 2002 [*Cavalieri et al*., 2003].

3.3 Mean state and seasonal cycle of the Arctic

In this section I first examine the time mean seasonal cycle, and then look at the centennial trend of the Arctic atmosphere, ocean and sea ice in 14 CMIP5 coupled models. Interactions between the atmosphere, ocean and sea ice are also discussed.

3.3.1 Basic character of the atmosphere

At the beginning, I compared the simulated winter-time (DJFM) sea level pressure to the HadSLP2 observational data (**Figure 3.1**). All models capture the Polar high pressure system across the Beaufort Sea and the Laptev Sea, and the low pressure at the northern Atlantic and Pacific Oceans. However, the strength of Polar high varies among models. CCSM4 presents the largest biases with a mean sea level pressure ~15 mb lower than that in HadSLP2. In MIROC5, the mean pressure at the high latitude ocean is ~ 6 mb higher than HadSLP2. The annual mean sea level pressure at the Beaufort Sea in HadGEM2-ES is ~ 10.20 mb, which is closest to HadSLP2 observation ~10.17 mb.

The CMIP5 models capture the basic seasonal cycle of surface radiative and turbulent fluxes in the ERA-40 reanalysis (**Figure 3.2**). Ocean gains heat through the solar radiation and loses heat through the longwave, latent heat and sensible heat fluxes. The seasonal cycle of surface net flux is controlled by the shortwave flux. Among the 14 models, GISS-E2-R shows the strongest seasonal cycle of shortwave flux, which reaches ~230 W m^{-2}. The spatial pattern of winter-time surface flux over the high latitude ocean in CMIP5 simulations is similar to the ERA-40 with strong heat loss from the northern Atlantic and Pacific Oceans, and relatively weaker heat loss from the Arctic Basin. Models with extreme low pressure at the northern

Atlantic and Pacific Oceans also present intense heat loss at these regions, like CCSM4.

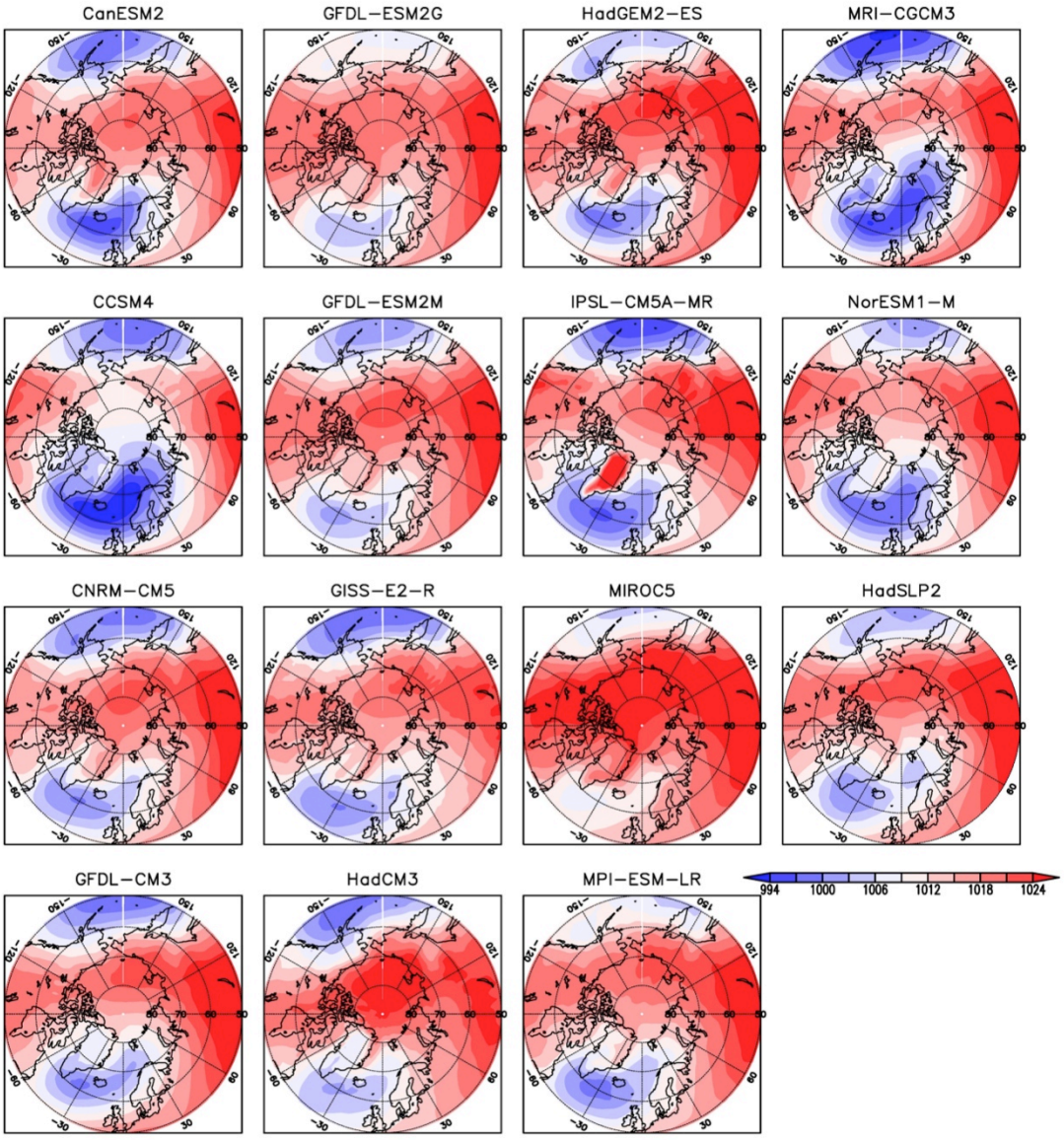

Figure 3.1: Time mean of ensemble mean of winter-time (DJFM) sea level pressure from 1861 to 2004 at high latitudes for 14 CMIP5 models and HadSLP2 observational data. Units are mb.

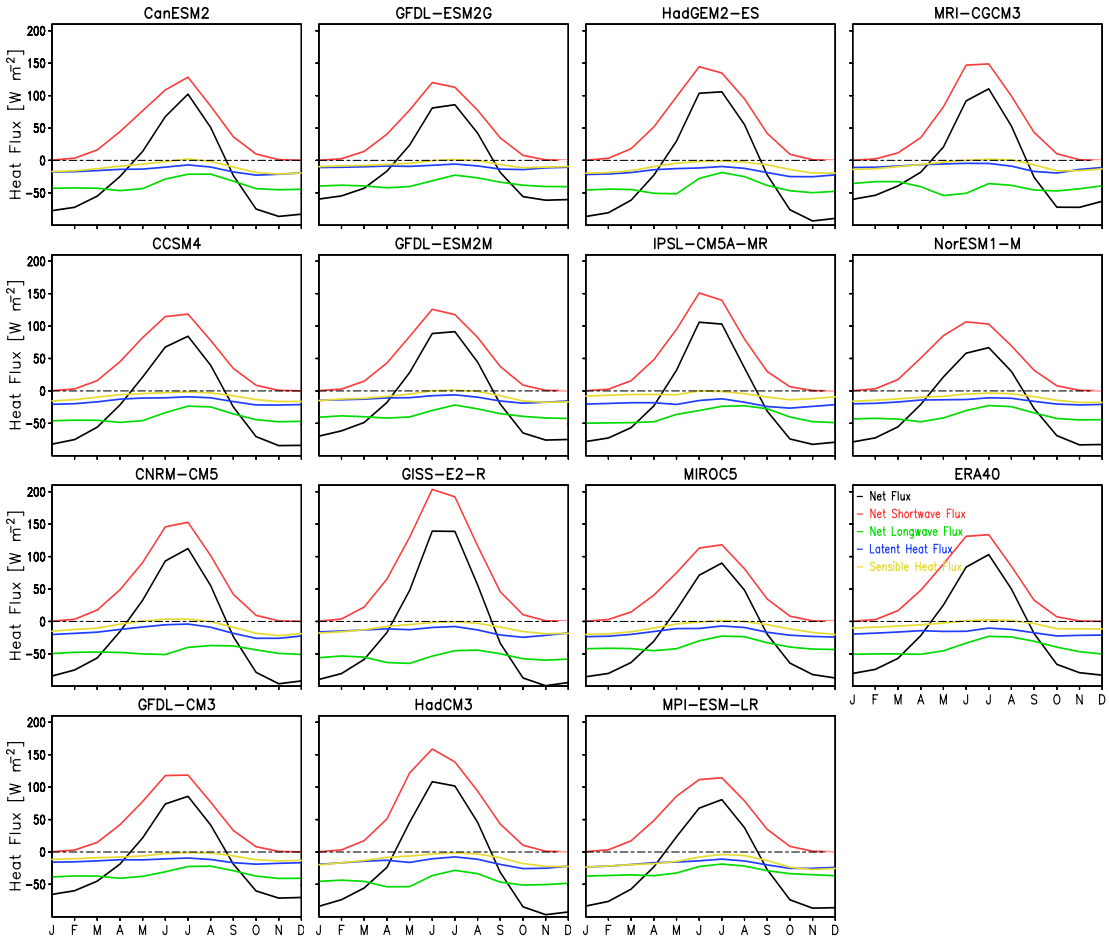

Figure 3.2: Seasonal cycle of ensemble mean surface downward net flux (black), net shortwave flux (red), net longwave flux (green), latent heat flux (blue) and sensible heat flux (yellow) from 1957 to 2002 over the high latitude ocean (north to 65°N) for 14 CMIP5 models and ERA-40 reanalysis data.

3.3.2 Sea ice property and its impact on the albedo

The Arctic sea ice to the north of 65°N shows less variations than that at lower latitudes (**Figure 3.3**). Most of the sea ice to the south of 65°N are typical seasonal sea ice, which melts completely at summer. The sea ice concentration at the Nordic Seas also presents lots of biases among models. For example, sea ice almost covers

about half of the Nordic Seas and blocks the Barents Sea Opening in GISS-E2-R. In the other models, the eastern part of Nordic Seas is ice-free at least in summer. The

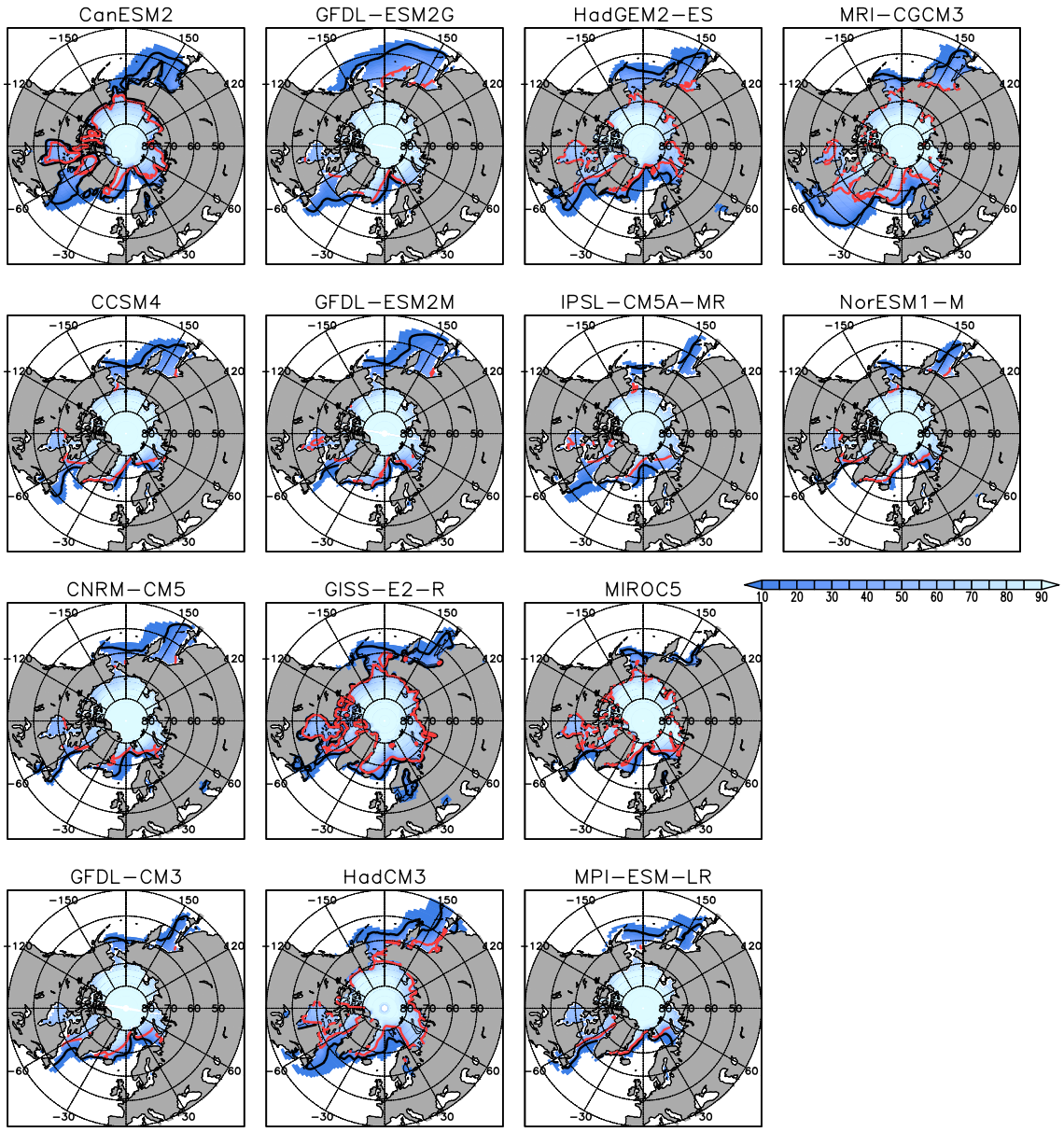

Figure 3.3: Time mean sea ice concentration (%) (color shading), winter-time (DJFM) sea ice extent (black contour), and summer-time (JJAS) sea ice extent (red contour) from 1861 to 2005 for 14 CMIP5 models.

summer-time sea ice extent shrinks to the interior of the Arctic Basin in six models, like CanESM2 and GISS-E2-R. The seasonal variation of the sea ice extent in GISS-

E2-R is strongest among these models and is also stronger than the NSIDC observations (**Figure 3.4**). In addition, total cloud fraction over the high latitude ocean also decreases in summer in this model, which allows more solar radiation reaching the surface. The failure in simulating the summer-time cloud fraction also exists in other four models: CNRM-CM5, GFDL-CM3 and two GFDL ESM models. Rest of models like CCSM4 show more clouds in summer like the observations suggest.

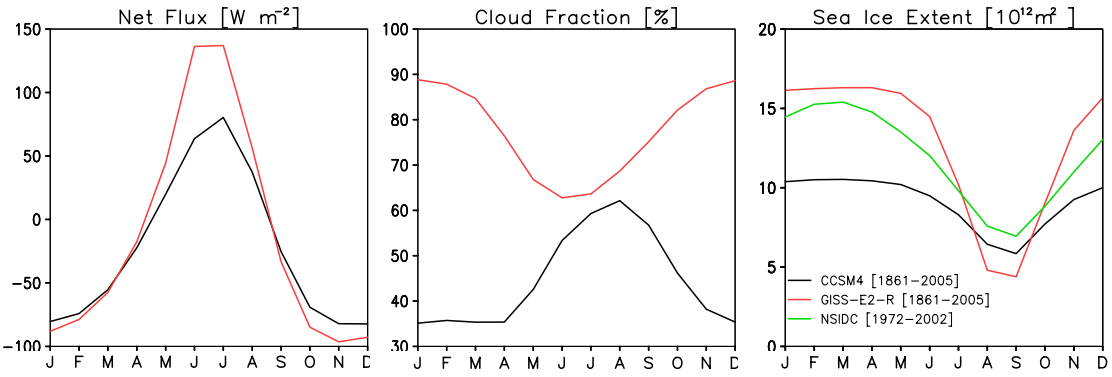

Figure 3.4: Seasonal cycle of ensemble mean surface net flux, cloud fraction, and sea ice extent at the high latitude ocean (north to 65°N) for GFDL-ESM2G, GISS-E2-R and NSIDC observational data.

3.3.3 Mean state of the Arctic Ocean

Next I look at the mean state of the Arctic ocean. Warm water mainly concentrates at the Nordic Seas like the PHC3.0 observational data show (**Figure 3.5**). Sea water temperature to the south of Iceland is higher than PHC3.0 in six models like CCSM4, while the temperature of Atlantic water in the Nordic Seas is either similar to or lower than the PHC3.0. Region with cold water (< 0°C) is similar to the region covered with sea ice. For example, in GISS-E2-R where sea ice covers half of the Nordic Seas, warm water could only be found at the coastal area of

Norwegian Sea. In comparison, warm water in CCSM4 takes a much larger area, which is roughly same as the ice-free region.

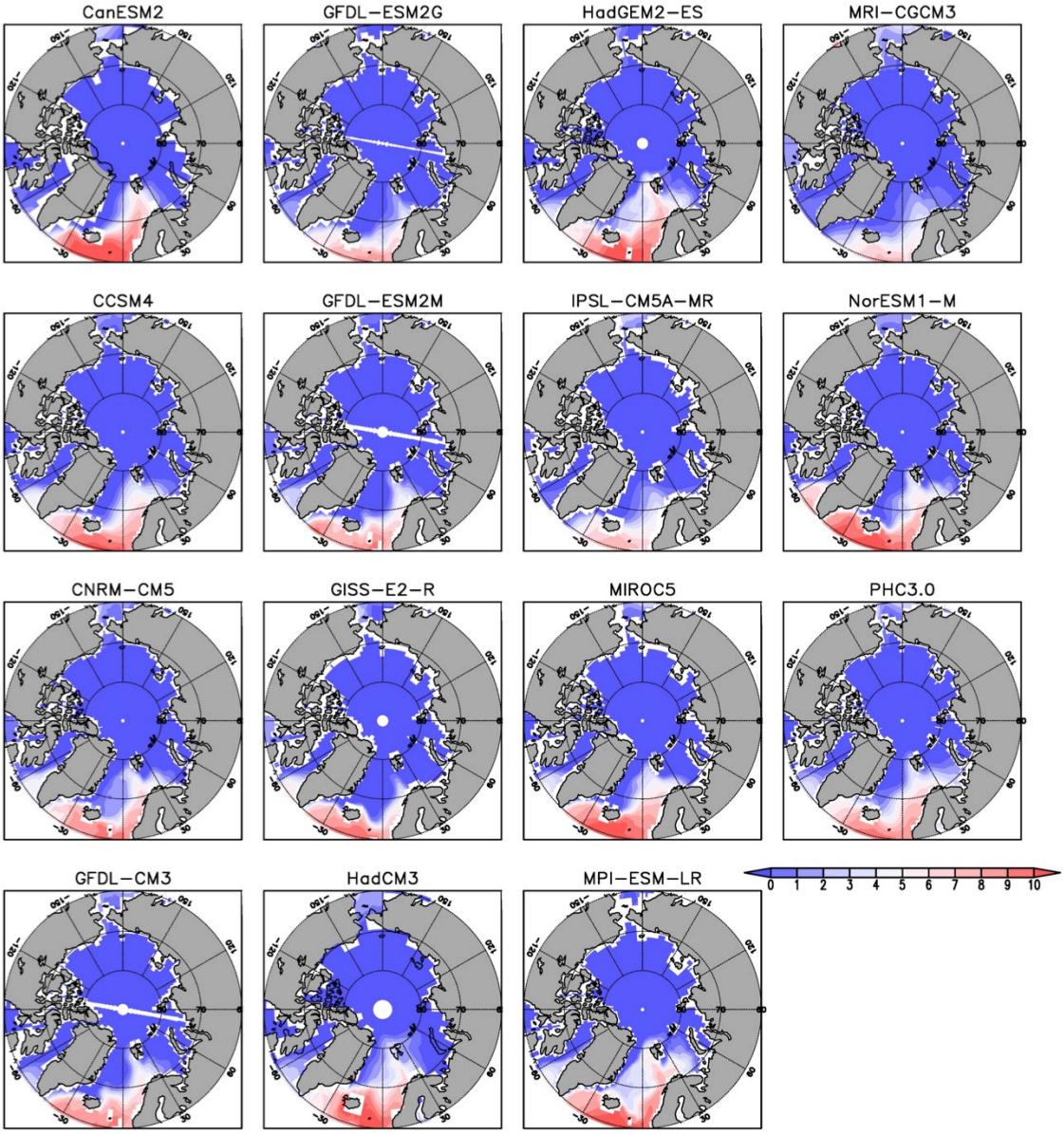

Figure 3.5: Time mean of ensemble mean upper ocean temperature (0-100m) from 1900 to 1994 for 14 CMIP5 models and PHC3.0 observational data. Units are °C.

Simulated sea water salinity at the Nordic Seas region is similar to that in the SODA reanalysis data, while the largest biases of salinity distribution happen at the

Arctic Basin (**Figure 3.6**). In SODA, fresh water is mainly concentrated at the Laptev Sea and the Beaufort Gyre. In GISS-E2-R, HadGEM2-ES, IPSL-CM5A-MR, and MRI-CGCM3, relatively fresher water is also found at these two locations. The spatial distribution of salinity in HadCM3 and CCSM4 presents the two extremes among models. In HadCM3, fresh water is concentrated in the Beaufort Gyre and

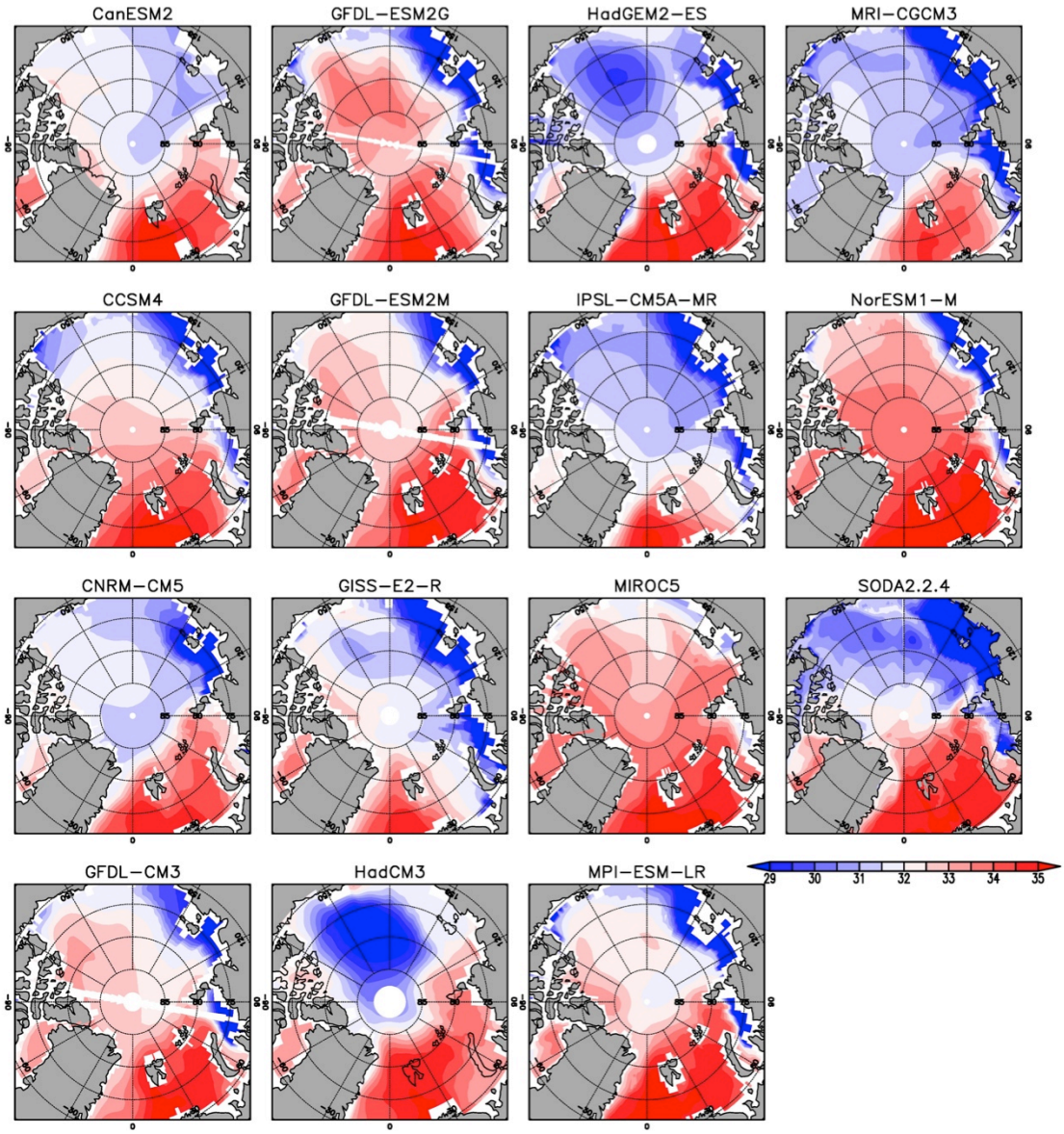

Figure 3.6: Time mean of ensemble mean upper ocean salinity (0-100m average) for 14 CMIP5 models and SODA reanalysis data. Time mean is calculated from 1861 to 2005 for models and from 1871 to 2005 for SODA. Units are psu.

saltier water is found in the marginal seas (the Beaufort Sea and the Laptev Sea). But in CCSM4, there is lower salinity in the marginal seas and high salinity in the Beaufort Gyre. For the rest models, there is fresh water along the Russian coast and saltier water in the rest regions.

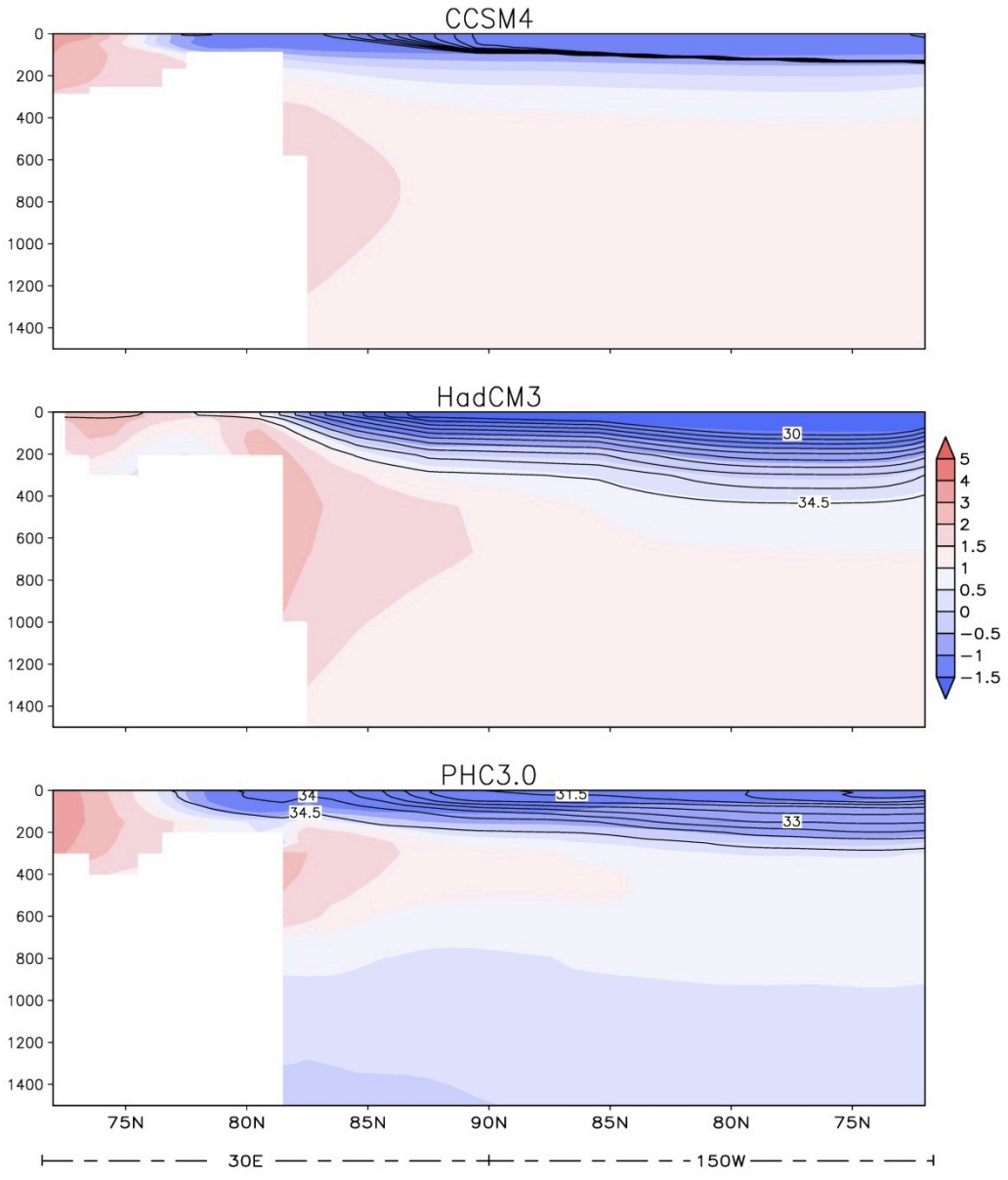

Figure 3.7: Ensemble mean temperature and salinity profiles for one across-Arctic sector (30E and 150W) for CCSM4, HadCM3 and PHC3.0 from 1900 to 1994. Units for temperature are °C, and units for salinity are psu.

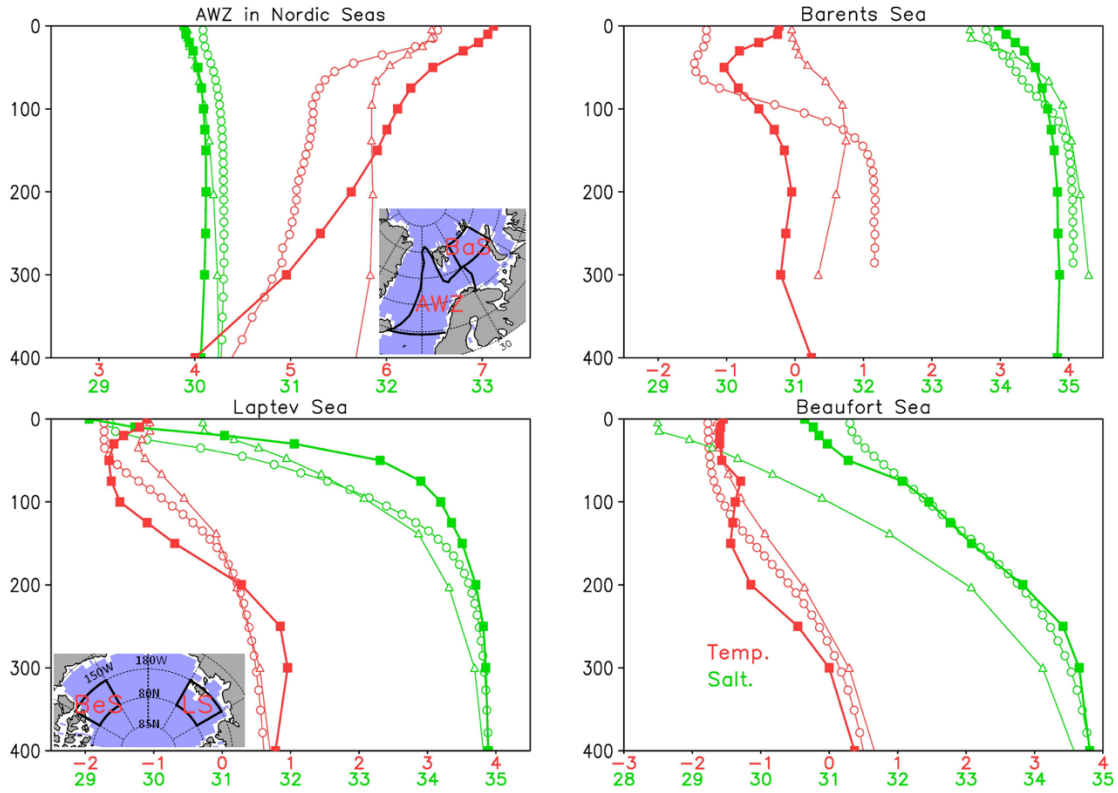

Figure 3.8: Ensemble mean temperature and salinity profiles in the defined four regions for CCSM4 (open circle), HadCM3 (triangle) and PHC3.0 (closed square) for time period 1900-1994. Locations of selected regions are marked in the two spatial maps on the left panel. AWZ means the Atlantic water zone in the Nordic Seas, and BaS stands for the Barents Sea. LS is short for the Laptev Sea, and BeS is for the Beaufort Sea. Units for temperature are °C, and units for salinity are psu.

Compared to the PHC3.0, most models fail to present the warm Atlantic water layer at 200 to 800 m deep (**Figure 3.7**). In CMIP5 simulations, the Atlantic water extends from 200 m to deep ocean (>1500 m). The upper layer (0-100m) salinity in the Beaufort Sea is larger in CCSM4 than in observations and smaller in HadCM3 (**Figure 3.8**). The surface salinity in the Laptev Sea is similar to PHC3.0 in CCSM4 but it is much larger in HadCM3. In the deeper ocean, salinity is underestimated in both of the two models. The magnitude of vertical temperature in these two models is

similar to PHC3.0, but the profile is less stratified. At the Nordic Seas, the vertical temperature at depth ranging from 100 to 300 m is less stratified than the PHC3.0 observation. At the northern Barents Sea, most models present the existence of Atlantic water at depth ranging from 100 to 200 m. Generally, simulated temperature in the mix layer (0-70 m) is less stratified in this region. In comparison, the salinity profiles at the Nordic Seas and the Barents Sea are similar to the observation.

The difference in the salinity distribution in CCSM4 and HadCM3 could be explained by the strength of the Beaufort Gyre shown in **Figure 3.9**. The Beaufort Gyre is much more robust in HadCM3 than the rest models and the observations with the magnitude of ocean currents reaching ~1 m/s. In HadCM3, the Pacific water moves westwards after entering Arctic, and after that the intense Beaufort Gyre brings the fresh Pacific water to its center through Ekman pumping. For CCSM4, the Pacific water splits into two branches, which move westwards and eastward separately along the coasts. Due to the weak Beaufort Gyre, fresh Pacific water stays at the coast area instead of moving into the interior of the Arctic Basin. In models with similar strength of Polar high to observation, like HadGEM2-ES, the Beaufort Gyre is not strong enough to bring all fresh water into the interior of the Arctic Basin, which makes the upper layer salinity of the Laptev Sea relatively small. For the rest models, fresh water stays at the coastal regions due to the weak Beaufort Gyre.

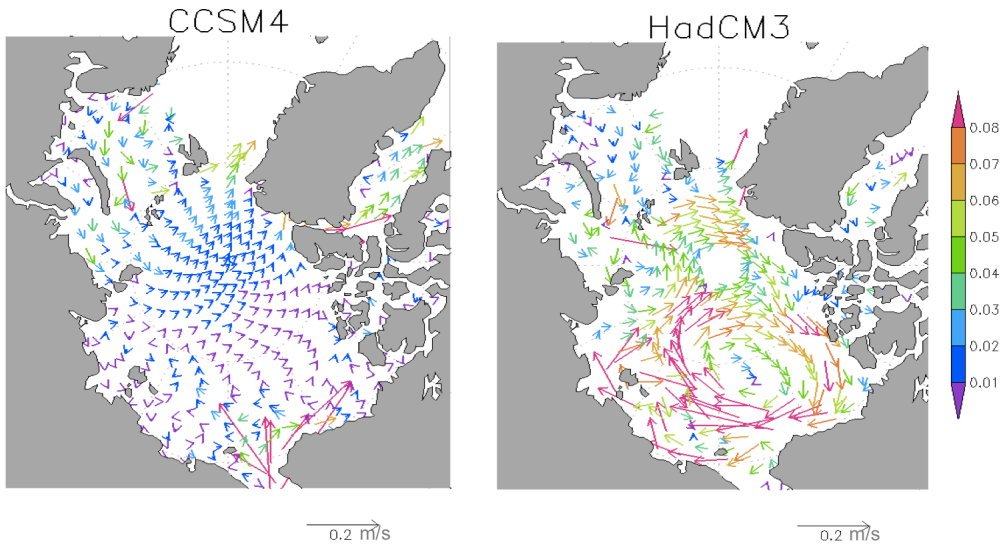

Figure 3.9: Time mean of ensemble mean surface velocity from 1861 to 2005 at Arctic Basin in CCSM4 and HadCM3.

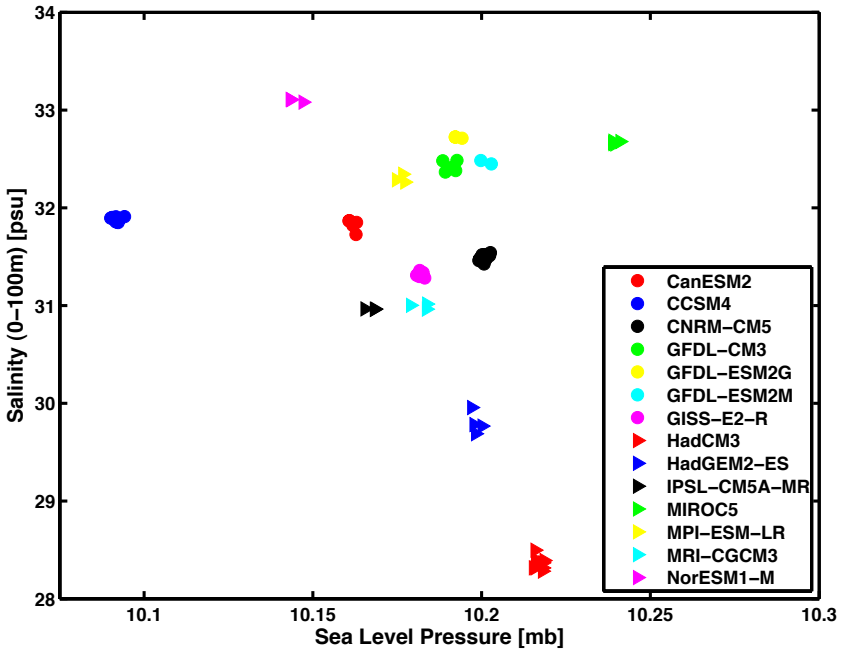

Figure 3.10: Correlation between the ensemble mean sea level pressure and upper ocean salinity (0-100m) at Beaufort Gyre (75-80°N, 150-180°W) from 1861 to 2005.

The strength of the Beaufort Gyre is closely correlated with that of the Polar high. Excluding CCSM4 and MIROC5, in which the mean sea level pressure is either too

high or too low compared to observations, the upper layer salinity at the Beaufort Gyre decreases with increasing local sea level pressure (**Figure 3.10**). Sea level pressure at the Beaufort Gyre is closest to the HadSLP2 observation in HadGEM2-ES, and as a result, HadGEM2-ES also gives the best presentation of upper ocean salinity.

Table 3.2: Volume transport through the Bering Strait, the Davis Strait, the Fram Strait and the Barents Sea Opening. Units are Sv.

Models	**Bering Strait**	**Davis Strait**	**Fram Strait**	**Barents Sea Opening**	**Net**
CanESM2	0.96	0	-3.12	2.16	0
CCSM4	1.05	-1.73	-1.51	2.19	0
CNRM-CM5	1.44	-2.31	-1.53	2.22	-0.18
GFDL-CM3	1.01	-0.67	-2.32	1.85	-0.13
GFDL-ESM2M	0.92	-0.34	-2.83	2.09	-0.16
GFDL-ESM2G	0.90	-1.08	-0.92	1.02	-0.08
GISS-E2-R	0.15	-0.18	-0.31	0.29	-0.05
HadCM3	0	0	-1.2	1.2	0
HadGEM2-ES	0.66	-0.68	-2.53	2.45	-0.09
IPSL-CM5A-MR	1.28	-0.5	-1.30	0.36	-0.16
MPI-ESM-LR	0.70	-1.22	-2.55	2.98	-0.08
MRI-CGCM3	1.02	-1.02	-2.60	2.42	-0.17
NorESM1-M	1.56	-1.99	-1.76	2.19	0
Tsubouchi et al. 2012	1.0±0.2	-3.1±0.7	-1.6±3.9	3.6±1.1	-0.19±4.13

There are Pacific water inflows at the Bering Strait, Atlantic water inflows at the Barents Sea Opening, and net outflows at the Davis Strait and the Fram Strait in all

models, although in CanESM2 and HadCM3, the Davis Strait is almost closed. The magnitude of the volume transports at these four straits varies among model (**Table 3.2**).

Table 3.3: Heat transport through the Bering Strait, the Davis Strait, the Fram Strait and the Barents Sea Opening. Units are TW (10^{12} W).

Models	**Bering Strait**	**Davis Strait**	**Fram Strait**	**Barents Sea Opening**	**Net**
CanESM2	2.30	2.08	9.81	51.98	66.17
CCSM4	0.03	12.91	10.18	5.67	28.79
CNRM-CM5	6.95	8.51	10.26	4.09	29.81
GFDL-CM3	5.53	7.94	29.14	49.49	92.10
GFDL-ESM2G	0.21	6.78	17.98	29.40	54.36
GISS-E2-R	0.29	2.23	6.32	5.40	14.24
HadCM3	4.11	4.40	52.40	31.42	92.32
HadGEM2-ES	2.20	4.64	33.42	64.21	104.47
IPSL-CM5A-MR	3.82	3.72	15.10	-0.92	21.72
MPI-ESM-LR	1.02	13.02	27.72	18.30	60.06
MRI-CGCM3	4.16	2.92	9.79	49.01	65.89
NorESM1-M	2.09	15.82	40.06	2.85	60.82

The volume transports at the Fram Strait and the Barents Sea Opening is weakest in GISS-E2-R. The high sea ice concentration at the Nordic Seas might be one explanation for that, which reduces the momentum flux transfer rate from atmosphere to ocean. In summer, there are more Pacific water inflow but less Atlantic water inflow as the observational studies show. The net volume transport into the Arctic Basin shows no seasonal difference in all models except HadGEM2-ES and MRI-CGCM3. On seasonal time scale, the volume transports at the Fram Strait and the

Barents Sea Opening are generally in phase in models excluding HadGEM2-ES and MRI-CGCM3. When more water goes into the Arctic through the Barents Sea Opening it comes out through Fram Strait. Relationship between the volume transport at the Denmark Strait and that at the Iceland-Norway Strait (not shown here) is similar to that at the Fram Strait and the Barents Sea Opening.

Table 3.4: Salt transport through the Bering Strait, the Davis Strait, the Fram Strait and the Barents Sea Opening. Units are 10^6 Kg s^{-1}.

Models	**Bering Strait**	**Davis Strait**	**Fram Strait**	**Barents Sea Opening**	**Net**
CanESM2	31.77	0.05	-106.81	77.90	2.90
CCSM4	34.40	-58.12	-52.45	77.58	1.41
CNRM-CM5	46.37	-77.11	-51.35	78.11	-3.99
GFDL-CM3	33.26	-22.04	-78.25	66.40	-0.63
GFDL-ESM2G	29.42	-39.17	-29.12	36.44	-2.43
GISS-E2-R	4.87	-6.11	-9.32	10.68	0.11
HadCM3	-0.49	-0.08	-39.31	43.35	3.47
HadGEM2-ES	21.93	-21.59	-87.03	87.40	0.70
IPSL-CM5A-MR	41.79	-16.42	-40.86	13.02	-2.47
MPI-ESM-LR	22.96	-40.73	-88.31	105.77	-0.31
MRI-CGCM3	33.20	-33.01	-85.60	84.94	-0.48
NorESM1-M	52.41	-68.59	-61.20	78.85	1.46

Generally, heat transports into the Arctic Ocean through the Fram Strait and the Barents Sea Opening are larger than those through the Bering Strait and the Davis Strait (**Table 3.3**). There are huge variations in heat transport through the Barents Sea Opening among models, which is mainly due to different locations where the calculation of volume flux is applied. In models where the calculation is applied at

the ice-covered region, the number of heat transport is smaller than those at the ice-free region. Like the net volume transport, the heat transport into the Arctic Ocean through Nordic Seas is most significant in winter. The ensemble mean salinity flux at the four straits are listed in **Table 3.4**. The seasonal cycle of salinity flux well represents the seasonal cycle of volume flux.

3.4 Centennial trend of the Arctic Ocean

3.4.1 Seasonal variations of atmospheric flux trend

Next I turn attention to the centennial trends in the Arctic Ocean. Results indicate that during the past one and half century, surface net flux increases (ocean gains heat) in all models (**Figure 3.11**).

There is an apparent seasonal difference of the heat flux increase in eight models, like CCSM4 and GISS-E2-R, and no seasonal difference found in the rest six models, like GFDL-ESM2G and NorESM1-M. In models showing significant seasonal differences in net flux increase, ocean gains more heat in summer due to more incoming solar radiation but also loses more heat in winter which is mainly because of the latent and sensible heat loss. We notice that models with increasing upward longwave, latent and sensible heat fluxes in winter are those showing significant decreases in the winter-time sea ice extent (**Figure 3.12**). For models with weaker seasonal latent heat changes, like GFDL-ESM2G, sea ice extent shows very few reductions or even shows small amount of increase in winter. This indicates that the ocean losses heat in winter through longwave radiation and turbulent heat fluxes.

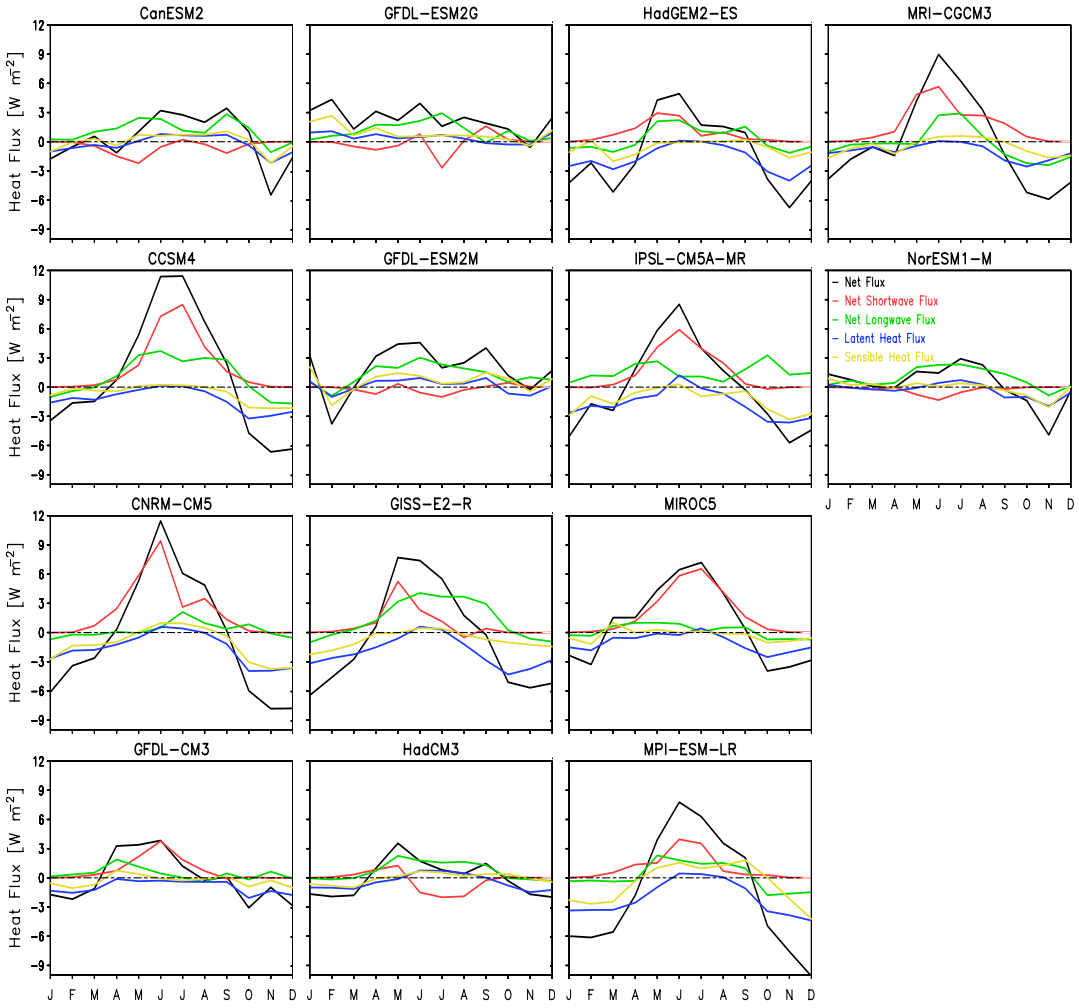

Figure 3.11: The long-term trend of ensemble mean surface downward net flux (black), net shortwave flux (red), net longwave flux (green), latent heat flux (blue) and sensible heat flux (yellow) at high latitudes for 14 CMIP5 models. The long-term trend here is defined as the difference between the mean value from 1861 to 1880 minus the mean from 1986 to 2005.

On the other hand, the sea ice cover retreat in summer enhances the surface solar flux heating. Models with significant sea ice losses are those with remarkable surface net flux increases, like CCSM4 and CNRM-CM5, indicating the importance of ice-albedo feedback process at the Arctic Ocean. Despite of the more severe sea ice loss in recent 50 years, the sensitivity of turbulent and longwave fluxes to ice cover is similar to that from 1861 to 2005.

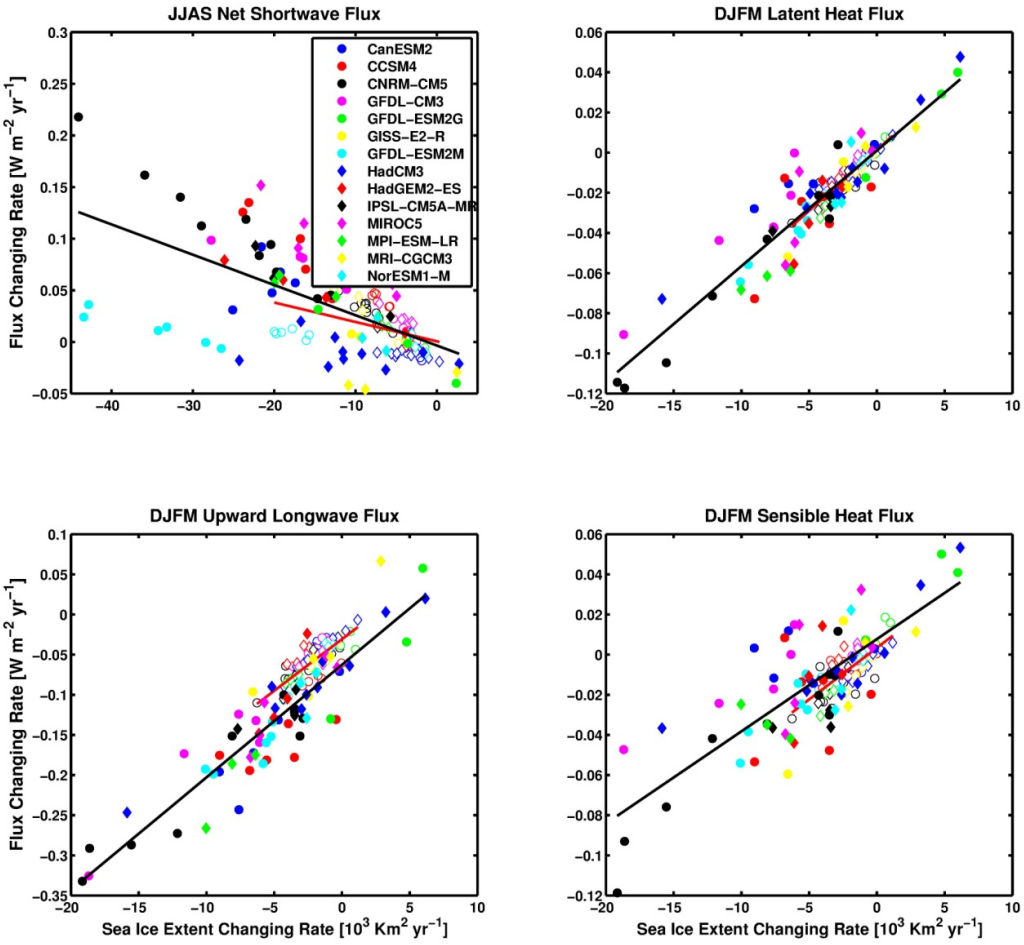

Figure 3.12: Seasonal feedbacks: rate of change of heat flux versus rate of change of sea ice extent for various flux components. Open marks are calculated from 1861 to 2005; closed marks are calculated from 1950 to 2005.

3.4.2 Warming of the Arctic Ocean

Warming of sea water mainly happens in the Nordic Seas and the Barents Sea (**Figure 3.13**). This warming trend could be found in all models, and is most significant in CCSM4, GISS-E2-R, HadGEM2-ES, IPSL-CM5A-MR and MPI-ESM-LR with temperature increasing as large as 1 °C from surface to 400m deep. The warming of the Barents Sea is closely correlated with the temperature change in the Nordic Seas. In comparison, the salinity shows very few changes in these two

regions. In the Laptev Sea and the Beaufort Sea, sea water warming is limited while salinity changes are significant. Upper layer water becomes fresher in CCSM4. In HadCM3, salinity increases in the Laptev Sea and decreases in the Beaufort Sea, which is close to observation.

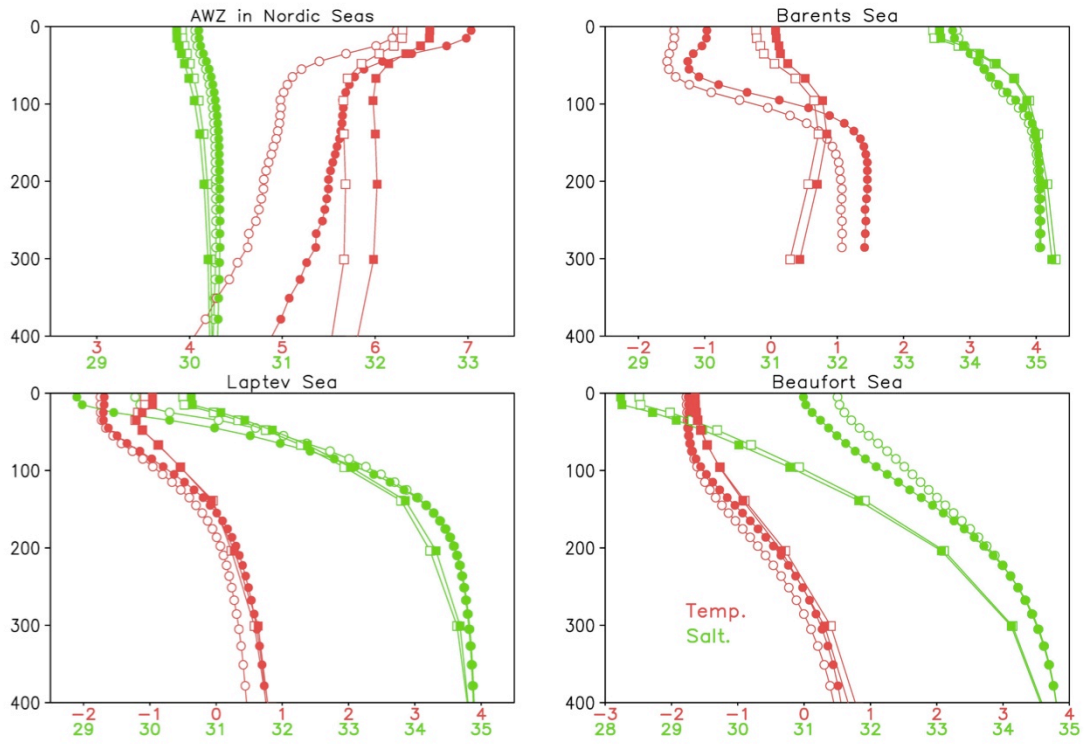

Figure 3.13: Temperature and salinity profile changes in recent 145 years in the defined four regions for CCSM4 (circle) and HadCM3 (square). Open circles and squares show the average temperature and salinity from 1861 to 1880, and closed circles and squares show the average temperature and salinity from 1986 to 2005.

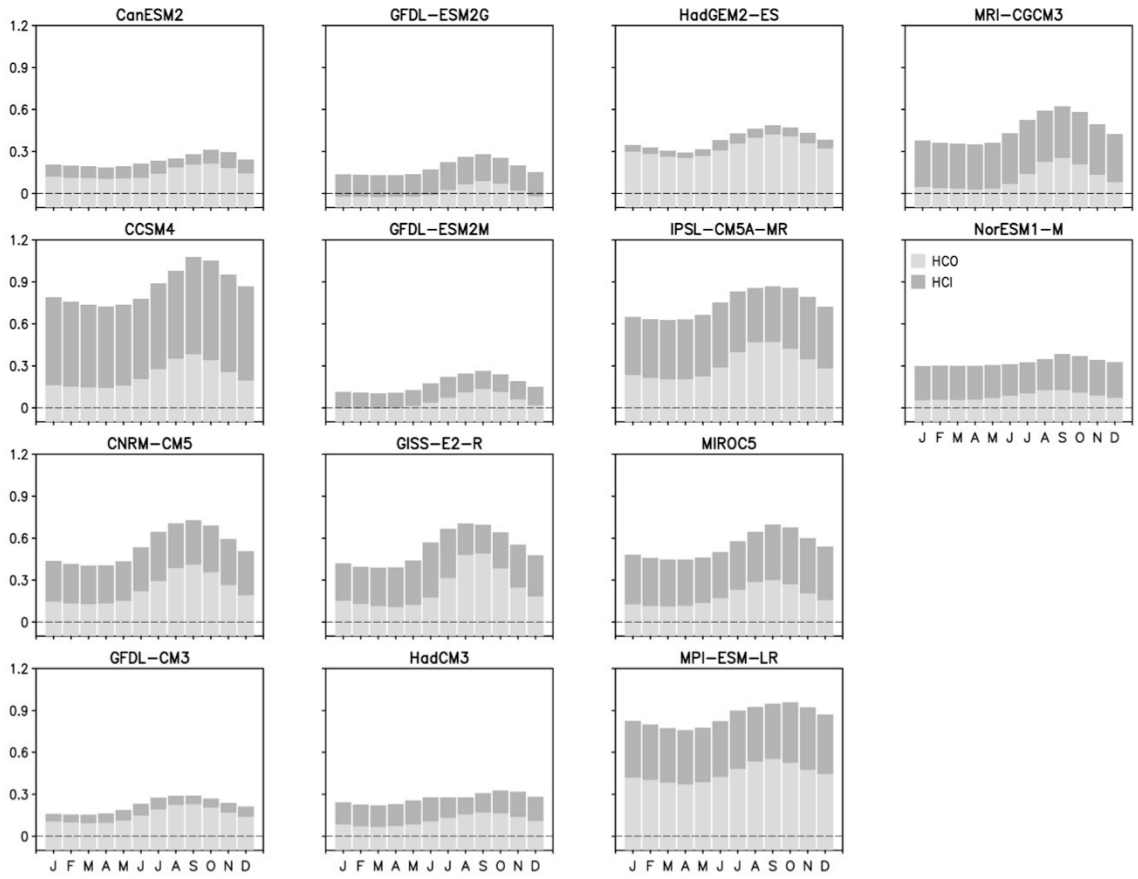

Figure 3.14: Seasonal cycle of ensemble mean mix-layer heat content increase (0-70m, light grey) and heat content increase due to sea ice melting (dark grey) in the Arctic Ocean. Increase of heat content is calculated as the 1986-2005 mean minus 1861-1880 mean.

The warming of ocean mix-layer and the decline of sea ice at the Arctic Ocean could be found in all models (**Figure 3.14**). The increase of ocean mix-layer heat content shows seasonal difference. In contrast, very few seasonal differences are found in the heat content change due to sea ice melting, and the reason for low seasonality is unclear. In CanESM2, GFDL-CM3, GFDL-ESM2G, HadCM3 and NorESM1-M, the seasonal cycle of ocean mix-layer heat content is weaker than in other models. The warming of mix-layer is also weaker in these 5 models. In addition, those models show weaker seasonal differences in surface net flux changes

as well (**Figure 3.11**). On seasonal time scale, over 96% of the heat content changes could be explained by the surface net fluxes changes. The most significant warming happens in MPI-ESM-LR with ~ 0.5 °C mean temperature increase. However, an intense warming in the mix-layer does not necessarily cause significant melting of sea ice. For example, the temperature increase in NorESM1-M is smaller than that in HadGEM2-ES, meanwhile there is larger amount of melting sea ice in NorESM1-M.

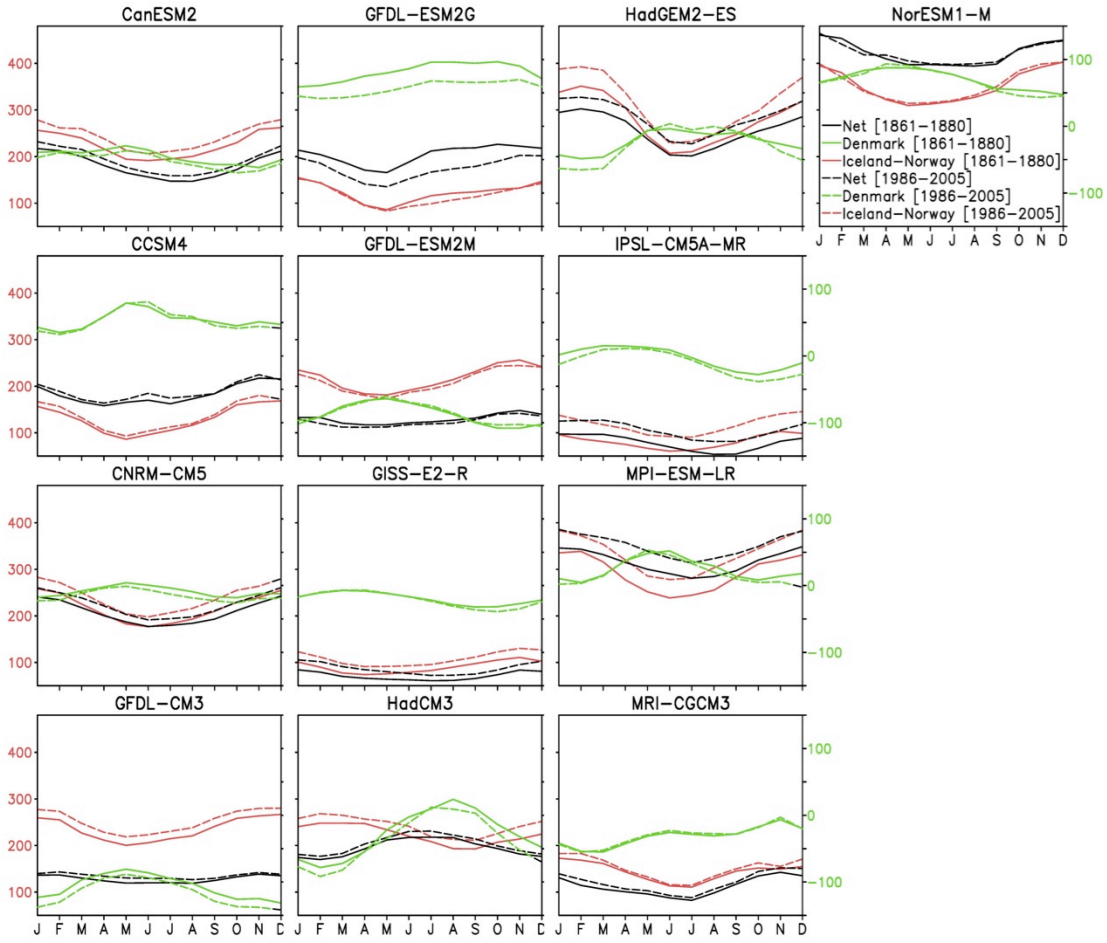

Figure 3.15: Seasonal cycle of heat flux changes through the Denmark Strait (red line, left Y axis), the Iceland-Norway Strait (green line, right Y axis) and total heat flux through these two straits (black line, left Y axis) for 1861-1880 (solid line) and 1986-2005 (dash line). Heat flux is calculated relative to 0°C. Units are TW.

Another factor that contributes to the heat content increase in the Arctic Ocean is the heat convergence from the four straits. During the last 145 years, the net heat transport into Arctic increases in all models, while this increase shows no seasonal differences (**Figure 3.15**). On interannual time scale, the impacts of surface net flux and heat transport on the heat storage changes are comparable for most models (**Table 3.5**). There are two exceptions: one is CCSM4 and another is MRI-CGCM3, in which the surface net flux still plays a more important role on heat content change. In MRI-CGCM3, the heat storage changing rate ($\partial HC/\partial t$) leads the heat transport by about 3 years with a correlation coefficient about 0.4.

Table 3.5: Correlation between changing rate of heat anomalies ($\partial HC/\partial t$) and surface net flux, and correlation between heat transports respectively for 14 CMIP5 models with seasonal cycle removed (from 1861 to 2005).

Models	CanESM2	CCSM4	CNRM-CM5	GFDL-CM3	GFDL-ESM2G	GFDL-ESM2M	GISS-E2-R
With surface net flux	0.60	0.83	0.57	0.66	0.37	0.55	0.58
With heat transport	0.56	0.38	0.40	0.46	0.37	0.54	0.41

Models	HadCM3	HadGEM2-ES	IPSL-CM5A-MR	MPI-ESM-LR	MRI-CGCM3	NorESM1-M
With surface net flux	0.48	0.52	0.57	0.46	0.85	0.42
With heat transport	0.33	0.52	0.40	0.62	-0.15	0.51

3.4.3 Salinity changes in the Arctic Ocean

Models with similar upper layer salinity distribution to the SODA reanalysis also exhibit similar salinity changes in recent two decades, which means increasing salinity at Russian side of the Arctic and decreasing salinity at the Beaufort Gyre

(**Figure 3.16**). It seems that the circulation pattern in the Arctic Basin can regulate the spatial pattern of salinity changes. In HadCM3, salinity decreases at the eastern

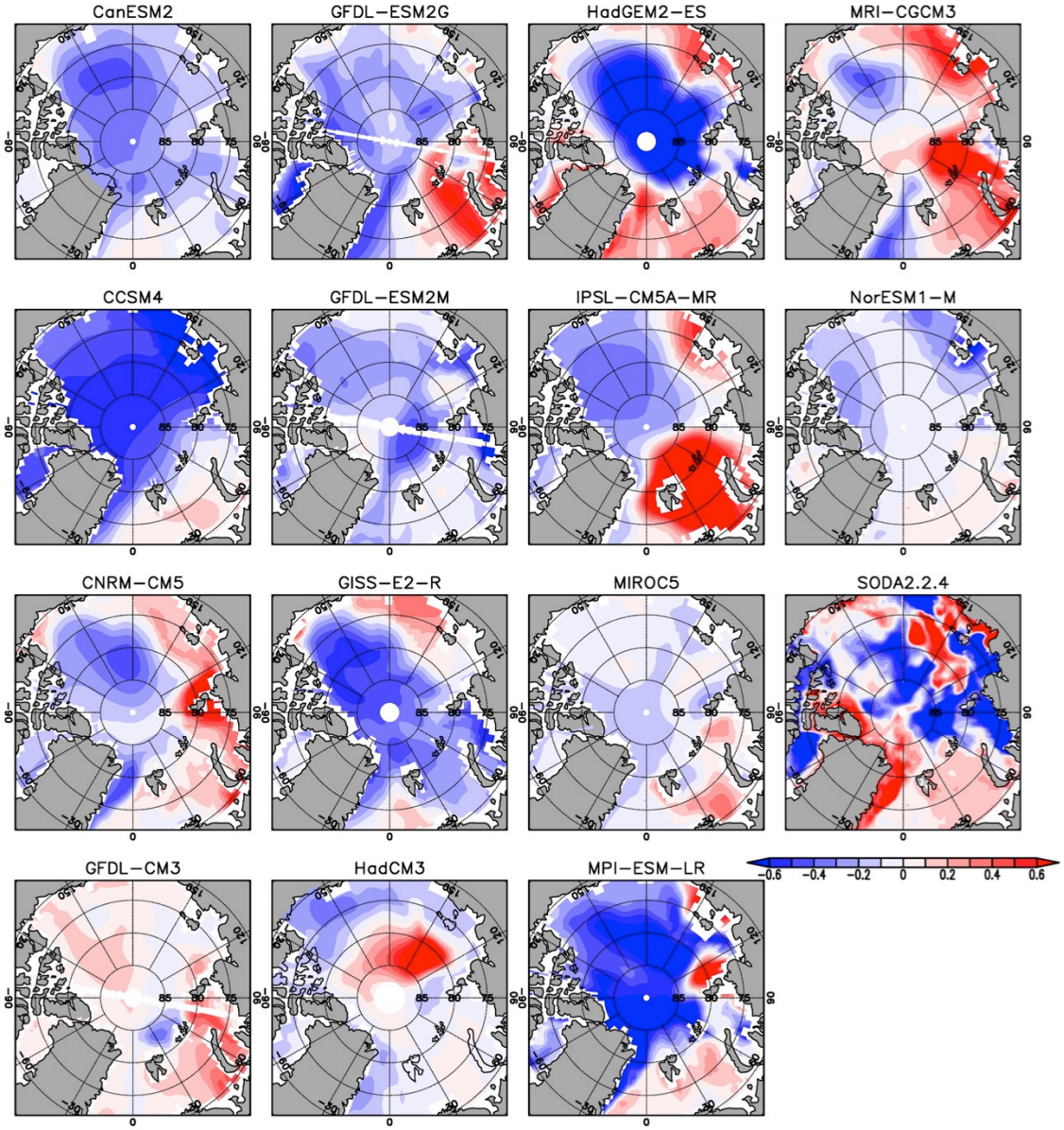

Figure 3.16: Upper ocean salinity (0-100m average) difference over high latitude ocean for 14 CMIP5 models and SODA reanalysis data. Difference is defined as the 1986-2005 mean minus 1861-1880 mean for models, and 1986-2005 mean minus 1871-1880 mean for SODA.

Beaufort Gyre but increases at the western part. Models with greatest sea ice melting, like CCSM4 and MPI-ESM-LR, also present most significant salinity decrease over the whole Arctic Basin.

3.5 Summary

This study examines the response of the Arctic Ocean to the green house gas forcing, and how atmosphere, ocean and sea ice affect each other interactively on seasonal and centennial time scale based on the historical simulations from 14 CMIP5 coupled climate models. All models capture the basic seasonal pattern of the Arctic surface meteorology. The seasonal cycle of surface net flux is strongly dependent on the cloud fraction and sea ice extent. The strength of Polar high determines the atmospheric circulation pattern, which in turn affects the strength of the Beaufort Gyre. Models with a similar Polar high strength to observations present a similar upper ocean salinity distribution in Arctic Basin with relative fresh water in Beaufort Gyre and Russian side of Arctic.

The warming of the Arctic Ocean is found in all models with enhanced downward surface heat flux, retreat of sea ice, increased temperature of mix-layer sea water, enhanced heat convergence into the Arctic, and changes of upper-layer salinity in the Arctic Basin. However, the amplitude of Arctic warming as well as the seasonal difference is different among models.

The heat content of sea water in the mix-layer increases with a clear seasonal cycle. In contrast, the amount of melting sea ice presents very few seasonal variations, and the reason is not clear. The seasonal variability in the mix-layer heat content is largely determined by the surface heat flux with a correlation coefficient of

96%, which confirms the previous study in *Serreze et al*. [2007b]. In models with strong seasonal cycle of surface net flux, the centennial decreasing trend of sea ice cover is comparable in all seasons. The retreat of sea ice extent in winter allows more evaporation at the ocean surface, which increases the upward latent heat flux and decreases oceanic heat gain.

The increasing trend of heat transport into the Arctic Basin exhibits very limited seasonal difference in most models. Both the surface net flux and heat convergence are important to the warming of sea water in recent decades.

The spatial pattern of salinity changes in the Arctic Ocean varies among models. Models with similar Polar high strength to observations present similar salinity changes to observations, which is more saltier sea water in the Laptev Sea and more fresher water in the Beaufort Gyre. Other models in which the strength of Polar high is either weaker or stronger than the observations fail to capture this spatial pattern. This indicates that the atmospheric circulation has a significant impact on the regulating the salinity distribution in recent decades.

Chapter 4: Subarctic/Arctic decadal climate: insights from CMIP5

4.1 Introduction

Observational studies have found intense decadal variability in the Nordic Seas region of the northern ocean, a region of high climate sensitivity [*Furevik*, 2001; *Carton et al*., 2011]. This same region is also subject to intense winter storm variability associated with atmospheric blocking events which disrupt the eastward movement of Atlantic storms [*Rex*, 1950a,b]. In this study I explore the origin of decadal ocean variability in the Nordic Seas and in particular its relation to variability in atmospheric blocking events. I focus on how differences in the simulations of blocking events influence the sub-Arctic ocean field on interannual to decadal time scales. Since the observational data are limited, I turn to historical simulations taken from the archive of the Coupled Model Intercomparison Project Phase 5 (CMIP5), which provide multi-model and multi-ensemble data sets of the whole climate system from the mid-1800s to 2005.

When blocking happens over the North Atlantic, a large amount of air is isolated from the mid-latitude jet stream, which develops an anti-cyclonic circulation, reduces the speed of zonal flow and alters Atlantic storm tracks [*Rex,* 1950a,b; *Woollings et al.*, 2008; *Häkkinen et al.*, 2011]. As shown in **Figure 4.1**, a high-pressure ridge develops at where the blocking happens, which makes the original westerly flow move along the high-pressure system. Thus, the blocking onset weakens the strong zonal flow and reduces the energy state of atmosphere as well as the strength of

Atlantic storm tracks [*Rex,* 1950a,b]. There are two frequent locations of the North Atlantic blocking events: Greenland and western Europe.

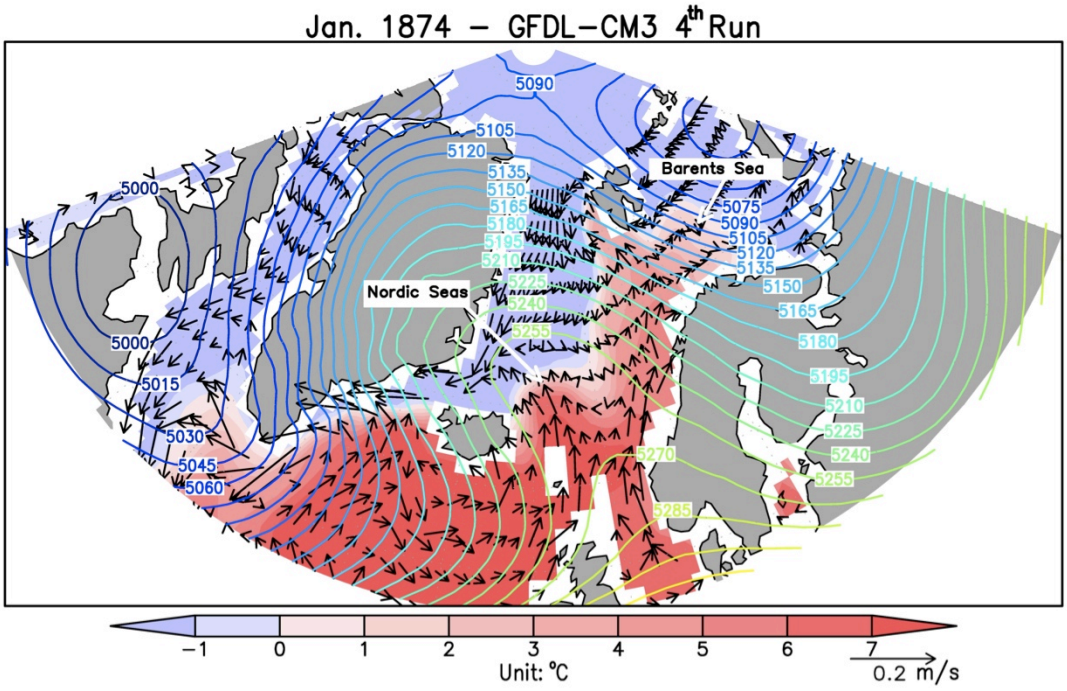

Figure 4.1: Example of geopotential height (contours, units: mb), surface ocean velocity (arrows, units: m/s), and SST (°C) from GFDL-CM3 for a month with persistent Greenland atmospheric blocking (>19 days).

Recent studies show that the presence/absence of blocking over Greenland is reflected in the negative/positive phase of the first empirical orthogonal eigenfunction of North Atlantic sea level pressure (*Woollings et al.* 2008 found a correlation of -0.47) [*Croci-Maspoli et al*., 2007; *Woollings et al.*, 2008; *Woollings et al.*, 2010]. This dominant mode has the character of a dipolar oscillation between the subtropical high-pressure and the mid-latitude low-pressure and is one way to define the North Atlantic Oscillation (NAO) [*Hurell*, 1995]. The cause of this relationship is an open research question. One group of studies suggest that the breaking of the jet stream

induces an anti-cyclonic atmospheric circulation pattern in the northeastern Atlantic, which leads to the negative phase of NAO [*Benedict et al.*, 2004; *Franzke et al*., 2004; *Wollings et al.*, 2008]. Other studies argue that anomalously high pressure over the subpolar ocean, which is the result of NAO in its negative phase, is preferable for occurrence of blocking events because of its modification of planetary waves [*Shabbar et al.*, 2001; *Luo* 2005; *Huang et al.*, 2006; *Barriopedro et al*., 2006]. It's also been suggested that NAO and blocking events over the North Atlantic are simply two different descriptions of one phenomenon [*Luo et al.*, 2007, *Berrisford et al.*, 2007]. The decreasing frequency of winter-time blocking at the Euro-Atlantic sector is associated with the eastward displacement of the NAO pattern position and the zonally distributed Atlantic storm tracks [*Ulbrich and Christoph*, 1999; *Jung et al.*, 2003; *Wollings et al*., 2012; *Davini et al*., 2012; *Zappa et al*., 2014].

In this study I examine a multi-model ensemble of historical runs from the most recent CMIP simulations. As discussed in Chapter 3, the basic state and seasonal cycles of these models span a wide parameter space. The mean sea level pressure over the high latitude oceans varies among models. The mean number of volume transports and heat transports into the Arctic Ocean also exhibits lots of variabilities. The similarity is that there is more heat transport into the Arctic through the Nordic Seas region in winter than in summer. On seasonal time scales, the heat content variation of the sub-Arctic and Arctic Ocean is controlled by the surface heat flux. On interannual to decadal time scale, both the surface heat flux and the oceanic heat advection play an important role on the variability of the sub-Arctic and Arctic Ocean.

In the past couple of years there has been considerable interest in looking at

blocking variability in these models, mainly because of the potential connection to North American wintertime climate. *Anstey et al.* [2013] has found that there are large differences in the frequency of blocking events among the CMIP5 models. One of the most significant differences is the blocking frequency over the Euro-Atlantic sector, which is generally underestimated than ERA-40 reanalysis data [*Anstey et al*., 2013; *Dunn-Sigouin and Son*, 2013; *Masato et al*., 2013]. The negative biases in blocking frequency over the Europe do not necessarily affect the ability of adequately simulating associated meteorological fields in some models [*Masato et al*., 2014]. The frequency of winter-time blocking over the North Atlantic shows no apparent decreasing trend under the warming background in CMIP5 simulations [*Dunn-Sigouin and Son*, 2013; *Woollings et al*., 2014].

My region of focus, Nordic Seas, is the region north of the Greenland-Scotland Ridge and south of the Fram Strait-Spitsbergen-northern Norway transect, including the Norwegian Sea, the Iceland Sea, the Greenland Sea and the Barents Sea (**Figure 4.1**). Approximately 8 Sv (1 Sv $=10^6$ m^3 s^{-1}) of Atlantic water flows into the Nordic Seas, and the Atlantic water inflow is strongest in winter [*Furevik*, 2001; *Carton et al.,* 2011; *Ding et al.,* in manuscript]. Some of the Atlantic water in the Nordic Seas region enters the Arctic Ocean through the Fram Strait and the Barents Sea Opening with comparable magnitudes [*Aksenov et al*., 2010]. Another water mass in the Nordic Seas is the fresh and cold Arctic water, which exports from the Fram Strait and moves along the east coast of Greenland.

The decadal-scale variability of temperature and salinity is a prominent feature of the subpolar gyre and Nordic Seas [*Venegas and Mysak*, 2000]. For instance, studies

have shown that the Nordic Seas warmed (and presumably salinified) in the 1920s–1930s 1960s, early to mid 1970s, 1983-1984, and early 1990s, and cooled down in the late 1960s, late 1970s, and late 1990s [*Swift et al.,* 2005; *Levitus et al.,* 2009a; *Matishov et al.,* 2009; *Furevik*, 2000; *Carton et al.,* 2011]. This decadal variability is mainly associated with the Atlantic Water in the eastern Nordic Seas. Since the Atlantic water moves into the Arctic through the Fram Strait and the Barents Sea Opening, its climate variability could affect the Arctic climate.

Atmospheric blocking events over the North Atlantic affect the climate variability of the Nordic Seas in two ways: changing the local heat flux and altering the ocean circulation pattern through wind-driven forcing of ocean currents. When a blocking event happens, the anti-cyclonic pressure anomaly on the northern North Atlantic pushes the low-pressure center and the storm track southward. At the low-pressure center, storminess reduces the local surface heat fluxes. Heat is transported to the east along the storm tracks [*Dickson et al*., 1996; *Rogers*, 1997; *Eden and Jung*, 2001]. The ocean currents induced by a blocking event is illustrated in **Figure 4.1.** The anti-cyclonic atmospheric circulation drives more warm Atlantic water to the western part of the Norwegian Sea. In contrast, the Atlantic water moving along the Norway coast slows down and the western branch of Atlantic water speeds up. The fact that more Atlantic water is driven to the west increases the total area of Atlantic water in the Nordic Seas, and enhances the heat loss from the ocean to the atmosphere. As a result, the Nordic Seas cool down. In addition, weaker Atlantic water inflows through the Barents Sea Opening and the Fram Strait decrease the heat advection into the Arctic.

Previous studies argue that more Atlantic water is driven to the eastern part of the Norwegian Basin and less to the western part when NAO in its positive phase [*Blindheim et al.,* 2000; *Furevik*, 2001; *Drange et al*., 2005; *Dickson et al.*, 2008]. This is opposite to the impact of blocking events. Observational studies have shown that in the eastern Svinøy section and the Barents Sea, both temperature and salinity are positively correlated with the strength of the North Atlantic low-pressure center [*Mork and Blindheim*, 2000; *Dickson et al.*, 2000].

Strength of the North Atlantic low-pressure center is positively correlated with the sea ice extent in the Barents Sea [*Sorteberg and Kvingedal*, 2006], and negatively correlated with the sea ice exports from the Fram Strait [*Hilmer and Jung*, 2000, *Serreze et al*., 2007]. In recent decades, the location of Atlantic storm tracks has moved further east [*Ulbrich and Christoph*, 1999; *Jung et al.*, 2003; *Wollings et al*., 2012], which may bring a larger impact of NAO on the sea ice exports through the Fram Strait [*Serreze et al*., 2007]. How the sea ice at the Barents Sea is correlated with the blocking event and the storm track over the North Atlantic is investigated in this study.

Another region influenced by blocking events in the North Atlantic is the subpolar ocean. The subpolar ocean becomes warmer and more saline when there are frequent blocking events in winter [*Häkkinen et al.*, 2011]. The deep water formation process at the Nordic Seas and the Labrador Sea, which is located at the western subpolar ocean, is closely linked with Atlantic Meridional Overturning Circulation (AMOC) [*Kuhlbrodt et al*., 2007]. Therefore, blocking events at the North Atlantic sector may have impact on the strength of AMOC through altering the surface water temperature,

salinity and density in the Nordic Seas and the subpolar ocean.

Section 4.2 briefly describes the fourteen CMIP5 models, several observational data sets and methods applied in this study. In Section 4.3, I discuss the decadal variabilities of the atmosphere and the ocean as well as the correlation between these two. Conclusion is presented in Section 4.4.

4.2. Data and methods

4.2.1 Data description

145 years (1861–2005) of historical simulations obtained from fourteen CMIP5 models are analyzed in my study. A brief description of the selected models is shown in **Table 3.1**. All fourteen models include multiple ensembles. Most of the model outputs were obtained from the online archive (http://pcmdi3.llnl.gov/esgcet/home.htm), while for some ensembles of two GFDL-ESM models, data was obtained directly from Geophysical Fluid Dynamics Laboratory model working group. Most data are of monthly time resolution, but the geopotential height data is of daily resolution. Daily geopotential height data are available for all models except for GISS-E2-R. Geopotential height data are only available for certain ensemble and certain time period for most models. Full time coverage of geopotential height data is available for five ensembles of GFDL-CM3, 1st ensemble of GFDL-ESM2M and GFDL-ESM2G. Because the winter-time blocking days in model simulations show very little long-term changes, the mean blocking day in each model is calculated over their available time coverage.

Ocean field outputs in ten models are of irregular horizontal resolution. In order to do spatial comparison among models, ocean temperature and salinity data are

remapped to 1°×1° resolution using climate data operators (CDO). Calculations of volume transports through the Fram Strait (~79°N) and the Barents Sea Opening (~20°E) are applied on the original ocean grids to avoid biases on the mass budget calculation. For HadCM3, which contains a "rigid-lid" ocean model, the volume flux is calculated as $\iint v(x,z)dxdz$, where $v(x,z)$ is the monthly mean ocean velocity normal to sides of the volume, x is the along-side distance coordinate, and z is the vertical coordinate. For the rest "free surface" ocean models, volume flux is calculated from mass transport data. Volume transport for MIROC5 is not available because no mass transport data available for its "free-surface" ocean model.

Heat content is calculated from surface to 1000m deep ($\rho C_p \int_{1000m}^{0} T dz$) where r and C_p are assumed to be constant. Heat content from Simple Ocean Data Assimilation version 2.2.4 reanalysis estimates of *Carton and Giese* [2008] is added for comparison.

4.2.2 Definition of blocking events

In this study, the blocking is defined following the two-dimensional reversal north-south dynamic height gradient definition [*Scherrer et al.*, 2006; *Häkkinen et al*., 2011]. One gridpoint is considered as blocked if there is a strong negative northward gradient (GHGN) (<–10 m/°latitude) and a positive southward gradient (GHGS) of geopotential height at 500mb, and this reversal north-south gradient needs to persist for 5 days or longer. The GHGN and GHGS for certain grid point are calculated as follows:

$GHGN = (Z(\lambda,\Phi_N) - Z(\lambda,\Phi_o)) / (\Phi_N - \Phi_o)$,

GHGS = $(Z(\lambda,\Phi_S) - Z(\lambda,\Phi_o)) / (\Phi_S - \Phi_o)$, where Z is the 500hPa geopotential height, λ is longitude, Φ_N, Φ_S and Φ_o are northern, southern and center latitudes respectively, and $|\Phi_{N|S} - \Phi_o| = 16$ degrees. We are interested in the winter-time (DJFM) blocking event over the North Atlantic sector with the latitude ranges from 45°N to 74°N, which exclude the subtropical blocking event. For each day, if there is one blocked grid (belonging to a 5-day block) at the North Atlantic sector, it is considered as a blocking day. Index of winter-time blocking days is the summary of blocked days from December to March for each year.

In this study, we use a NAO definition based on the Principal Component time series of the leading Empirical Orthogonal Functions (EOF) in the sea level pressure (SLP) in the North Atlantic Sector [*Wallace and Gutzler*, 1981; *Dickson*, 2000]. The winter-time (DJFM) SLP is used for the EOF analysis, which produces a NAO index of yearly resolution. Observational SLP data from HadSLP2 [*Allan and Ansell*, 2006] is applied here for the comparison with model simulations. The leading phase of the EOF analysis of SLP presents a similar NAO pattern to the observations in all models although the locations of the simulated Azores high and Icelandic low vary from model to model. The leading EOF phase could explain 38% to 67% of the SLP variance in CMIP5 models. In comparison, about 56% of the HadSLP2 variance could be explained by its leading EOF phase.

4.2.3 Definition of Atlantic water

Definition of Atlantic water in the Nordic Seas follows the salinity definition in *carton et al.* [2011] with modified salinity criteria in different models (shown in **Table 4.1**). Salinity distribution in the Nordic Seas show variations among models

but the basic pattern is consistent with two branches: one flowing into the Barents Sea and another across the Fram Strait. Because it is of high probability that the surface heat flux anomaly over the Greenland-Iceland region and that over the Nordic Seas are of different signs [*Hann*, 1890; *Dickson et al.* 1996], we consider the climate variability of Atlantic water at the eastern Nordic Seas (63°N to 80°N, 15°W to 60°E) and Atlantic water at subpolar ocean separately.

Table 4.1: The minimum salinity of defined Atlantic water in different models.

Model	CanESM2	CCSM4	CNRM-CM5	GFDL-CM3	GFDL-ESM2G	GFDL-ESM2M	GISS-E2-R
Criteria	35.2	35.0	34.3	35.0	35.0	35.0	34.7
Model	HadCM3	HadGEM2-ES	IPSL-CM5A-MR	MIROC5	MPI-ESM-LR	MRI-CGCM3	NorESM1-M
Criteria	35.0	34.9	34.7	35.0	35.0	34.6	35.3

4.3. Atmospheric blocking in CMIP5 historical simulations

4.3.1 Blocking events over the North Atlantic

In this section we examine the variabilities of the atmosphere and then the ocean as they appear in the coupled models, and look for relationships between these two. A key feature of the winter climate, as pointed out in the Introduction, is the persistence of blocking events in some years. Winter-time blocking events at mid latitudes are found in all models. Frequency of the blocking event at the North

Pacific Ocean shows fewer variations than that at the Euro-Atlantic sector (**Figure 4.2**). Three typical blocking patterns are found at the Euro-Atlantic sector: 1) rare blocking events as shown in CCSM4, 2) fewer blocking events over Greenland and more over western Europe as shown in GFDL-CM3, 3) more blocking events over

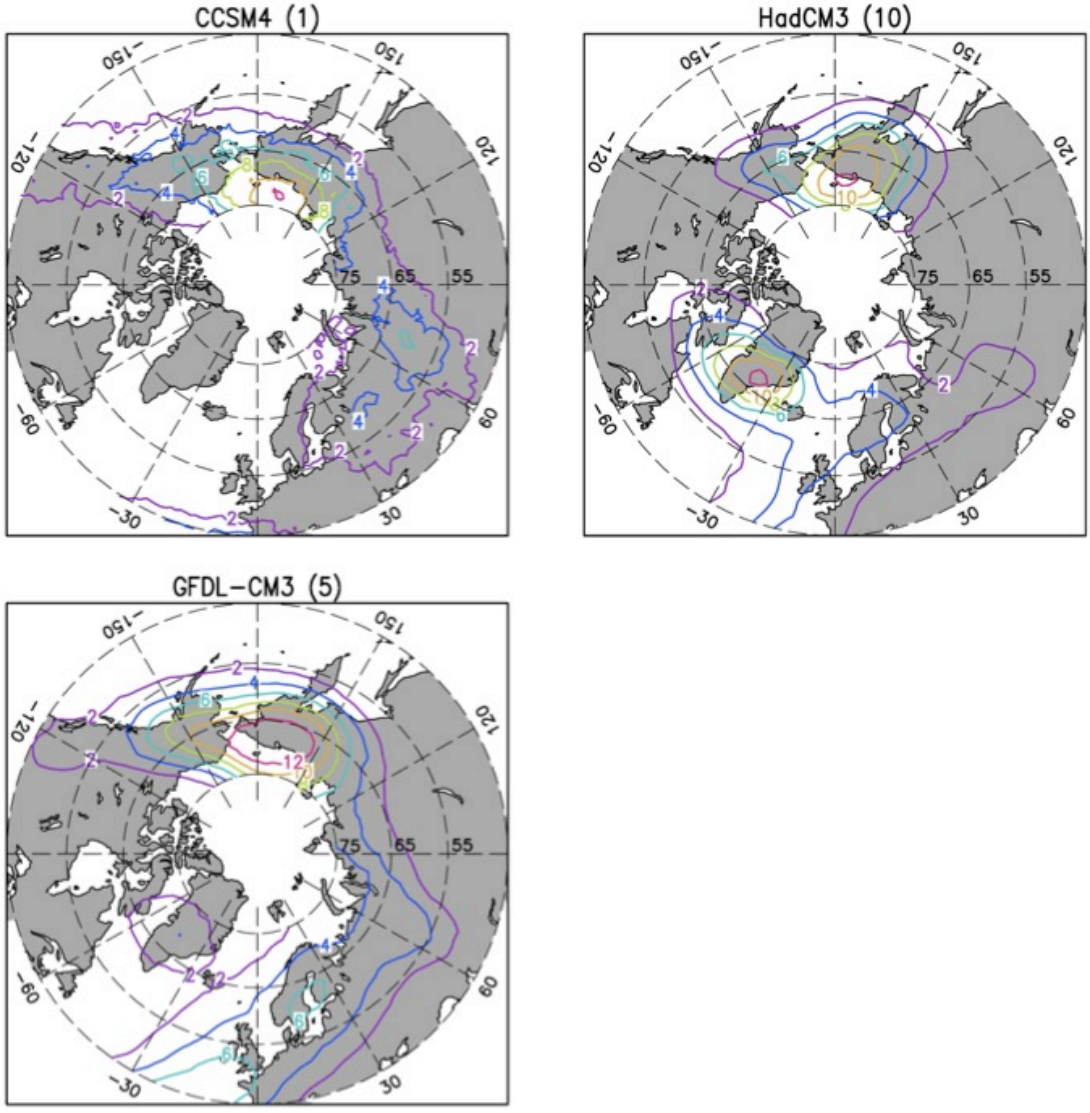

Figure 4.2: Mean winter-time (DJFM) blocking days in North Hemisphere for CCSM4, GFDL-CM3 and HadCM3, which present three types of blocking distributions over Greenland and western Europe seen among the CMIP5 models considered here. CCSM4 have only one ensemble with daily blocking data, while GFDL-CM3 and HadCM3 have five and 10 ensembles separately.

Greenland and fewer over Europe as shown in HadCM3. The spatial pattern presented in GFDL-CM3 is closer to that in the National Centers for Environmental Prediction/National Center for Atmospheric Research (NCEP/NCAR) reanalysis data [*Häkkinen et al.*, 2011]. The mean number of winter-time blocking days is closest to the NCEP/NCAR reanalysis, which is about 70 days, in HadCM3. The prediction of winter-time blocking days in other models is generally weaker than that in observations.

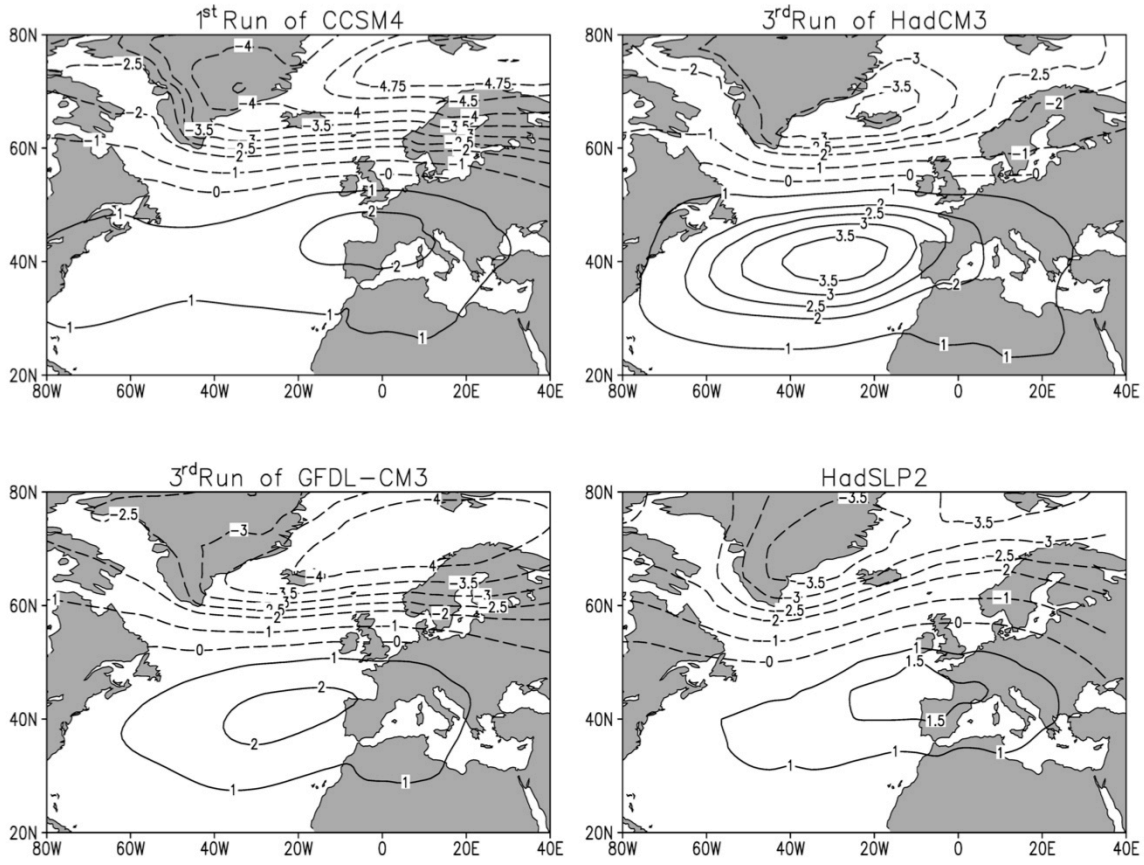

Figure 4.3: The first EOF pattern of winter-time (DJFM, 1861-2004) sea level pressure for the North Atlantic sector as represented in CCSM4, GFDL-CM3, HadCM3 and observations (units: mb).

4.3.2 Relationship between the Greenland blocking and NAO

Different spatial distributions of blocking over the northern North Atlantic are reflected in the location of the low-pressure center over the North Atlantic Ocean. The first phase of EOF analysis presents a clear NAO pattern in each model and in each ensemble. However the strength and location of the low-pressure center vary among different models and different ensembles (**Figure 4.3**).

In general, strength of low-pressure center in model simulations is slightly stronger than that in HadSLP2. In models like HadCM3, the low-pressure center is over Iceland, which is close to where it is in HadSLP2, while for GFDL-CM3 and CCSM4, the low-pressure center has moved northeastward to the Nordic Seas and the Barents Sea respectively. The location of the high-pressure center also varies among models, and GFDL-CM3 presents the closest high-pressure location to observations.

Time series of winter-time blocking days and the NAO index show that frequent Greenland blockings usually co-occur with negative NAO phases in winter as indicated in *Woollings et al.* [2008] (**Figure 4.4**). On interannual time scale, no leading or lagging relationship is found between winter-time blocking days and the NAO index. When frequency of blocking events over the North Atlantic, especially over Greenland, increases, the low-pressure center moves northeastward, from Iceland to the Barents Sea.

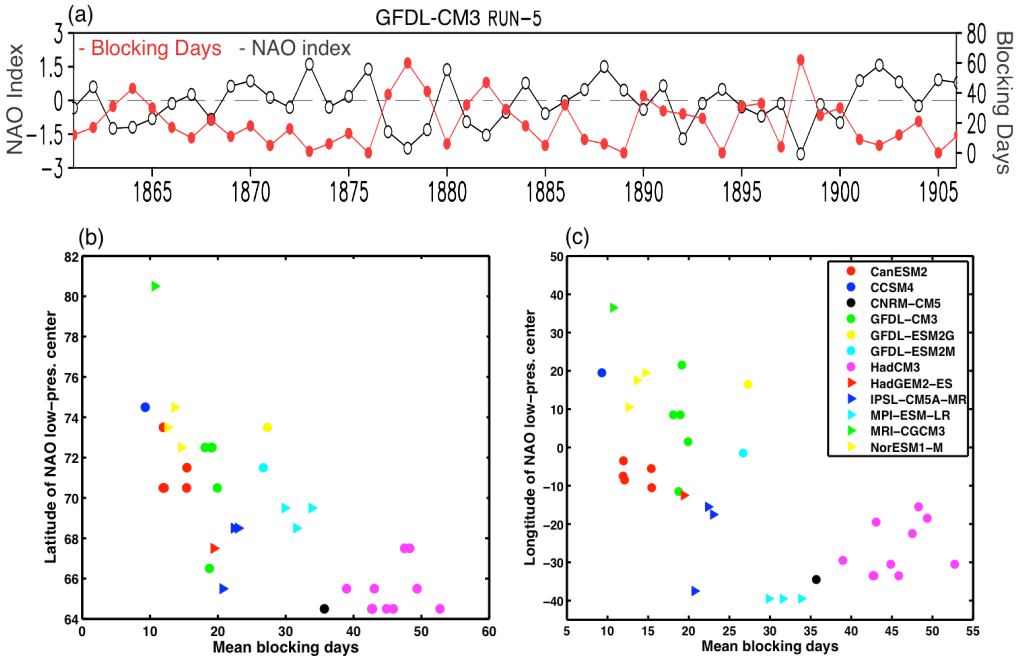

Figure 4.4: (a) Time series of the frequency of winter-time (DJFM) blocking days plotted against the NAO index for GFDL-CM3 ensemble member #5. (b) Relationship between mean blocking days and the latitude of the low-pressure center of the NAO (see **Figure 4.3**). (c) Similar to (b) except for longitude.

4.3.3 Impacts of blocking events on surface heat flux

The frequency of blocking and the location of the NAO low-pressure center also present different impacts on surface net fluxes. Here we use the NAO index to do the correlation because the time series of blocking days suffers from shorter time period and is out of phase with NAO index. The location of regions with the most significant decreasing impact moves eastward from ~50°W to ~20°W with the eastward movement of storm tracks, which is a result of decreasing frequency of Greenland blocking events (**Figure 4.5**). Eastward movement of storm tracks changes the pathway of heat transports from the North Atlantic Ocean to Europe.

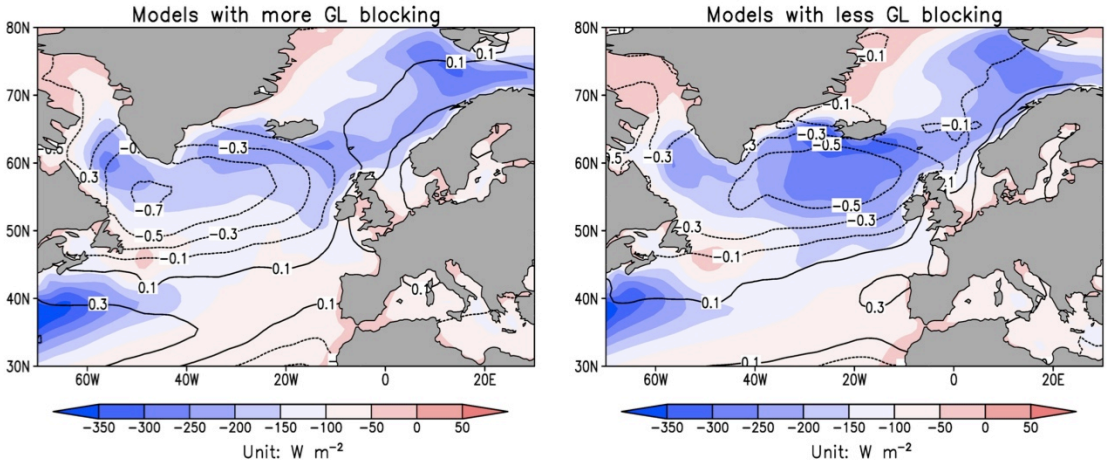

Figure 4.5: Correlation between surface net flux and the NAO index for models with frequent (contours, left panel) and infrequent (contours, right panel) Greenland blocking events. Color shows the time-mean winter-time (DJFM) surface net flux from 1861 to 2005.

4.4. Decadal variability of Atlantic water in the sub-Arctic seas

4.4.1 Decadal variability of the Atlantic water

Next I turn attention to the decadal variability of the high latitude ocean (**Figure 4.6**). On decadal time scale, the ocean heat content exhibits the largest variability over subpolar ocean and the Nordic Seas, which could be found in both Simple Ocean Data Assimilation (SODA) reanalysis data and CMIP5 model outputs. The Arctic Basin and the Pacific Ocean show less climate variability on decadal time scale. Variability of ocean heat content at the Nordic Seas is generally smaller in CMIP5 models than that in SODA reanalysis data. According to SODA, the ocean heat content variability in the Nordic Seas is of similar magnitude to the subpolar ocean, while in model simulations, it is about 2/3 of subpolar ocean variability.

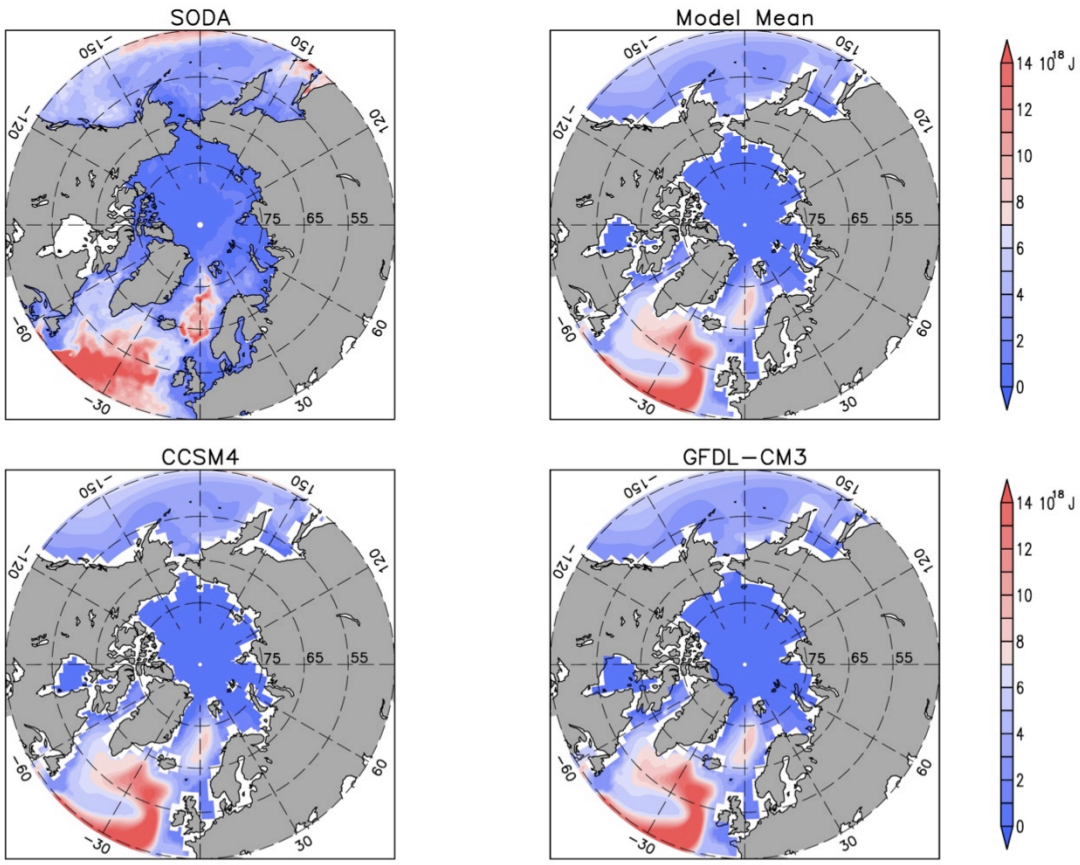

Figure 4.6: Root mean square heat content from observations (upper left), ensemble mean of all 14 models (upper right), and CCSM4 and GFDL-CM3 (lower panels). Heat content is calculated from surface to bottom. Both seasonal cycle and the long-term trend have been removed. Data are running two-year average.

The temperature profiles of Atlantic water in the Nordic Seas indicate the presence of warm and cold events in all models, which are strikingly similar in amplitude and timescale to observed events (**Figure 4.7**, also *carton et al*., [2011]). The warm events are generally characterized by salty water and cold events co-occur with reduced salinity as the observations show, although there are some exceptions as well. For example, the warm event starting from 2003 in the 3rd ensemble of GFDL-CM3 co-occurs with decreased salinity.

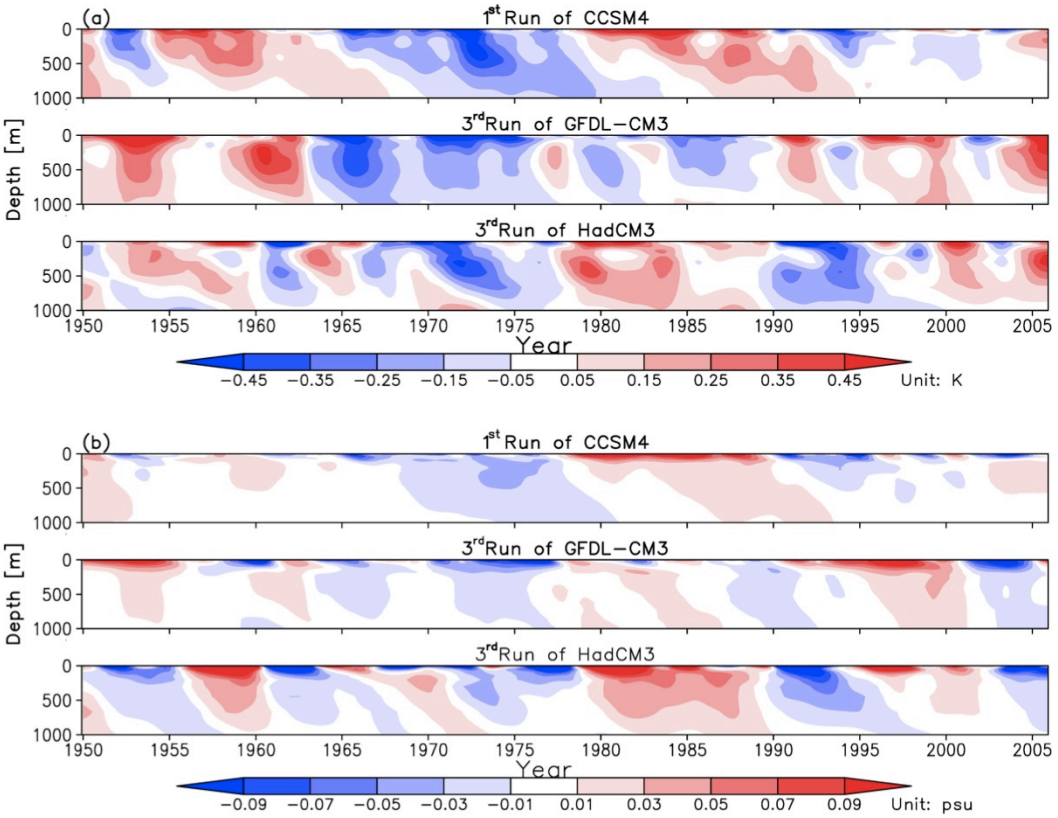

Figure 4.7: a) Temperature profiles and (b) salinity profiles of the Nordic Seas Atlantic Water region for CCSM4, GFDL-CM3 and HadCM3. The seasonal cycle and linear trend have been removed and data have been low-pass filtered with a running two-year average.

Atlantic water in different ensembles presents different temperature and salinity variabilities. Decadal variability is also found in the subpolar ocean in all these CMIP5 models. Generally, there is a weak correlation between heat content in the Nordic Seas and the subpolar ocean except for MRI-CGCM3, in which subpolar heat content changes lead the Nordic Seas by ~3 years with correlation coefficient as large as 0.6.

4.4.2 Origin of decadal variability of Atlantic water

One big difference of decadal variability in the Nordic Seas among these models is the relative importance of vertical heat propagation from surface and lateral heat advection. In models with infrequent Greenland blocking events, like CCSM4, there is clear heat propagation from surface to deep ocean in the Nordic Seas via recirculation in the basin. Generally, it takes about one decade for the surface temperature anomaly to reach 1000m deep. In models with frequent Greenland blocking events, like GFDL-CM3 and HadCM3, the vertical heat propagation is not significant because temperature anomalies at different ocean layers occur at similar times for most cases. The weakness of vertical heat propagation in those models suggests that heat anomalies in the whole water column are created at the same time, which is likely with lateral heat advection. Vertical propagation of salinity anomalies is similar to heat propagation.

Evidence of heat advection in HadCM3 is apparent in the sea surface temperature (SST) field (**Figure 4.8**). SST in the subpolar ocean leads SST in the Nordic Seas by about 4 years, and the Nordic Seas SST leads SST in the Barents and Kara Seas by about 2 years with correlation coefficient as large as ~0.5. It takes about 6 years for heat to be transported from the subpolar ocean to the Barents and Kara Seas, while this trend is weaker in GFDL-CM3 and almost disappears in CCSM4. Correlation between downward surface net flux and the rate of heat storage anomalies ($\partial HC/\partial t$) also indicates that CCSM4 is a heat flux controlled model where local surface heat flux can explain over ~70% of the heat content changes. But in models with high frequency of Greenland blocking events, like HadCM3, only ~20% of heat

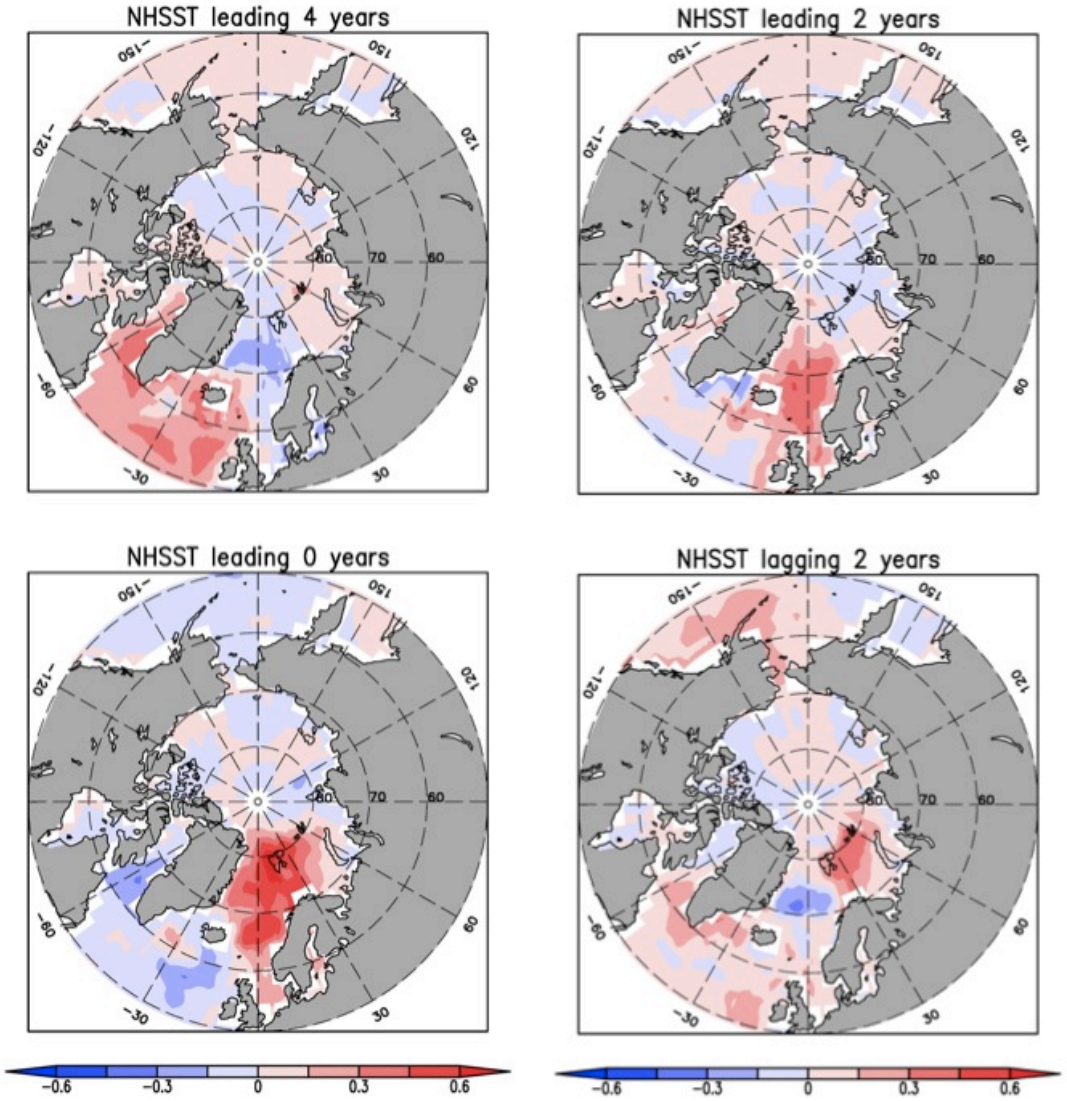

Figure 4.8: Lead/lag correlation between the North Hemisphere SST and the SST in the Nordic Seas for HadCM3. The apparent northward progression of the correlation suggests the importance of heat advection in this model.

content variations could be explained by local surface heating (**Figure 4.9**). Surface net flux plays a more important role in the ocean heat content changes on interannual time scale (10^{-1} yr^{-1} < frequency < 2^{-1} yr^{-1}).

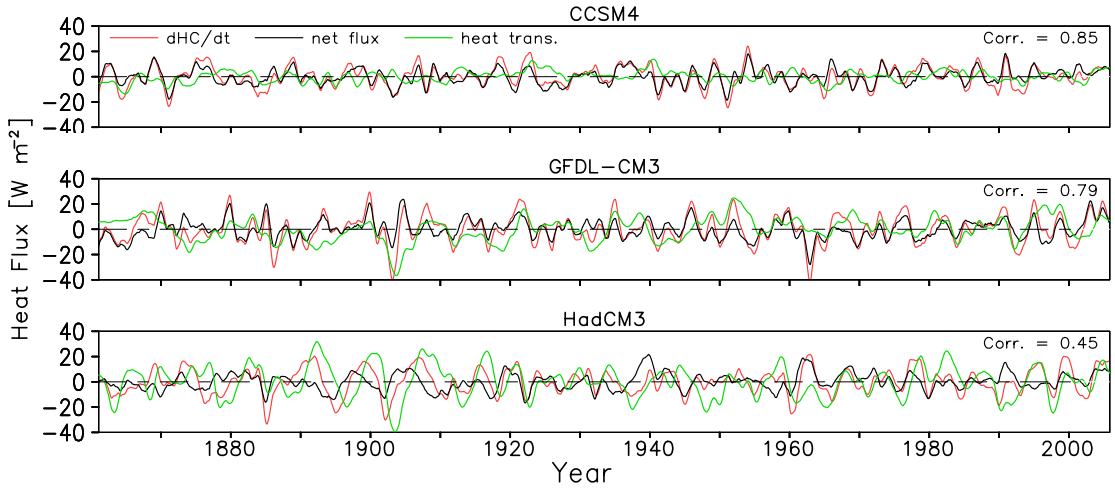

Figure 4.9: Time series of downward net surface flux and anomalous heat content tendency ($\partial HC/\partial t$) in the Nordic Seas Atlantic water region as it appears in CCSM4, GFDL-CM3 and HadCM3. Heat content is calculated from surface to 600m deep.

4.4.3 Impacts of blocking events on the decadal variability

Here I use the correlation coefficient of $\partial HC/\partial t$ and surface net flux to indicate the importance of surface heating. The winter-time blocking over Greenland is negatively correlated with the importance of surface heating (**Figure 4.10**). The correlation with statistical significance at the 5% level corresponds to a correlation coefficient ~0.53. If we consider blockings over Greenland and western Europe together, the correlation becomes slightly weaker with R^2 reduced from 0.53 to 0.45 at the 5% level of statistical significance. This relationship could be found at both interannual (10^{-1} yr^{-1} < frequency < 2^{-1} yr^{-1}) and decadal time scale (frequency >10^{-1} yr^{-1}), but more statistical significant on interannual time scale.

Correlation between $\partial HC/\partial t$ and heat flux through the Iceland-Norway strait is weakest in CCSM4 and strongest in HadCM3, although the difference among models

is weaker than that between $\partial HC/\partial t$ and surface net flux (**Figure 4.9**). The root mean square of heat flux in CCSM4 is 10 W m^{-2}, which is about 30% of surface net flux variations. In GFDL-CM3 and HadCM3, the ratio between heat flux and surface net flux increases to 50% and 90% respectively. The relative magnitudes of heat flux and local heating in different models could explain why the importance of heat flux on interannual to decadal variability of the Nordic Seas Atlantic water decreases with the reduced frequency of blocking events in different models.

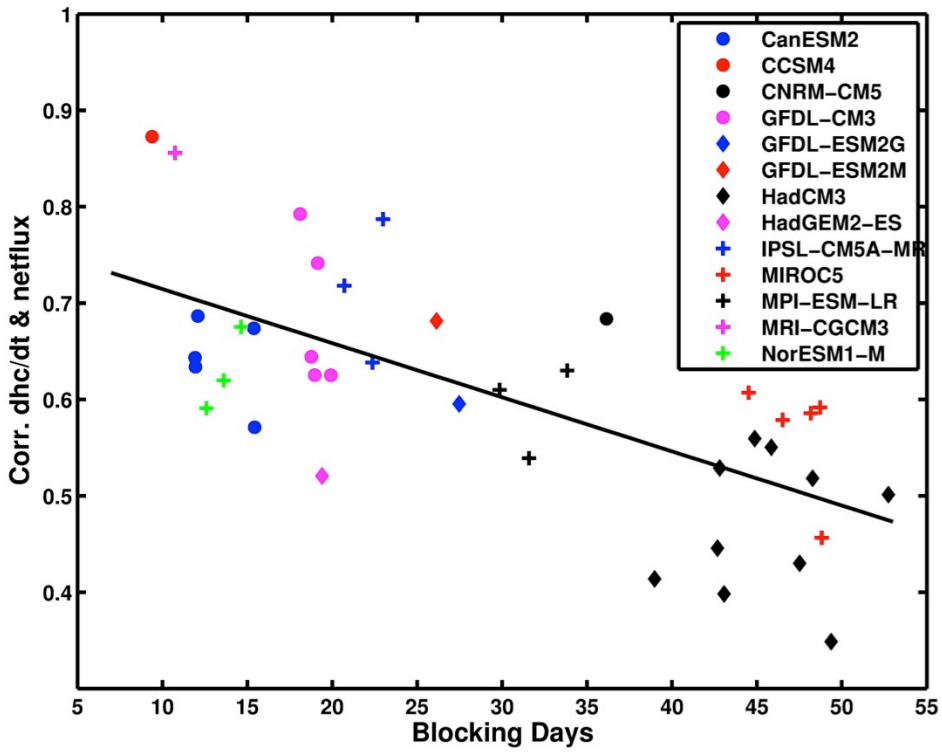

Figure 4.10: Relationship between mean winter-time (DJFM) blocking days over Greenland and the correlation coefficient between the heat storage changing rate ($\partial HC/\partial t$) and surface net flux of Atlantic water.

To study why the heat advection shows less variability in models with low frequency of Greenland blockings, I divided models into two different groups: models

with mean Greenland blocking days more than 25 and less than 25 days. Comparisons between their mean SLP and surface ocean velocity states are shown in **Figure 4.11**. In models with less Greenland blocking events, the low-pressure center expands from west of Iceland to the entire Nordic Seas, which causes a lower pressure gradient, smaller wind-driven force and weaker surface ocean velocity at Iceland-Norway strait. Another difference is the pressure over Greenland, which is much higher in models with low frequency of Greenland blocking events than models with high frequency.

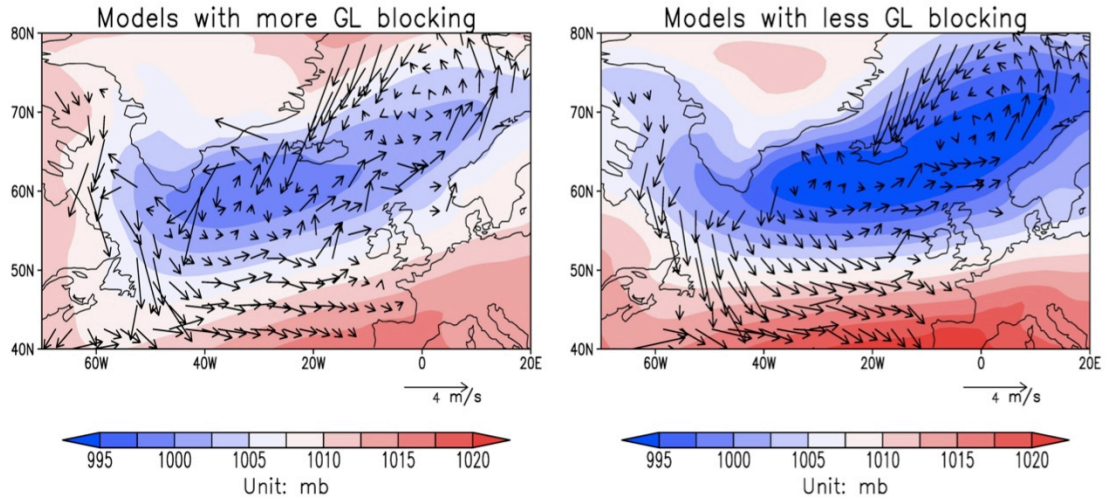

Figure 4.11: Mean state of winter-time ocean surface currents (arrows) and sea level pressure (color) for models with frequent (left panel) and infrequent (right panel) Greenland blocking events. Surface currents are normalized in all models.

I also compared the mean state difference of ocean surface currents and sea level pressure (**Figure 4.12**). Results show that for years with high frequency of Greenland blocking events, there is a similar effect to negative NAO, which shows a high-pressure center over the Nordic Seas and northwestward ocean current differences. Therefore, when the blocking frequency increases, less Atlantic water goes into the

Nordic Seas through the Iceland-Norway strait. The magnitude in models with infrequent Greenland blocking is four times larger than that in models with frequent blockings. One possible reason is that in models with frequent blockings, such as HadCM3, the variability of blockings days is smaller that in models with infrequent blockings.

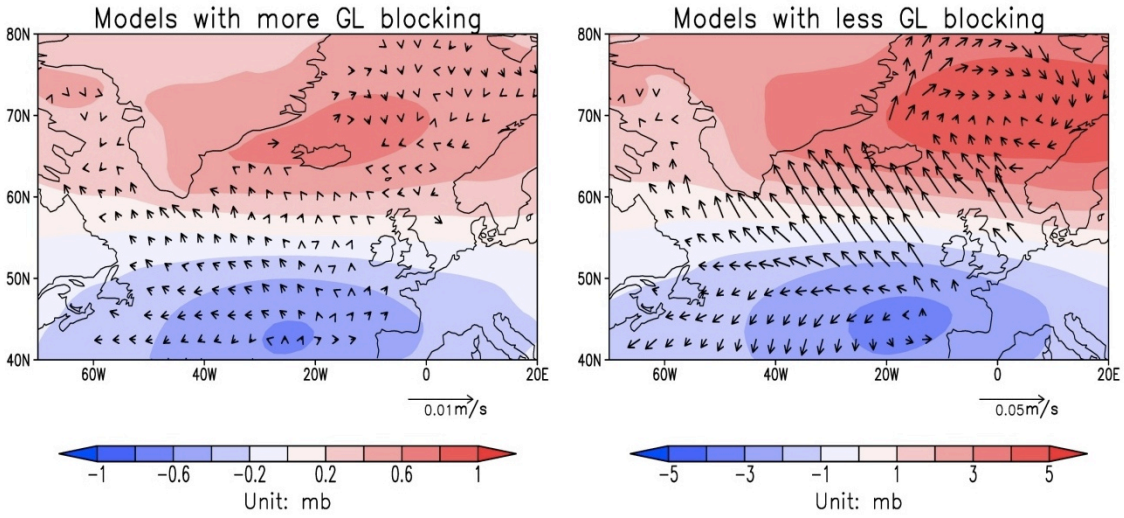

Figure 4.12: Difference of ocean currents (arrows) and sea level pressure (color) between years with more blocking days (larger than the mean value) and years with fewer blocking days. Models with frequent (left panel) and infrequent (right panel) Greenland blocking events are considered respectively here.

4.5 Decadal variability of the Arctic sea ice

Another important message we could get from **Figure 4.9** is that heat transport through the Iceland-Norway strait lags $\partial HC/\partial t$ by approximately 1 year. Taking the time period from 1890 to 1910 in HadCM3 as an example, the heat storage anomaly increases after surface net flux increases, followed by increasing of heat transport. The heat transport is determined by both the sea water temperature and the volume transport. For CMIP5 models I examine, over 80% of heat transport variations could

be explained by the volume transport variations. Therefore, when the Nordic Seas warm, there is more Atlantic water flowing into this region. One possible explanation for that is the sea ice variation at the Barents Sea. The surface wind forcing is important for volume transport through the Barents Sea Opening and Fram strait. Melting of sea ice at the Barents Sea is able to increase the Atlantic Water flux because when sea ice becomes thinner, more atmospheric momentum is transferred to the ocean. In addition, according to *Shimada et al*. 2006, if the boundary sea ice melts, which will reduce the large internal ice stress, will also increase the efficiency of atmospheric momentum transfer. The sea ice concentration at the Barents Sea is negatively correlated with the heat content of Atlantic water in the Nordic Seas on decadal time scale, with a mean correlation coefficient about -0.5 for all model simulations.

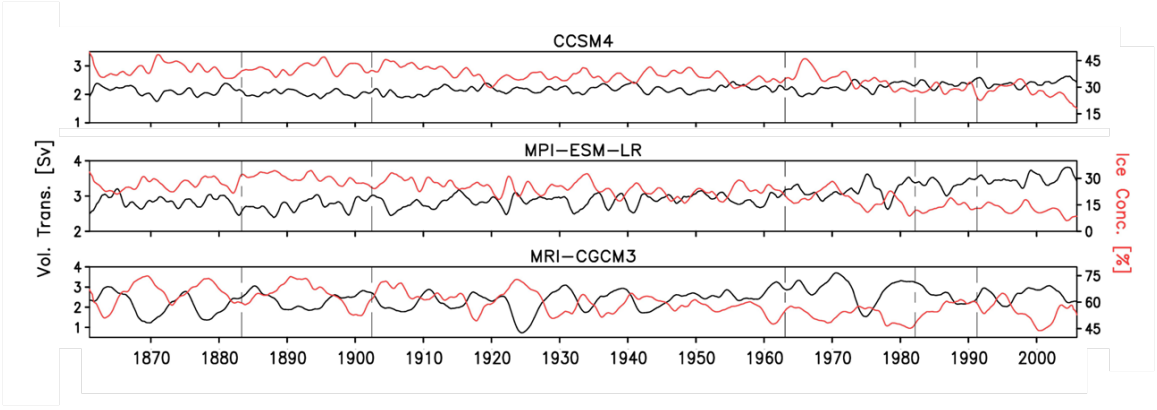

Figure 4.13: Area mean sea ice concentration over Barents Sea (red) and volume transport through Barents Sea Opening (black) for CCSM4, MPI-ESM-LR, and MRI-CGCM3.

Meanwhile, volume transport through the Barents Sea Opening into the Arctic Basin is negatively correlated with the sea ice extent in the Barents Sea (**Figure 4.13**), and the mean correlation coefficient from all models is about -0.8. The mean state of

sea ice concentration at the Barents Sea determines the strength of Atlantic inflow. In CCSM4 and MPI-ESM-LR for example, which are models with average and below average sea ice concentration at the Barents Sea, higher sea ice concentration is characterized by a smaller volume transport through the Barents Sea Opening. In MPI-ESM-LR, the intensified volume flux from the 1980s reduces the sea ice concentration at the Barents Sea to less than 10%, which would intensify the warming of Arctic. MRI-CGCM3 is the model with the largest volume transport variations and the largest variations of sea ice at the Barents Sea among models. Although there is no significant correlation between volume transport and the sea ice concentration at the Fram Strait, the volume fluxes through the Fram strait and the Barents Sea Opening are negatively correlated with correlation coefficient as large as -0.8.

When Atlantic water in the Nordic Seas warms, more sea ice at the Barents Sea melts and volume transport and heat transport into the Nordic Seas become stronger. AMOC is enhanced correspondingly although the correlation coefficient between volume transport and AMOC index is not big enough to say it is significant. Enhanced heat transport into Nordic Seas will further intensify the Atlantic water warming in the Nordic Seas. This process exists in all models, while impact of heat transports on decadal variability of the Nordic Seas is most significant in models with high frequency of blocking events. In addition, decreasing frequency of Greenland blocking events tends to enhance the volume and heat transports into the Nordic Seas although the correlation is not strong, with correlation coefficient generally smaller than -0.6.

4.6 Conclusion and discussion

Tropospheric blocking of the jet stream over the North Atlantic is an atmospheric phenomenon that usually lasts for several days, while its accumulated impact has the ability to affect the wind pattern and ocean circulation of the North Atlantic sector on decadal time scale. Its impact on the sub-Arctic ocean, especially the Nordic Seas, has received less attention. In this study, I examine the simulations of Greenland blocking events in 14 CMIP5 climate models and investigate its impact on the Nordic Seas.

Frequency of winter-time Greenland blocking events varies from model to model. One possible reason for the different blockings among these models is the different spatial resolutions [*Anstey et al.* 2013]. Models with few Greenland blocking events in general are characterized by a northeastward shift of the NAO low-pressure center, which reduces the wind-driven force and surface northward ocean velocity at the Iceland-Norway strait. Thus, heat advection into the Nordic Seas shows weaker decadal variability in models with lower frequency of Greenland blocking events, and surface heating plays a dominant role in the decadal variability of Atlantic water in the Nordic Seas. Surface net flux could explain ~70% of the heat storage anomalies.

The changing rate of heat storage anomalies ($\partial HC/\partial t$) leads the heat flux into the Nordic Seas by about 1 year. Sea ice melting at the Barents Sea after Nordic Seas warming could explain this relationship as decreasing sea ice concentration at the Barents Sea increases the volume transport through the Barents Sea Opening and the Iceland-Norway strait.

On decadal time scale, the subpolar ocean receives more downward surface flux when there are frequent blocking events in winter. Regions that are most sensitive to

the surface flux changes move northeastward when the mean blocking frequency decreases. Winter-time blocking days are negatively correlated with volume fluxes into and out of the Nordic Seas, and therefore, when there are few blocking events, more heat is advected into the Arctic Basin through the Nordic Seas.

Some studies have pointed out that under the global warming background, there is a northeastward movement of the NAO low-pressure center and Atlantic storm tracks [*Ulbrich and Christoph*, 1999; *Jung et al.*, 2003]. With the displaced Atlantic storm tracks, we could expect that impacts of heat advection on the decadal variability of Atlantic water in the Nordic Seas become weaker. Meanwhile, it's possible that the heat of the Nordic Seas will be brought into the interior of Europe.

Chapter 5: Conclusions

5.1 Summary of results

My thesis focuses on the climate variability of the atmosphere, ocean and sea ice of the high latitude oceans from seasonal to centennial time scale in fourteen CMIP5 coupled climate models. Climate responses of high latitudes to volcanic forcing, green house gas forcing, and the internal variability are examined in this dissertation study. The historical simulations from CMIP5 coupled climate models are selected because the observational data are limited especially at the high latitude oceans. The coupled climate models provide a comprehensive data set of the entire climate system, which allows us to evaluate the interactions among atmosphere, ocean and sea ice on different time scales.

All the fourteen CMIP5 models capture the basic pattern of the atmosphere, ocean and sea ice mean state at high latitude oceans, although the magnitudes vary among models. The winter-time Arctic is characterized by a Polar high-pressure center over the Beaufort Sea and two low-pressure centers on the North Atlantic and Pacific Oceans. The surface radiative and turbulent fluxes resemble the ERA-40 reanalysis data. In addition, the NAO pattern in the sea level pressure field is found in all models; however, the location of the NAO low-pressure center shows large variations among models. The frequency of winter-time blocking events over the North Atlantic sector also exhibits large biases. One possible reason for the different blockings among these models is the different spatial resolutions [*Anstey et al.* 2013]. In general, models with frequent blocking events over the North Atlantic shows a northeastward movement of the NAO low-pressure center.

The upper layer ocean temperature at the Nordic Seas and the northern Barents Sea presents large biases compared to observations. Meanwhile, the salinity profile in these two regions is similar to observations. The strength of the Beaufort Gyre is positively correlated with the strength of the Polar high, which in turn affects the salinity distribution in the Arctic Basin. In models with a strong Polar high, the fresh water is concentrated in the Beaufort Gyre, while in models with a weak Polar high, more fresh water is found at the marginal seas. Volume transports through the Bering Strait, the Davis Strait, the Fram Strait and the Barents Sea Opening vary from model to model. One big difference in the AMOC in these models is the magnitude of its variability. In models like GFDL-CM3, the natural variability of AMOC reaches several Sv. In models like CCSM4, the AMOC variability is much smaller. The sea ice extent also shows large differences especially to the south 65°N. The summer-time sea ice extent shrinks into the Arctic Basin in some models while in other models, the sea ice melting in summer mainly happens at the Pacific and Atlantic Oceans.

The fist part of this dissertation study examines the response of global and high latitude oceans to the stratospheric volcanic aerosols. All models show an annual average global reduction in net surface solar radiation of 1-5 W m^{-2}, a drop in net surface heat flux of 1-3 W m^{-2}, and a resulting decline in SST of 0.1-0.3 K. Sea ice extent and mass in the North Hemisphere also increase by about 5%. The increase of surface salinity at North Atlantic is more significant than that of global scale. Surface flux and SST recovers in a few years, a little bit longer than lifetime of stratospheric aerosols. The increase in sea ice area and mass persists even longer (~7 to 8 years)

due to the reinforcing impact of solar albedo feedback and reductions in thermodynamic surface heat loss. The cool SST signal also penetrates into the subsurface ocean, lowering 0-1000m temperature by an average of roughly 0.03 K, and persisting for many decades, masking some of the anthropogenic warming signal. Indeed, comparisons of simulations with and without volcanic aerosols show that the concentration of eruptions in the early years of the 20th century and again in the near the end of the century may mask some of the acceleration of ocean heating that might otherwise have been observed.

Results show that there is no compelling evidence of a link between the timing of an eruption and a shift in phase of ENSO. A similar effort has been made to examine the relationship between the volcanic eruptions and the phase of NAO in boreal winter sea level pressure and found similarly tenuous connections. Volcanic eruptions may enhance the overturning circulation (and consequently increase northward heat transport) due to increases in ocean surface density in the northern Atlantic sector. The composite study indicates that AMOC is enhanced after volcanic eruptions in all models. A comparison shows that the models vary by at least a factor of four in their sensitivity, the most sensitive models being those which have the most Atlantic meridional overturning variability in general.

The second part of study focus on the climate variability from seasonal and centennial time scale. The warming of the Arctic Ocean is found in all models with enhanced downward surface heat flux, retreat of sea ice, increased temperature of mix-layer sea water, enhanced heat convergence into the Arctic, and changes of

upper-layer salinity in the Arctic Basin. However, the amplitude of Arctic warming as well as the seasonal difference is different among models.

The heat content of sea water in the mix-layer increases with a clear seasonal cycle. In contrast, the amount of melting sea ice presents very few seasonal variations. The seasonal variability in the mix-layer heat content is largely determined by the surface heat flux with a correlation coefficient of 96%. In models with strong seasonal cycle of surface net flux, the centennial decreasing trend of sea ice cover is comparable in all seasons. The retreat of sea ice extent in winter allows more evaporation at the ocean surface, which increases the upward latent heat flux and decreases oceanic heat gain.

The increasing trend of heat transport into the Arctic Basin exhibits very limited seasonal difference in most models. Both the surface net flux and heat convergence are important to the warming of sea water in recent decades.

The spatial pattern of salinity changes in the Arctic Ocean varies among models. Models with similar Polar high strength to observations present similar salinity changes to observations, which is more saltier sea water in the Laptev Sea and more fresher water in the Beaufort Gyre. Other models in which the strength of Polar high is either weaker or stronger than the observations fail to capture this spatial pattern. This indicates that the atmospheric circulation has a significant impact on the regulating the salinity distribution in recent decades.

In the third part of my dissertation study, the atmospheric blocking events over the North Atlantic and their potential impacts on the decadal variability in the Nordic Seas are studied. Models with few Greenland blocking events in general are

characterized by a northeastward shift of the NAO low-pressure center, which makes the surface wind more horizontal and the northward ocean velocity much weaker at the Iceland-Norway strait. Thus, in those models the heat advection into the Nordic Seas shows weaker decadal variability, and the surface heating plays a more important dominant role in the decadal variability of Atlantic water in the Nordic Seas. In CCSM4 and MRI-CGCM3, both of which show vary rare winter-time Greenland blocking events, the surface net flux could explain ~70% of the heat storage anomalies ($\partial HC/\partial t$).

In winters with more frequent Greenland blocking events or the negative phase of NAO, the subpolar ocean becomes warmer due to the increasing downward surface heat flux. With the northeastward movement of the low-pressure center, the region where the surface heat flux is closely correlated with the NAO index also moves northeastward. The winter-time Greenland blocking events are negatively correlated with volume fluxes at the Iceland-Norway Strait and the Barents Sea Opening, although the significance is limited. This indicates that more heat is advected into the Arctic Basin through the Nordic Seas in winters with infrequent Greenland blocking events.

When the Atlantic water in the Nordic Seas region warms, more sea ice at the Barents Sea melts and more Atlantic water enters the Arctic through the Barents Seas Opening. This might explain why the changing rate of heat storage anomaly leads the heat transport into the Nordic Seas by about 1 year.

Some studies have pointed out that under the global warming background, there is a northeastward movement of the NAO low-pressure center and Atlantic storm tracks

[*Ulbrich and Christoph*, 1999; *Jung et al.*, 2003]. With the displaced Atlantic storm tracks, we could expect that impacts of heat advection on the decadal variability of the Nordic Seas become weaker. Meanwhile, the local surface heat flux might become the dominant contributor.

5.2 Implications and future plans

In this dissertation I try to examine climate variability of high latitude ocean on different time scales by analyzing the historical simulations from the archive of CMIP5 coupled climate models. The results reported in this thesis have important and interesting implications for future work in the following fields:

(1) *The prediction of the Arctic sea ice extent trend in winter*. Results show that the winter-time Arctic sea ice extent change is crucial to the seasonal cycle of surface net flux trend in recent decades. In some models like GFDL-ESM2G, the sea ice extent even slightly increases in winter despite of the decreasing sea ice volume. One possible explanation is that the ocean currents spread the broken sea ice to a larger area. Whether this explanation is sufficient or there is any other explanations for this phenomenon requires more efforts.

(2) *The origin of AMOC variability and relationship between NAO and AMOC*. I conclude that AMOC is enhanced after volcanic eruptions and that the magnitude of enhanced AMOC depends on its natural variability. What has not been resolved in this study is that why the AMOC variability presents large differences among the coupled climate models? In addition, previous studies pointed out that volcanic eruptions shift the NAO into positive phase, which intrigues the enhanced AMOC. However, in this study, very limited

NAO responses to volcanic eruptions are found. Why the stratospheric aerosol heating does not lead to positive NAO and why the relationship between the NAO and AMOC is weak in CMIP5 models need further study.

(3) *What controls the surface heat flux over the Nordic Seas?* In models with infrequent winter-time Greenland blocking events, the local surface heating plays a dominant role in the decadal variability of the Nordic Seas. However, both the frequency of Greenland blocking and the NAO show weak influences on the surface net fluxes in this region. Its correlation with the AMOC is also not significant. Which climate variability is more important to the decadal variability of surface heat fluxes in the Nordic Seas is an interesting topic to study with later on.

In summary, research in this dissertation constitutes a step towards better understanding the climate variability at the high latitude oceans. Future efforts on the interaction of different climate phenomena, like the NAO and AMOC, will be crucial to understand the high latitude climate system.

Bibliography

Adams, J. B., M.E. Mann and C. M. Caspar (2003), Proxy evidence for an El Niño response to volcanic forcing, *Nature, 426,* 274–278.

Ammann, C. M., G. A Meehl and W. M. Washington (2003), A monthly and latitudinally varying volcanic forcing dataset in simulations of 20th century climate. *Geophys. Res. Letts.*, *30*, 1657, doi:10.1029/2003GL016875.

Andrews T., J. M. Gregory , M. J. Webb, K. E. Taylor (2012), Forcing, feedbacks and climate sensitivity in CMIP5 coupled atmosphere-ocean climate models. *Geophys. Res. Letts., 39*, L09712, doi:10.1029/2012GL051607.

Angell, J. K. (1988), Impact of E1 Nino on the delineation of tropospheric cooling due to volcanic eruptions. *J. Geophys. Res.*, *93,* 3697–3704.

Angell, J. K. and J. Korshover (1985), Surface temperature changes following the six major volcanic episodes between 1780 and 1980. *J. Clim. Appl. Meteorol., 24,* 937–951.

Anstey, J. A., P. Davini, L. J. Gray, T. J. Woollings, N. Butchart et al. (2013), Multi-model analysis of Northern Hemisphere winter blocking: Model biases and the role of resolution. *J. Geophys. Res.- Atmos.*, **118**, 3956–3971. doi:10.1002/jgrd.50231

Barriopedro, D., R. García-Herrera, A. R. Lupo and E. Hernán- dez (2006), A climatology of Northern Hemisphere blocking. *J. Climate*, **19**, 1042–1063.

Berrisford, P., B. J. Hoskins and E. Tyrlis (2007), Blocking and Rossby wave breaking on the dynamical tropopause in the Southern Hemisphere. *J. Atmos. Sci*., **64**, 2881–2898.

Blindheim, J., V. Borovkov, B. Hansen, S. A. Malmberg, W. R. Turrell and S. Østerhus (2000), Upper layer cooling and freshening in the Norwegian Sea in relation to atmospheric forcing. *Deep Sea Research Part I: Oceanographic Research Papers*, **47**, 655-680.

Boé, J., A. Hall and X. Qu (2009). Current GCMs' Unrealistic Negative Feedback in the Arctic. *J. Climate*, **22**, 4682–4695. doi:10.1175/2009JCLI2885.1

Booth, B.B., N. J. Dunstone, P. R. Halloran, T. Andrews and N. Bellouin (2012), Aerosols implicated as a prime driver of twentieth-century North Atlantic climate variability. *Nature*, *484*, 228–232.

Canty, T., Mascioli, N. R., Smarte, M. D., and Salawitch, R. J., 2013: An empirical model of global climate–Part 1: A critical evaluation of volcanic cooling. *Atmos.Chem. and Phys.*, **13**, 3997-4031.

Carmack, E. C., R. W. Macdonald, R. G. Perkin, F. A. Mclaughlin and R. J. Pearson (1995). Evidence for warming of Atlantic water in the Southern Canadian Basin of the Arctic Ocean: Results from the Larsen-93 expedition. *Geophys. Res. Lett.*, **22**, 1061–1064.

Carton, J. A., G. Chepurin, J. Reagan and S. Häkkinen (2011), Interannual to decadal variability of Atlantic Water in the Nordic and adjacent seas. *J. Geophys. Res.*, **116**, C11035. doi:10.1029/2011JC007102

Carton, J.A. and B. S. Giese (2008), A reanalysis of ocean climate using Simple Ocean Data Assimilation (SODA), *Mon. Wea. Rev.*, *136,* 2999-3017.

Cavalieri, D. J., C. L. Parkinson and K. Y. Vinnikov (2003). 30-Year satellite record reveals contrasting Arctic and Antarctic decadal sea ice variability. *Geophys. Res. Lett.*, **30**, doi:10.1029/2003GL018031

Christiansen, B. (2008), Volcanic Eruptions, Large-Scale Modes in the Northern Hemisphere and the El Niño–Southern Oscillation. *J. Clim.*, *21,* 910–922.

Cobb, K. M., C. D. Charles, H. Cheng and R. L. Edwards (2003), El Niño/Southern Oscillation and tropical Pacific climate during the last millennium. *Nature*, *424*, 271-276.

Collins, W. J., N. Bellouin, M. Moutriaux-Boucher *et al.* (2011), Development and evaluation of an Earth-System model - HadGEM2, *Geosci. Model Dev. Discuss*, *4,* 997-1062.

Croci-Maspoli, M., C. Schwierz and H. Davies (2007), Atmospheric blocking: Space-time links to the NAO and PNA. *Climate Dyn.*, **29**, 713-725.

Crowley, T. J. and M. B. Unterman (2012), Technical details concerning development of a 1200-yr proxy index for global volcanism. *Earth Syst. Sci. Data Discuss.*, *5,* 1–28.

Curry, J. A. and J. L. Schramm (1995). Sea Ice-Albedo Climate Feedback Mechanism. *J. Climate*, **8**, 240–247.

Curry, J. A., J. L. Schramm and E. E. Ebert (1993). Impact of Clouds on the Surface Radiation Balance of the Arctic Ocean. *Meteorol. Atmos. Phys*, **51**, 197–217.

Curry, J., W. Rossow, D. Randall and J. Schramm (1996). overview of arctic cloud and radiation characteristics. *J. Climate*, **9**, 1731–1764.

Davini, P., C. Cagnazzo, R. Neale and J. Tribbia (2012). Coupling between Greenland blocking and the North Atlantic Oscillation pattern. *Geophys. Res. Letts*., doi:10.1029/2012GL052315

Delworth, T. L., V. Ramaswamy and G. L. Stenchikov (2005), The impact of aerosols on simulated ocean temperature and heat content in the 20th century. *Geophys. Res. Letts.*, *32,* L24709, doi:10.1029/2005GL024457.

Dickson, B., S. Dye, S. Jónsson, A. Köhl, A. Macrander, M. Marnela et al. (2008), The overflow flux west of Iceland: variability, origins and forcing. In *Arctic–Subarctic Ocean Fluxes* (pp. 443-474). Springer Netherlands.

Dickson, R. R., T. J. Osborn, J. W. Hrrrell, J. Meincke et al. (2000). The Arctic Ocean Response to the North Atlantic Oscillation. *J. Climate*, **95**, 2671–2696.

Dickson, R.R., J. Lazier, J. Meincke, P. Rhines, J. Swift (1996), Long-term coordinated changes in the convective activity of the North Atlantic. *Prog. Oceanogr.,* **38**, 241-295.

Drange, H., T. Dokken, T. Furevik, R. Gerdes and W. Berger (2005), The Nordic Seas: An Integrated Perspective oceanography, climatology, biogeochemistry and modeling, *American Geophysical Union, Washington DC*

Drijfhout, S., G. Oldenborgh, and A. Cimatoribus, 2012: Is a Decline of AMOC Causing the Warming Hole above the North Atlantic in Observed and Modeled Warming Patterns?. *J. Climate*, 25, 8373–8379.

Driscoll, S., A. Bozzo, L. J. Gray, A. Robock and G. Stenchikov (2012), Coupled Model Intercomparison Project 5 (CMIP5) simulations of climate following volcanic eruptions. *J. Geophys. Res.*, *117,* D17105. doi:10.1029/2012JD017607

Dunne, J. P., J. G. John, A. J. Adcroft *et al.* (2012), GFDL's ESM2 Global Coupled Climate–Carbon Earth System Models. Part I: Physical Formulation and Baseline Simulation Characteristics. *J. Clim., 25*, 6646–6665.

Dunn-Sigouin, E. and S.W. Son (2013). Northern Hemisphere blocking frequency and duration in the CMIP5 models. *J. Geophys. Res.- Atmos.*, **118**, 1179–1188. doi:10.1002/jgrd.50143

Eden, C. and T. Jung (2001). North Atlantic Interdecadal Variability : Oceanic Response to the North Atlantic Oscillation (1865 – 1997). *J. Climate*, **14**, 676–691.

Emile-Geay, J., R. Seager, M. A. Cane, E. R. Cook and G. H. Haug (2008), Volcanoes and ENSO over the Past Millennium. *J. Clim.*, *21*, 3134–3148.

Evan, A. T., D. J. Vimont, A. K. Heidinger, J. P. Kossin and R. Bennartz (2009), The role of aerosols in the evolution of tropical North Atlantic Ocean temperature anomalies. *Science*, *324,* 778-781.

Franzke, C., S. Lee and S. B. Feldstein (2004), Is the North At- lantic Oscillation a breaking wave? *J. Atmos. Sci*., **61**, 145– 160.

Furevik, T. (2001). Annual and interannual variability of Atlantic Water temperatures in the Norwegian and Barents Seas: 1980–1996. *Deep Sea Research Part I: Oceanographic Research Papers,* **48**, 383–404

Gao, C., A. Robock and C. Ammann (2008), Volcanic forcing of climate over the past 1500 years: An improved ice core-based index for climate models. *J. Geophys. Res.*, *113,* D23111. doi:10.1029/2008JD010239

Gent, P. R., G. Danabasoglu, L.J. Donner, *et al.* (2011), The community climate system model version 4. *J. Clim.*, *24,* 4973-4991.

Gleckler, P. J., T. M. L. Wigley, B. D. Santer, J. M. Gregory, K. Achutarao and K. E. Taylor (2006), Volcanoes and climate: Krakatoa's signature persists in the ocean. *Nature, 439,* 675.

Graversen, R. G. and M. Wang (2009). Polar amplification in a coupled climate model with locked albedo. *Clim. Dynam.*, **33**, 629–643

Gregory, J. M. (2010). Long-term effect of volcanic forcing on ocean heat content. *Geophys. Res. Letts.*, *37,* L22701, doi:10.1029/2010GL045507

Griffies, S. M., W. Winton, L. J. Donner, *et al.* (2011), GFDL-CM3 coupled climate model: characteristics of the ocean and sea ice simulations. *J. Clim., 24*, 3520-3544.

Grotefendt, K., K. Logemann, D. Quadfasel and S. Ronski (1998). Is the Arctic Ocean warming? *J. Geophys. Res.*, **103**, doi:10.1029/98JC02097

Guan, B. and S. Nigam (2008). Pacific sea surface temperatures in the twentieth century: An evolution-centric analysis of variability and trend. *J. Clim.*, *21,* 2790-2809.

Häkkinen, S., P. B. Rhines and D. L. Worthen (2011). Atmospheric blocking and Atlantic multidecadal ocean variability. *Science,* **334**, 655–659

Hann, J. (1890), Zur Witterungsgeschichte von Nord-Gronland,West- kuste. *Meteor. Z.*, **7**, 109–115.

Haywood, J. M., A. Jones, N. Bellouin and D. Stephenson (2013), Asymmetric forcing from stratospheric aerosols impacts Sahelian rainfall. *Nature Climate Change*, *3,* 660–665.

Hilmer, M. and T. Jung, (2000). Evidence for a recent change in the link between the North Atlantic Oscillation and Arctic sea ice export, *Geophys. Res. Letts*., **27**, 989–992.

Holloway, G. and T. Sou (2002). Has Arctic Sea Ice Rapidly Thinned ? *J. Climate*, **15**, 1691–1701.

Huang, J., M. Ji, K. Higuchi and A. Shabbar (2006), Temporal structures of the North Atlantic Oscillation and its impact on the regional climate variability. *Adv. Atmos. Sci*., **23**, 23–32.

Hurrell, J. (1996), Influence of variations in extratropical wintertime teleconnections on northern hemisphere temperatures. *Geophys. Res. Letts.*, **23**, 665-668.

Iwi, A. M., L. Hermanson, K. Haines and R. T. Sutton (2012), Mechanisms linking volcanic aerosols to the Atlantic meridional overturning circulation. *J. Clim.*, *25,* 3039–3051.

Jiang, J. H., H. Su, C. Zhai, et al. (2012). Evaluation of cloud and water vapor simulations in CMIP5 climate models using NASA “A-Train” satellite observations. *J. Geophys. Res.*, **117**, D14105. doi:10.1029/2011JD017237

Johnson, M. A. and I. V. Polyakov (2001). The Laptev Sea as a source for recent Arctic Ocean salinity changes. *Geophys. Res. Lett.,* **28**, 2017–2020.

Jones, T. C., *et al.* (2003), Anthropogenic climate change for 1860 to 2100 simulated with the HadCM3 model under updated emissions scenarios. *Clim. Dynam.*, *20,* 583–612.

Jung, T., M. Hilmer, E. Ruprecht, S. Kleppek, S. K. Gulev and O. Zolina (2003), Characteristics of the Recent Eastward Shift of Interannual NAO Variability. *J. Climate*, **16**, 3371–3382.

Knight, J. R., R. J. Allen, C. K. Folland, M. Vellinga, and M. E. Mann, 2005: A signature of persistent natural thermohaline circulation cycles in observed climate. *Geophys. Res. Lett.*, **32**, L20708, doi:10.1029/2005GL024233.

Levitus, S., J. I. Antonov, T. P. Boyer, R. A. Locarnini, H. E. Garcia and A. V. Mishonov (2009), Global ocean heat content 1955–2008 in light of recently revealed instrumentation problems, *Geophys. Res. Letts.*, **36**, L07608, doi:10.1029/2008GL037155

Lique, C. and M. Steele (2013). Seasonal to decadal variability of Arctic Ocean heat content: A model-based analysis and implications for autonomous observing systems. *J. Geophys. Res.-Oceans*, **118**, 1673–1695.

Luo, D. (2005), Why is the North Atlantic block more frequent and long-lived during the negative NAO phase? *Geophys. Res. Lett*., **32**, L20804, doi:10.1029/2005GL022927.

Luo, D., A. R. Lupo and H. Wan (2007), Dynamics of eddy-driven low-frequency dipole modes. Part I:Asimple model of North Atlantic Oscillations. *J. Atmos. Sci*., **64**, 3–28.

Mann, M. E., M. A. Cane, S. E. Zebiak and A. Clement (2005), Volcanic and solar forcing of the Tropical Pacific over the past 1000 years, *J. Clim.*, *18,* 447–456.

Masato, G., B. J. Hoskins and T. Woollings (2013). Winter and Summer Northern Hemisphere Blocking in CMIP5 Models. *J. Climate*, **26**, 7044–7059. doi:10.1175/JCLI-D-12-00466.1

Masato, G., T. Woollings and B. J. Hoskins, (2014). Structure and impact of atmospheric blocking over the Euro-Atlantic region in present-day, *Geophys. Res. Letts*., **41**, 1051–1058, doi:10.1002/2013GL058570.The

Mass, C. F. and D. A. Portman (1989), Major volcanic eruptions and climate: a critical evaluation. *J. Clim.*, *2,* 566–593.

Matishov, G. G., D. G. Matishov and D. V. Moiseev (2009), Inflow of Atlantic-origin waters to the Barents Sea along glacial troughs, *Oceanologia*, **51**, 321-340

Mauritsen, T., B. Stevens, E. Roeckner, *et al.* (2012), Tuning the climate of a global model. *Journal of Advances in Modeling Earth Systems***,** *4,* M00A01. doi:10.1029/2012MS000154

McGregor, S. and A. Timmermann (2011), The effect of explosive tropical volcanism on ENSO. *J. Clim.*, *24,* 2178–2191.

McGregor, S., A. Timmermann and O. Timm, (2010), A unified proxy for ENSO and PDO variability since 1650. *Clim. of the Past*, *6,* 1–17.

Mcphee, G., P. Stanton, H. Morison and G. Martinson (1998). Freshening of the upper ocean in the Arctic: Is perennial sea ice disappearing? *Geophys. Res. Lett.*, **25**, 1729–1732.

Mignot, J., M. Khodri, C. Frankignoul and J. Servonnat (2011), Volcanic impact on the Atlantic Ocean over the last millennium, *Clim. Past*, *7,* 1439–1455, doi:10.5194/cp-7-1439-2011.

Minnis, P., E. F. Harrison, L. L. Stowe, G. G. Gilbson, F. M. Denn, D. R. Doelling and W. L. Smith Jr. (1993), Radiative climate forcing by Mount Pinatubo eruption. *Science*, *259,* 1369–1508.

Moritz, R. E., C. M. Bitz and E. J. Steig (2002). Dynamics of recent climate change in the Arctic. *Science,* **297**, 1497–502.

Mork, K. A. and J. Blindheim (2000), Variations in the Atlantic inflow to the Nordic Seas, 1955-1996, *Deep Sea Research Part I: Oceanographic Research Papers*, **47**, 1035-1057.

Msadek, R., and C. Frankignoul, 2009: Atlantic multidecadal oceanic variability and its influence on the atmosphere in a climate model. *Climate Dyn*., **33**, 45–62.

Otterå, O. H., M. Bentsen, H.Drange and L. Suo (2010), External forcing as a metronome for Atlantic multidecadal variability. *Nature Geosci.*, *3,* 688-694.

Overland, J. E., M. C. Spillane and N. N. Soreide (2004). Integrated Analysis of Physical and Biological Pan-Arctic Change. *Climatic Change*, **63**, 291–322.

Proshutinsky, A. and M. A. Johnson (1997). Two circulation regimes of the wind-driven Arctic Ocean. *J. Geophys. Res.*, **102**, 493–514.

Proshutinsky, A., R. H. Bourke and F. A. McLaughlin (2002). The role of the Beaufort Gyre in Arctic climate variability: Seasonal to decadal climate scales. *Geophys. Res. Lett.*, **29**, doi:10.1029/2002GL015847

Rampino, M. R. and S. Self (1982), Historic eruptions of Tambora (1815), Krakatau (1883) and Agung (1963), their stratospheric aerosols and climatic impact. *Quatern. Res.*, *18,* 127–143.

Rayner, N.A., D.E. Parker, E.B. Horton, C.K. Folland, L.V. Alexander, D.P. Rowell, E.C. Kent and A. Kaplan (2003), Global analyses of sea surface temperature, sea ice and night marine air temperature since the late nineteenth century. *J. Geophys. Res.*, *108,* D14, 4407 10.1029/2002JD002670.

Rex, D., (1950a): Blocking action in the middle troposphere and its effect upon regional climate: I. An aerological study of blocking action. *Tellus*, **2**, 196–211.

Rex, D., (1950b): Blocking action in the middle troposphere and its effect upon regional climate: II. The climatology of blocking action. *Tellus*, **2**, 275–301.

Rigor, I. G., R. L. Colony and S. Martin (2000). Variations in Surface Air Temperature Observations in the Arctic, 1979–97. *J. Climate*, **13**, 896–914.

Robock, A. (2000), Volcanic eruptions and climate. *Rev. Geophys.*, *38*, 191–219.

Robock, A. and J. Mao (1992), Winter warming from large volcanic eruptions. *Geophys. Res. Letts., 19,* 2405-2408.

Robock, A. and J. Mao (1995), The volcanic signal in surface temperature observations. *J. Clim*., *8*, 1086-1103.

Robock, A., K. E. Taylor, G. L. Stenchikov and Y. Liu (1995), GCM evaluation of a mechanism for El Niño triggering by the El Chichón ash cloud, *Geophys. Res. Letts., 22*, 2369–2372.

Rogers, J. C., (1997), North Atlantic Storm Track Variability and Its Association to the North Atlantic Oscillation and Climate Variability of Northern Europe. *J. Climate*, **10**, 1635–1647.

Sato, M., J. E. Hansen, M. P. McCormick and J. B. Pollack (1993), Stratospheric Aerosol Optical Depths, 1850-1990. *J. Geophys. Res.*, *98*, 987–994.

Schmidt, G. A., J. H. Jungclaus, C. M. Ammann *et al.* (2011), Climate forcing reconstructions for use in PMIP simulations of the last millennium (v1.0). *Geosci. Model Dev.*, *4*, 33–45.

Schmitz, W. J. (1995), On the interbasin scale thermohaline circulation. *Rev. Geophys.*, *33*, 151-173.

Self, S., M. R. Rampinoz, J. Zhao and M. G. Katz (1997), Volcanic aerosol perturbations and strong El Niño events: *Geophys. Res. Letts.*, *24*, 1247–1250.

Serreze, M. C., A. P. Barrett, A. G. Slater, et al. (2006). The large-scale freshwater cycle of the Arctic. *J. Geophys. Res.-Oceans*, **111**, C11010. doi:10.1029/2005JC003424

Serreze, M. C., M. M. Holland and J. Stroeve (2007). Perspectives on the Arctic's shrinking sea-ice cover. *Science*, **315**, 1533–1536.

Serreze, M. C., M. M. Holland and J. Stroeve, (2007), Perspectives on the Arctic's shrinking sea-ice cover. *Science*, **315**, 1533–1536.

Shabbar, A., J. Huang and K. Higuchi (2001), The relationship between the wintertime North Atlantic Oscillation and blocking episodes in the North Atlantic. *J. Climate*., **21**, 355–369.

Shimada, K., T. Kamoshida, M. Itoh, et al. (2006). Pacific Ocean inflow: Influence on catastrophic reduction of sea ice cover in the Arctic Ocean. *Geophys. Res. Lett.*, **33**, L08605. doi:10.1029/2005GL025624

Slonosky, V. C., L. A. Mysak and J. Derome (1997). Linking Arctic sea-ice and atmospheric circulation anomalies on interannual and decadal timescales. *Atmosphere-Ocean*, **35**, 333–366.

Solomon, S., D. Qin, M. Manning, Z. Chen, M. Marquis, K.B. Averyt, M. Tignor and H.L. Miller (eds.) (2007), Contribution of working group I to the fourth assessment report of the Intergovernmental Panel on Climate Change, 2.7.2.1 Radiative Effects of Volcanic Aerosols, *Cambridge University Press*, Cambridge, United Kingdom and New York, NY, USA.

Sorterberg, A. and B. Kvinggedal, (2006), Atmospheric Forcing on the Barents Sea Winter Ice Extent. *J. Climate*, **19**, 4772–4784.

Steele, M., J. Zhang *and* W. Ermold (2010*).* Mechanisms of summertime upper Arctic Ocean warming and the effect on sea ice melt*, J. Geophys. Res.,* **115***, C11004, doi:10.1029/2009JC005849.*

Steele, M., R. Morleyand W. Ermold (2001). PHC: A global ocean hydrography with a high-quality Arctic Ocean. *J. Climate*, **14**, 2079-2087.

Stenchikov, G., A. Robock, V. Ramaswamy, M. D. Schwarzkopf, K. Hamilton and S. Ramachandran (2002), Arctic Oscillation response to the 1991 Mount Pinatubo eruption: Effects of volcanic aerosols and ozone depletion. *J. Geophys. Res.*, *107*, NO. D24, 4803, doi:10.1029/2002JD002090.

Stenchikov, G., I. Kirchner, A. Robock, H.-F. Graf, J.C. Antuña, R.G. Grainger, A. Lambert and L. Thomason (1998). Radiative forcing from the 1991 Mount Pinatubo volcanic eruption. *J. Geophys. Res, 103*, 13837-13857.

Stenchikov, G., K. Hamilton, R. J. Stouffer, A. Robock, V. Ramaswamy, B. Santer and H.-F. Graf (2006), Arctic Oscillation response to volcanic eruptions in the IPCC AR4 climate models. *J. Geophys. Res*, *111*, D07107, doi:10.1029/2005JD006286.

Stenchikov, G., T. L. Delworth, V. Ramaswamy, R. J. Stouffer, A. Wittenberg and F. Zeng (2009), Volcanic signals in oceans. *J. Geophys. Res.*, *114***,** D16104, doi:10.1029/2008JD011673.

Stothers, R. B. (1996), Major optical depth perturbations to the stratosphere from volcanic eruptions: Pyrheliometric period, 1881–1960, *J. Geophys. Res., 101*, 3901–3920.

Stroeve, J. C., V. Kattsov, A. Barrett, M. Serreze, T. Pavlova, M. Holland and W. N. Meier (2012). Trends in Arctic sea ice extent from CMIP5, CMIP3 and observations. *Geophys. Res. Lett.*, **39**, doi:10.1029/2012GL052676

Swift, J. H., K. Aagaard, L. Timokhov and E. G. Nikiforov (2005), Long-term variability of Arctic Ocean waters: Evidence from a reanalysis of the EWG data set, *J. Geophys. Res.,* **110**, C03012, doi:10.1029/ 2004JC002312.

Talley, L. D., G. L. Pickard, W. J. Emery and J. H. Swift (2011). Descriptive Physical Oceanography: An Introduction (Sixth Edition), *Elsevier*, Boston, 560 pp.

Tom Markvart, Luis CastaŁżer (2003). Practical Handbook of Photovoltaics: Fundamentals and Applications. *Elsevier*. ISBN 1-85617-390-9.

Ulbrich, U. and M. Christoph (1999), A shift of the NAO and increasing storm track activity over Europe due to anthropogenic greenhouse gas forcing. *Climate Dynamics*, **15**, 551–559.

Uppala, S. M., et al. (2005), The ERA-40 re-analysis, *Quart. J. Roy. Meteor. Soc*., **131**, 2961–3012

Venegas, S. A. and L. A. Mysak (2000), Is There a Dominant Timescale of Natural Climate Variability in the Arctic ? . *J. Climate,* **13**, 3412–3434.

Wallace, J. and D. Gutzler (1981), Teleconnections in the geopotential height field during the Northern Hemisphere winter, *Mon. Weather Rev*., **109**, 784–812

Walsh, J. E., W. L. Chapman and T. Shy (1996). Recent decrease of sea level pressure in the central Arctic. *J. Climate*, **9**, 480–486.

Wang, M. and J. E. Overland (2012). A sea ice free summer Arctic within 30 years: An update from CMIP5 models. *Geophys. Res. Lett.*, **39**, doi:10.1029/2012GL052868

Woollings, T., A. Hannachi, B. Hoskins and A. Turner (2010), A regime view of the North Atlantic Oscillation and its response to anthropogenic forcing. *J. Climate*, **23**, 1291-1307.

Woollings, T., B. Harvey and G. Masato (2014). Arctic warming, atmospheric blocking and cold European winters in CMIP5 models. *Environmental Research Letters*, ***9***, 014002. doi:10.1088/1748-9326/9/1/014002

Woollings, T., B. Hoskins, M. Blackburn and P. Berrisford (2008), A New Rossby Wave–Breaking Interpretation of the North Atlantic Oscillation. *J. Atmos. Sci.*, **65**, 609–626. doi:10.1175/2007JAS2347.1

Wouters, B., S. S. Drijfhout, and W. Hazeleger, 2012: Interdecadal North Atlantic meridional overturning circulation variability in EC-EARTH. *Climate Dyn*., **39**, 2695–2712, doi:10.1007/s00382-012-1366-4.

Yukimoto, S., *et al.* (2012), A new global climate model of the Meteorological Research Institute: MRI-CGCM3 -- model description and basic performance; *J. Meteorol. Soc. Japan*, *90*, 23–64.

Zanchettin, D., C. Timmreck, O. Bothe, S. J. Lorenz, G. Hegerl, H.-F. Graf, J. Luterbacher and J. H. Jungclaus (2012), Delayed winter warming: A robust decadal response to strong tropical volcanic eruptions? *Geophys. Res. Lett.*, *40*, 204–209.

Zanchettin, D., O. Bothe, H.-F. Graf, S. J. Lorenz, J. Luterbacher, C. Timmreck and J. H. Jungclaus (2013), Background conditions influence the decadal climate response to strong volcanic eruptions. *J. Geophys. Res.*, *118*, 4090-4106.

Zappa, G., G. Masato, L. Shaffrey, T. Woollings and K. Hodges (2014). Linking Northern Hemisphere blocking and storm track biases in the CMIP5 climate models. *Geophys. Res. Letts*, **41**, 135–139. doi:10.1002/2013GL058480

Zhang, H. M., R. W. Reynolds and T. M. Smith (2004), Bias characteristics in the AVHRR sea surface temperature. *Geophys. Res. Lett.*, *31*, L01307, doi:10.1029/2003GL018804.

Zhang, R., T. L. Delworth, R. Sutton *et al.* (2013), Have Aerosols Caused the Observed Atlantic Multidecadal Variability? *J. Atmos. Sci*., *70*, 1135–1144.

Zhong, Y., G. H. Miller, B.L. Otto-Bliesner, M.M. Holland, D.A. Bailey, D.P. Schneider and A. Geirsdottir (2011), Centennial-scale climate change from

decadally-paced explosive volcanism: a coupled sea ice-ocean mechanism, *Clim. Dynam*., *37*, 2373-2387, DOI 10.1007/s00382-010-0967-z.